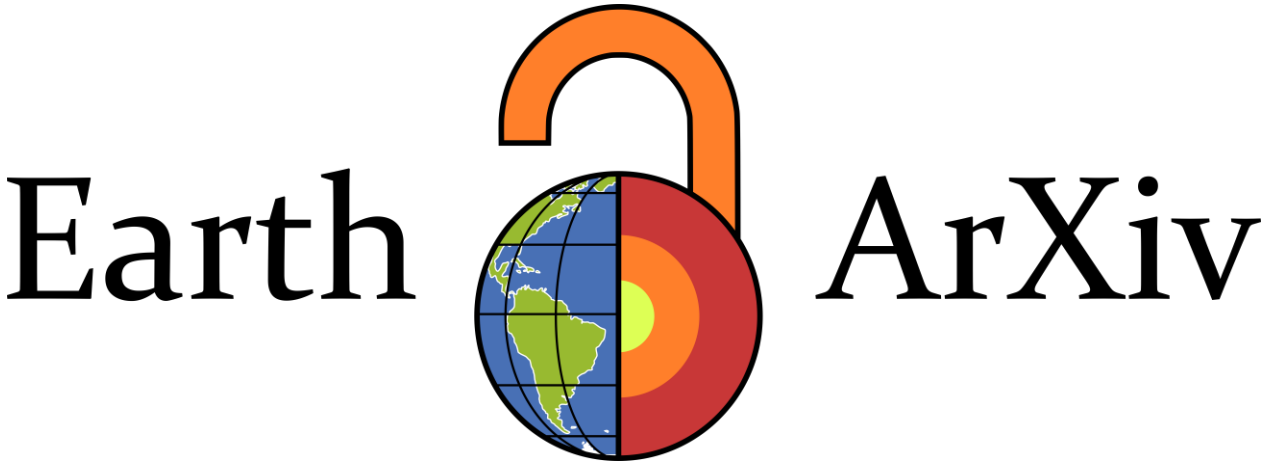

Paleoarchean seawater and seafloor hydrothermal processes: insights from 3.5 to 3.3 Ga carbonate geochemistry

Xiang, Wanli[a, b], Duda, Jan-Peter[b], Pack, Andreas[c], Willbold, Matthias[c], Reitner, Joachim[b, d]

[a] College of Tourism and Geographical Science, Leshan Normal University, Leshan, 614000, China.

[b] Department of Geobiology, University of Göttingen, Göttingen, 37077, Germany.

[c] Department of Geochemistry and Isotope Geology, University of Göttingen, Göttingen, 37077, Germany.

[d] Göttingen Academy of Science and Humanities in Lower Saxony. Göttingen, 37073, Germany

Correspondence to: Wanli Xiang (xiangwanli@lsnu.edu.cn) & Joachim Reitner (jreitne@gwdg.de)

Abstract

Carbonates (3.5 to 3.3 Ga) in the East Pilbara Terrane (EPT), Western Australia, including interstitial carbonate between pillow basalts, fracture-filling calcite, sedimentary carbonates and carbonate associated with stromatolites, provide valuable geochemical archives for reconstructing Early Earth environments. This study highlights three key findings: (1) Fracture-filling calcite D-2-W from the 3.48 Ga Dresser Formation acts as a proxy for Paleoarchean shallow seawater geochemistry. It exhibits high Sr (1789 μg/g), $\delta^{13}C$ (+2.20‰), $\delta^{18}O$ (-13.03‰), and age-corrected $^{87}Sr/^{86}Sr$ (0.700596), alongside low concentrations of rare earth elements (REE) and Y (briefly REE+Y), near-chondritic Y/Ho ratios, and shale-normalized REE+Y patterns characterized by heavy REE enrichment, positive La and Y anomalies, and absence of Ce and Eu anomalies. These features reflect a shallow marine setting likely influenced by anoxygenic photosynthetic processes and low-intensity volcanic-hydrothermal interactions. (2) EPT interstitial carbonates reliably trace Paleoarchean seafloor hydrothermal systems driven by basalt-seawater interactions. During hydrothermal alteration, water-rock reactions enriched carbonates in basalt-derived trace elements (Mg, Fe, Mn, light REE), lowered Sr and $\delta^{13}C$, and elevated $^{87}Sr/^{86}Sr$ and Eu/Eu*. (3) Post-depositional alterations of the interstitial carbonates exhibit distinct multi-element behaviors: recrystallization, often driven by low-temperature hydrothermal fluids, subtly shifts original geochemical compositions while preserving REE+Y patterns and $\delta^{13}C$ values. In contrast, ankeritization, induced by high-temperature fluids, resulting in significantly elevated abundances of basalt-derived elements, altered REE+Y patterns with middle REE enrichment and pronounced positive Eu anomalies, and markedly higher $^{87}Sr/^{86}Sr$ ratios. Consequently, this study challenges the classical paradigm of using singular isotopic proxies (e.g., $^{87}Sr/^{86}Sr$) to trace continental emergence, by establishing key geochemical fingerprints to discriminate between seawater and hydrothermal signatures in Archean carbonates. These insights provide critical calibration points for modeling early Earth ocean-tectonic evolution.

Keywords: Archean carbonate, Geochemistry, $^{87}Sr/^{86}Sr$, Archean seawater, Hydrothermal alteration.

1. Introduction

The geochemical composition of Paleoarchean seawater is still a subject of debate, due to the absence of pristine fluid inclusions or unaltered sedimentary archives older than 3.5 billion years (Ga). Previous works predict that the Paleoarchean ocean water composition was likely anoxic, ferruginous, phosphorus, sulfate-free, and dominated by hydrothermal processes (Veizer et al., 1989, 1992; Van Kranendonk et al., 2003; Rasmussen and Muhling, 2023; Pellerin et al., 2023; Rasmussen et al., 2024; Xiong et al., 2025). However, direct geochemical evidence has been obscured by post-depositional overprinting—particularly in carbonates where fluid-rock interactions mask primary signals (Veizer et al., 1989; Shields and Veizer, 2002; Van Kranendonk et al., 2003). Nonetheless, sedimentary carbonates are still regarded as the most valuable proxies for reconstructing past ocean conditions, as they integrate diagnostic elements from seawater during precipitation in various settings (Veizer, 1983; Smrzka et al., 2019). Thus, distinguishing pristine from secondary signatures is crucial for using carbonate as a proxy for past seawater compositions.

Two widely utilized approaches are microfacies analysis and geochemical techniques. Carbonate microfacies consistently reflect depositional and burial conditions (Flügel and Munnecke, 2010). Consequently, microfacies analysis, especially when combined with field geological studies such as mapping and profiling, provides compelling visual evidence of primary formation processes and subsequent alterations (Biswas, 1983; Flügel, 2004; Yarmohammadi et al., 2020; Abd-Elhameed et al., 2025). This makes it an indispensable prerequisite for conducting robust geochemical analyses. Geochemical approaches include the analysis of elemental compositions and isotopic signatures. More specifically, some major and trace elements behave mobile during alteration, allowing their abundance to estimate primary and secondary signatures. For instance, carbonate rock alteration results in an inverse Sr-Mn relationship, with progressive recrystallization leading to Sr loss and Mn gain (Veizer et al., 1989; Banner and Hanson, 1990). Due to the mobility of Sr in aqueous fluids, the primary primary $^{87}Sr/^{86}Sr$ ratios in carbonate minerals easily shift towards diagenetic fluid values. Post-depositional alteration nearly always changes the primary $^{87}Sr/^{86}Sr$ of carbonates (Veizer and Compston, 1974; Burke et al., 1982), with radiogenic fluid sources (e.g., clay minerals) increasing ratios, and juvenile volcanic sources or dissolution of less radiogenic minerals decreasing them (Shields and Veizer, 2002).

Despite these challenges, certain reliable tracers of depositional conditions, such as rare earth elements (plus yttrium, collectively referred to as REE+Y), can withstand later alteration and preserve original data (Parekh et al., 1977; Johannesson et al., 2006). Carbonate minerals, notably calcite, serve as long-term stores for lanthanides, incorporating them more effectively than other trace elements (Sabau et al., 2014). Significant loss of trace elements from the mineral lattice only occurs with complete mineral dissolution (Stipp et al., 2006). The resistance of REE+Y to alteration makes them valuable tools for reconstructing ancient environments and water sources (Bau and Dulski, 1996; Webb and Kamber, 2000; Kamber and Webb, 2001; Bolhar et al., 2005; Bau et al., 2010; Zhao et al., 2021).

Among REE+Y, Y and Ho, geochemical twins, typically behave coherently in environments, keeping Y/Ho ratios in igneous rocks and epiclastic sediments near 28 (Bau, 1996; Zhao et al., 2022), which approximates the chondritic value range of 26 to 27 (Pack et al., 2007). However, modern seawater and marine sedimentary carbonates from Archean and Paleoproterozoic eras show Y/Ho ratios exceeding 44 (Alibo and Nozaki, 1999; De Baar et al., 1985; Van Kranendonk et al., 2003; Kamber et al., 2004; Komiya et al., 2008; Planavsky et al., 2010; Luong et al., 2018), due to specific marine geochemical fractionation. Bau and Dulski (1999) attributed this to conservative Y near-vent mixing versus non-conservative Ho mixing during high-temperature hydrothermal fluid-seawater interaction, with Ho preferentially scavenged by Fe oxyhydroxides (Bau et al., 1996, 1998; Bau, 1999; Smrzka et al., 2019). Additionally, Ho is scavenged about twice as fast as Y due to differing complexation with inorganic (carbonate ions) and organic ligands, enriching Y in seawater (Nozaki et al., 1997; Zhang et al., 1994; Qu et al., 2009). In addition, Eu is redox-sensitive (Eu^{3+} in oxidizing and Eu^{2+} in reducing environments) and exhibits strong temperature dependence: above 250°C in reduced sulfur environments, nearly all Eu in acidic fluids is divalent (Sverjensky, 1984). Eu^{2+} has lower sorption affinity than Eu^{3+}, preferentially partitioning into the dissolved phase over trivalent REE neighbors (Bau, 1991; Bau and Möller, 1992). This decoupling is pronounced during high-T metamorphism (>250°C) under reducing conditions (Sverjensky, 1984; Bau, 1991, 1993; Bilal, 1991), yielding chondrite-normalized Eu/Eu* > 1 in high-T fluids and Eu/Eu* ≈ 1 in low-T fluids (<250°C) (Bau and Dulski, 1996). Thus, combining petrology and

geochemistry aids in identifying primary and secondary carbonate facies, recognizing depositional environments and assessing diagenetic alteration impacts.

Within carbonate facies, sedimentary carbonates (e.g., stromatolites) are favored as critical archives for reconstructing Paleoarchean seawater composition (Van Kranendonk et al., 2003; Allwood et al., 2010; Sugitani et al., 2015; Nutman et al., 2016; Viehmann et al., 2020; Hohl et al., 2024; Xiang et al., 2024). For example, stromatolitic carbonates in the Strelley Pool Formation (ca. 3.4 Ga; briefly SPF) exhibit a higher average $\delta^{13}C$ value (2.53 ± 1.11‰; Lindsay et al., 2005; Flannery et al., 2018; Xiang et al., 2024) compared to the near-constant seawater $\delta^{13}C$ of ~0‰ (Schidlowski, 1988), a positive deviation linked to restricted marine settings where photoautotrophic microorganisms in microbial mats sequestered ^{12}C, enriching environmental and carbonate ^{13}C (Melezhik et al., 2001; Arp et al., 2011; Xiang et al., 2024). These carbonates exhibit REE+Y patterns characteristic of anoxic seawater with hydrothermal influence, including smooth LREE depletion, no Ce anomaly, positive La, super-chondritic Y/Ho ratios, and pronounced positive Eu anomalies (Van Kranendonk et al., 2003; Viehmann et al., 2020), which align with sedimentological observations (Allwood et al., 2006a, 2007). However, multiple dolomite generations (Allwood et al., 2009; Flannery et al., 2018; Xiang et al., 2024) and reset Sm-Nd isotopes (Viehmann et al., 2020) indicate post-depositional alteration, potentially obscuring pristine seawater geochemistry.

Recent studies of interstitial carbonates in basalt interpillow spaces of the 3.53–2.83 Ga Pilbara Craton (Western Australia), formed through hydrothermal alteration of Archean oceanic crust, provide novel geochemical constraints on Archean seawater composition and crust-seawater interactions (Nakamura and Kato, 2002, 2004; Yamamoto et al., 2004; Lindsay et al., 2005; Shibuya et al., 2012; Marien et al., 2023; Xiang et al., 2024). Compared to stromatolites, these carbonates exhibit lower $\delta^{13}C$ values (-0.12 ± 1.76‰; Shibuya et al., 2012; Xiang et al., 2024) and similar REE+Y patterns but with higher total REE+Y concentrations and near-chondritic Y/Ho ratios (Nakamura and Kato, 2004; Yamamoto et al., 2004; Marien et al., 2023). Marien et al. (2023) distinguished two calcite types: (1) coarse-grained (Type I) with elevated Mn (478–14790 μg/g), high REE+Y, low Sr, and radiogenic $^{87}Sr/^{86}Sr(i)$, precipitated from boiling seawater trapped during pillow lava eruption; and (2) fine-grained (Type II) with lower Mn (13.7–420 μg/g), higher Sr (825–2516 μg/g), and $^{87}Sr/^{86}Sr(i)$ of 0.7010–0.7011 (3.34 Ga) and 0.70137 (3.12 Ga), formed from seawater in degassing spaces with minimal fluid-rock interaction. Most samples yield Sm-Nd isochron ages consistent with host rocks (Marien et al., 2023). Petrographic and in-situ geochemical analyses by Xiang et al. (2024) identified four interstitial carbonate facies: sparry calcite, acicular crystal-fan calcite, recrystallized blocky/massive sparry calcite, and ankerite. Their formation was driven by Mg-, Fe-, Al-, Si-, and Mn-enriched fluids derived from hydrothermal chlorite breakdown during basalt-seawater interactions. However, unaltered material identification and diagenetic correction remain essential for reconstructing depositional conditions and resolving the "complex and prolonged" diagenetic histories of marine carbonates (Bathurst, 1975; Fantle et al., 2020).

This study thus focuses on the geochemical diversity of Paleoarchean carbonates from the 3.53–3.17 Ga East Pilbara Terrane (EPT)—the Pilbara Craton's ancient nucleus and one of only two cratons preserving extensive, low-grade metamorphosed Paleoarchean exposures that contains Earth's oldest biosignatures, including microfossils and stromatolites (the other being the Kaapvaal Craton, southern Africa; Van

Kranendonk et al., 2002, 2008, 2019; Allwood et al., 2006a, 2007; Lepot, 2020). Facies-specific geochemical analyses (major/trace elements, REE+Y patterns, and age-corrected $^{87}Sr/^{86}Sr$) reveal insights into seawater composition, hydrothermal fluid chemistry during seawater-basalt interactions, and early Earth mantle-crust-ocean coupling. Post-depositional alteration effects were also quantified to refine future paleoenvironmental reconstructions.

2. Sampling information

2.1 Geological setting

The EPT evolved through a series of at least three mantle plume events: the Warrawoona event (3.53–3.42 Ga), Kelly event (3.35–3.29 Ga), and Sulphur Springs event (3.27–3.24 Ga), creating a complex volcanic plateau (Smithies et al., 2005; Huston et al., 2007; Van Kranendonk et al., 2002, 2006a, b, 2007a, b, 2015; Champion and Smithies, 2007; Pirajno, 2007a, b). These events resulted in a >20 km thick (ultra)mafic and felsic volcano-sedimentary succession, part of the Pilbara Supergroup (Fig. 1). Multiple tectonic models for Pilbara Supergroup volcanic rocks have been proposed (Glikson and Hickman, 1981; Hickman, 1983; Bickle et al., 1983, 1993; Barley et al., 1984; Barley, 1993; Arndt et al., 2001; Ueno et al., 2001; Kitajima et al., 2001; Kato and Nakamura, 2003), but recent studies favor an origin from discrete mantle melting events on older felsic crust (Van Kranendonk et al., 2002, 2007a, b, 2015; Hickman and Van Kranendonk, 2004; Van Kranendonk and Pirajno, 2004; Fischer and Gerya, 2016), with the dome-and-keel pattern forming North Pole Dome through granitic dome diapirism during crustal overturn (Van Kranendonk et al., 2019). The region's tectonic history marked by repeated uplift and deepening suggested by alternating geological features.

Figure 1: (a) Simplified geological map of the North Pole Dome, Eastern Pilbara Terrane, Western Australia, including sampling localities (red stars). (b) Simplified stratigraphy of the studied Archean rocks (Xiang et al., 2024; modified from Van Kranendonk and Hickman, 2000; Van Kranendonk et al., 2007b; Hickman and Van Kranendonk, 2012).

The Pilbara Supergroup was subdivided into four autochthonous groups: Warrawoona, Kelly, Sulphur Springs, and Soanesville groups (Van Kranendonk, 2006; Van Kranendonk et al., 2006a, 2007a, 2008, 2015, 2019). The Warrawoona Group (>12 km thick) consists of eight volcanic cycles capped by sedimentary units silicified by hydrothermal fluids (Hickman and Van Kranendonk, 2004; Van Kranendonk, 2006; Van Kranendonk et al., 2019). It includes pillowed basalts, komatiitic basalts, and felsic volcanic rocks, along with minor sedimentary units (Buick and Barnes, 1984; Lowe and Byerly, 1986; Thorpe et al., 1992; McNaughton et al., 1993; Byerly et al., 2002).

In the studied region, the oldest, basaltic North Star Basalt formation (3490 ±15 million years, Ma Ar/Ar) was overlain by the Dresser Formation with a U-Pb zircon age of 3481± 2 Ma (Van Kranendonk et al., 2008; Hickman and Van Kranendonk, 2012). This formation, a low-eruptive felsic caldera affected by syndepositional growth faults in a restricted marine setting, stands out for its remarkable preservation of subaerial epithermal features including geyserites and hot springs, which potentially harbor microbialite

fossils (Nijman et al., 1998; Van Kranendonk et al., 2008; Djokic et al., 2017, 2021; Baumgartner et al., 2019; Tadbiri and Van Kranendonk, 2020; Caruso et al., 2021). Overlying the Dresser Formation is an approximately 4 km thick mafic succession of the Antarctic Creek Member of the Mt Ada Basalt, with U–Pb zircon age of 3470 ± 2 Ma (Byerly et al., 2002; Hickman and Van Kranendonk, 2012). It underlies up to 1.3 km of felsic volcanic and volcaniclastic rocks of the Duffer and Panorama formations, and up to 150 m of the Marble Bar Chert Member of the Towers Formation in the far southeastern corner of the dome (Hickman and Van Kranendonk, 2012). The Apex Basalt, the stratigraphically youngest basaltic formation in the Warrawoona Group, has a depositional age ranging from 3463 to 3454 Ma, as constrained by zircon U-Pb ages from the underlying felsic Duffer Formation (Thorpe et al., 1992; McNaughton et al., 1993) and the overlying felsic Panorama Formation (Thorpe et al., 1992). The Strelley Pool Formation, with a detrital zircon U-Pb age of 3414 ± 34 Ma (Gardiner et al., 2019) and a carbonate Sm-Nd isotopic age of approximately 3253 ± 320 Ma (Viehmann et al., 2020), disconformably overlies the Panorama Formation. It comprises fluviatile to shallow marine conglomerates and quartzite, well-preserved stromatolitic marine carbonates of diverse macroscopic and microscopic forms, and some coarse clastic rocks, deposited on a carbonate platform that spanned the EPT (Lowe, 1983; Van Kranendonk et al., 2003; Van Kranendonk, 2006, 2007; Allwood et al., 2006a). This formation is conformably succeeded by the 3350-3335 Ma Euro Basalt, which includes a 1.5 km-thick basaltic komatiite unit and up to 5 km of overlying, interbedded komatiitic and tholeiitic basalts (Van Kranendonk et al., 2006a, 2019; Hickman and Van Kranendonk, 2012).

2.2 Sample description

The studied EPT carbonates comprise three distinct facies: ~3.5–3.4 Ga interstitial carbonates in pillow basalt interspaces, ~3.5–3.4 Ga bedded sedimentary carbonates, and ~3.4 Ga stromatolites. Sampling sites are marked on the EPT geological map, and their stratigraphic positions are shown in Figure 1. Detailed petrographic features, formation mechanisms, and depositional settings are fully described in Xiang et al. (2024) and summarized here.

Interstitial carbonates fall into four types: (1) primary, acicular crystal-fan calcite from the Apex Basalt (Fig.2a); (2) recrystallized/altered, blocky/massive/sparry calcite from the North Star, Apex, and Euro Basalts, and the Dresser Formation (Fig.2b, c); (3) blocky ankerite from the North Star and Mt Ada Basalts (Fig.2d); (4) fracture-filling sparry calcite from the Dresser Formation (Fig.2e). These carbonates likely precipitated abiotically from high-alkalinity hydrothermal fluids generated by seawater-basalt interactions.

Figure 2: Thin-section photomicrographs from the North Pole Dome, Eastern Pilbara Terrane (Western Australia). The samples reveal four distinct types of interstitial carbonates: (1) primary facies: the acicular crystal-fan calcite (a); (2) recrystallized/altered facies: blocky calcite (b) and massive calcite and sparry calcite (sparite) in (c); (3) The blocky ankerites often exhibiting the calcite overgrowth; (4) Fracture-filling calcite precipitated in wide fractures. Sedimentary carbonates include two types, namely marine ankerite associated with organic matter (f, g) and terrestrial hydrothermal dolomite-calcite assemblages (h). (I, j) show stromatolite from the Strelley

Pool Formation displays tri-generational dolomite, with initial generation (D1) partially recrystallized into subsequent generations (D2-D3). Samples (a-c) derive from the Apex Basalt, (d) from Mt Ada Basalt, and (e, f-h) from the Dresser Formation. All photographs were taken under plane-polarized light except (b, c) under cross-polarized light and (j) under Cathodoluminescence. Scale bars in (a, f-h) are 200 µm (also applies to b-e, i), whereas the scale bar in (j) is 25 µm. (Mineral abbreviation: Cal-calcite, Qtz- quartz, Ank-ankerite, Dol-dolomite).

Bedded sedimentary carbonates include two types: one is mainly ankerite closely associated with organic matter and chert from the Dresser Formation and Euro Basalt (Fig.2f, g); the other is dolomite-calcite from the Dresser Formation (labeled as DB in Table 1; Fig.2h). These carbonates formed through organomineralization, with varying hydrothermal influences: DB likely originated in a subaerial hydrothermal pond, while others formed in shallow marine settings with minor hydrothermal input.

The stromatolite sample consists of three generations of dolomite cemented by chert from the Strelley Pool Formation (Fig.2i, j), indicating microbial extracellular polymeric substance (EPS)-mediated biomineralization in shallow marine environments.

3. Methods

3.1 Sample preparation

Samples were prepared via two approaches. Homogeneous whole-rock samples, including bedded sedimentary carbonates (Tsu and DB) and stromatolite (Strelley), were fully pulverized and homogenized using an agate ball mill. For the remaining samples, mineral facies were selected based on petrographic observations. Small cylinders (~1 cm in diameter, devoid of visible alteration, inclusions, or secondary porosity) were drilled from rock sections, ultrasonically cleaned in ethanol three times, air-dried at room temperature, and then crushed into fragments. These carbonate fragments were hand-selected and ground to powder in an agate mortar.

A sequential leaching protocol was employed to isolate the carbonate fraction and minimize contamination, using ultrapure reagents throughout. Carbonate powder (~50 mg) was digested overnight in ~0.3 M HNO_3 within Teflon beakers at room temperature, followed by centrifugation to separate supernates and potential precipitates. The supernates were dried at 80 °C, while precipitates were dried at 60 °C. To eliminate organic contaminants that could interfere with precise measurements, dehydrated supernates were dissolved in 0.2 mL concentrated HNO_3 at 80 °C for 2 h, sequentially treated with 0.2 mL H_2O_2 for 15 h and 0.2 mL 6 M HCl for 2 h, and then dried at 80 °C. The residue was refluxed in 1.2 mL 3 M HNO_3, centrifuged to isolate supernates and insoluble fractions, and the supernates were dried again for further analysis. Insoluble fractions from both centrifugation steps were weighed to determine the mass of the analyzed sample and dissolved fractions. Carbonate geological reference materials (Jls-1, JDo-1, Cals-1; Table A.1) and procedural blanks were processed alongside samples to ensure reproducibility and quality control. All procedures and measurements were conducted at the Geoscience Center, University of Göttingen.

3.2 Elemental concentrations

Major and minor element concentrations were determined using an Agilent 5100 VDV inductively coupled plasma-optical emission spectrometer (ICP-OES). Aliquots of digested sample solutions were diluted to 10 mL in a 2 wt% HNO_3 + 0.5 wt% HCl matrix, and dilution factors were calculated gravimetrically. Calibration was performed by measuring a blank solution and six multi-element calibration standards. Measurements of international reference materials (Jls-1, JDo-1, Cals-1) bracketed sample analyses, with standard deviations of Jls-1 and JDo-1 used to estimate measurement precision for calcite and dolomite, respectively. Seven procedural blanks were analyzed periodically, and their mean value was subtracted from each calibrated measurement before applying individual dilution factors.

Trace element concentrations in the samples were determined using a Thermo Fisher Scientific iCAP Q ICP-MS equipped with an Apex desolvating nebulizer and PFA spray chamber. Aliquots of digested samples were dried, dissolved in 0.4 M HNO_3–0.05 M HF, and diluted gravimetrically to a final ~5000× factor via two-step dilution. The method utilized an internal standard (containing 100 ng/g ^{9}Be, 10 ng/g ^{115}In, and 10 ng/g ^{209}Bi), multi-element external calibration standards, and 20 ppb Ba, Nd, Pr standard solutions to correct spectral interferences (e.g., $^{135}Ba^{16}O^{+}$ on $^{151}Eu^{+}$, $^{141}Pr^{16}O^{+}$ on $^{157}Gd^{+}$, $^{146}Nd^{16}O^{+}$ on $^{162}Dy^{+}$). Oxide formation (<0.6% CeO/Ce) was negligible. Reference materials (Cal-s, JLs-1, JDo-1) were analyzed every five samples to monitor data quality. Long-term precision and accuracy for rare earth elements (REEs) were <10% (RSD), except for Sm, Eu, Gd in JLs-1 (accuracy <20%; Table A.1). Only elements with <10% accuracy were used to correct matrix effects and instrumental drift (not addressed by internal standardization); JLs-1 and JDo-1 served as references for calcite and dolomite, respectively.

All REE and Y concentrations are normalized to Post-Archean Australian Shale (PAAS; subscript SN, after Pourmand et al., 2012), which reflects the composition of weathered and recycled terrigenous material derived from the continental crust (Taylor and McLennan, 1985). Anomalous behaviors are quantified using the following equations:

$Ce/Ce^* = Ce_{SN}/(0.5Pr_{SN} + 0.5La_{SN})$, $Pr/Pr^* = Pr_{SN}/(0.5Ce_{SN} + 0.5Nd_{SN})$ (after Bau and Dulski, 1996) ;

$La/La^* = La_{SN}/(3Pr_{SN} - 2Nd_{SN})$ and $Gd/Gd^* = Gd_{SN}/(2Tb_{SN} - Dy_{SN})$ (after Alexander et al., 2008);

$Eu/Eu^* = Eu_{SN}/(Sm_{SN}^2 * Tb_{SN})^{1/3}$ and $Y/Y^* = Y_{SN}/(0.5Er_{SN} \times 0.5Ho_{SN})$ (after Lawrence et al. 2006).

The widespread positive La anomaly in Archean samples may affect Ce anomaly calculations; thus, the validity of the revised Ce/Ce* equation is assessed by cross-plotting with Pr/Pr*. Light-to-heavy REE ratios in Archean carbonates are expressed as Pr_{SN}/Yb_{SN} (Planavsky et al., 2010), while Sm_{SN}/Yb_{SN} is used here to reflect middle-to-heavy REE ratios, rather than LREE depletion as suggested by Kamber and Webb (2001). To compare Y and REE behaviors, Y (+3: 1.02 Å) is positioned between Dy (+3: 1.03 Å) and Ho (+3: 1.02 Å) (ChemGlobe, 2026) in PAAS-normalized REE+Y patterns. Y's anomalous

behavior relative to REEs is evaluated using non-normalized Y/Ho weight ratios, reflecting their ionic radius similarity (Bau and Dulski, 1996).

3.3 Radiogenic Sr isotopic composition

Aliquots of sample solutions and reference materials (JLs-1 and JDo-1) were spiked with ^{87}Rb-^{84}Sr tracer solutions. The spiked aliquots were dried, dissolved in 3.0 mL 2.5 M HCl, and subjected to cation exchange chromatography using BioRad AG 50×8 (200–400 mesh) resin to separate Rb and Sr from matrix elements. The Rb fraction was collected, dried, dissolved in 0.5 M HNO_3. Concentrations of Rb were determined on a ThermoFisher Scientific ELEMENT2 mass spectrometer using an ID-SF-ICPMS technique as described in Willbold and Jochum (2005). The Sr fraction was further purified with Triskem Sr-spec resin (50–100 μm) to eliminate residual ^{87}Rb interference on ^{87}Sr during mass spectrometry, following the method of Pin et al. (2014). Measurements were performed on a ThermoFisher Scientific Neptune Plus MC-ICP-MS equipped with a Teledyne Cetac Aridus3 desolvation system. Sr isotope ion currents were measured with 10^{11} Ω amplifiers, while interfering isotopes (e.g., ^{83}Kr and ^{85}Rb for Sr) were monitored using 10^{12} Ω amplifiers. NIST SRM 987 was analyzed every five samples, followed by reference materials and procedural blanks. The $^{86}Sr/^{88}Sr$ ratio was normalized to 0.1194 using an exponential law. After offline correction implementing the double isotope dilution equation of Boelrijk (1968), the long-term mean $^{87}Sr/^{86}Sr$ ratio for NIST SRM 987 is 0.710246 ± 0.000009 (2σ, n = 65 over 60 months). The $^{87}Sr/^{86}Sr$ ratios for JDo-1 and JLs-1 are 0.707575 ± 0.000028 (2σ, n = 2) and 0.707847 ± 0.000019 (2σ, n = 2), respectively, whereas repeated long-term digestions and measurements of the basaltic geological reference material JB-2 yielded $^{87}Sr/^{86}Sr$ of 0.703675 ± 0.000006 (2σ, n = 9 over 60 months). Further details regarding the analytical technique can be found in Hegner et al. (2020).

4. Results

Table 1 presents the concentrations of major and trace elements, along with PAAS-normalized REE+Y anomalies, in EPT carbonates. The dissolved mass fraction is the mass ratio of the dissolved to weighed sample. For the interstitial carbonates studied, lower dissolved mass fractions indicate more quartz cement or post-deposition veins. Most interstitial carbonates have dissolved mass fractions >70 wt%, except D-1 and E-3. In contrast, whole-rock samples of bedded sedimentary carbonates and SPF stromatolites have lower mass fractions (down to 16.5 wt%) due to significant amounts of chert matrix. A highly silicified SPF stromatolite sample (SHAW), with an extremely low dissolved mass fraction (0.37 wt%), is excluded from most analyses but included for its REE+Y pattern.

Table 1: Geochemical compositions of the various carbonates from the East Pilbara Terrane, Western Australia

4.1 Major and trace elements

Based on major and trace element data (Table 1) and carbonate rock classification (Fig.3a), the primary interstitial calcite averages 39.5 ± 0.8 wt% Ca, 0.5 ± 0.3 wt% Mg, 1.4 ± 0. 7 wt% Fe, and 0.8 ± 0.1 wt%

Mn. The altered interstitial calcite exhibits comparable Ca (40.8 ± 0.8 wt%) and Mn (0.8 ± 0.2 wt%) but lower Mg (0.2 ± 0.1 wt%) and Fe (0.5 ± 0.3 wt%). The interstitial ankerite averages 25.1 ± 3.8 wt% Ca, 6.5 ± 1.5 wt% Mg, 8.8 ± 1.3 wt% Fe, and 0.7 ± 0.2 wt% Mn. The fracture-filling calcite contains 42.2 ± 0.0 wt% Ca and trace amounts of Mg (≤0.2 wt%), Fe (≤0.1 wt%), and Mn (~ 0.0 wt%). Sedimentary carbonates are primarily ankerite, with averages of 22.8 ± 2.3 wt% Ca, 8.6 ± 1.6 wt% Mg, 9.8 ± 2.0 wt% Fe, and 1.1 ± 0.2 wt% Mn, except for calcite-dominated sample DB (36.6 wt% Ca, 2.3 wt% Mg, 0.2 wt% Fe, and 0.2 wt% Mn; possibly with minor dolomite). SPF stromatolites consist of dolomite (22.7 wt% Ca, 12.0 wt% Mg, 1.7 wt% Fe, and 0.4 wt% Mn). Sr is highly enriched in fracture-filling calcite, ranging from 1198.5 to 1789.3 μg/g (1493.9 ± 417.8 on average), while its levels are far lower in interstitial carbonates (the primary 119.1 ± 17.3 μg/g, the altered 89.4 ± 26.7 μg/g, ankerite 151.3 ± 86.3 μg/g, on average), sedimentary carbonates (60.2 ± 41.2 μg/g on average), and stromatolites (47.8 μg/g).

Figure 3: (a) Carbonate rock classification based on converted $CaCO_3$-$MgCO_3$-$(Fe+Mn)CO_3$ compositions (wt%). It reveals that the EPT carbonates mainly comprise calcite, dolomite, and ankerite. Cross-plots of EPT carbonates display molar Mg/Ca ratio vs. (b, c) Fe (wt%), (d) Mn (wt%), and (e) Sr (μg/g), revealing varied Fe, Mn, and Sr levels across carbonate facies. The dashed square in (b) is enlarged in (c), with grey lines and envelope indicating strong Fe-lithology correlations, suggesting dissolved Fe mainly from carbonates. Data on interstitial carbonates are sourced from Nakamura and Kato (2004), Yamamoto et al. (2004), and Marien et al. (2023), while sedimentary carbonate and stromatolite data come from Viehmann et al. (2020). (Abbreviations: Cal. –calcite; P-primary; A-altered; Carb. -carbonate; SPF- Strelley Pool Formation; ref-reference).

Plots of molar Mg/Ca ratio against Fe, Mn, and Sr concentrations show variable levels of these elements across EPT carbonate facies (Fig. 3b-e). Samples of primary and altered interstitial calcites, marine sedimentary carbonates, and SPF stromatolites exhibit a strong lithological control on Fe (wt%) that its linear variation with the molar Mg/Ca ratio in calcite and dolomite facies. This suggests that dissolved Fe primarily originates from carbonates rather than other minerals. However, considering petrological findings (Xiang et al., 2024), large deviations in interstitial ankerite and sample DB may stem from ankerite-calcite mixing and iron oxide contamination, respectively, which may also explain deviations in some other carbonates and stromatolites (Nakamura and Kato, 2004; Yamamoto et al., 2004; Viehmann et al., 2020; Marien et al., 2023). Regarding Mn and Sr, fracture-filling calcite shows notably higher Sr but lower Mn, while other carbonate facies display no correlation and significant differences.

Some diagnostic trace element concentrations (Fig.4) are briefly introduced below (excluding outliers). Interstitial carbonates have consistently low Al contents, ranging from 0.00 to 0.07 wt% (0.02 wt% on average). Sedimentary carbonates show a similar Al range but a higher mean (0.07 ± 0.05 wt% on average), while fracture-filling calcite and SPF stromatolites have negligible Al. Sc concentrations rise in the order (on average): fracture-filling calcite (0.25 μg/g), interstitial ankerite (0.72 μg/g), stromatolite (1.81 μg/g), altered interstitial calcite (2.31 μg/g), primary interstitial calcite (2.45 μg/g), and sedimentary carbonate (8.36 μg/g). A similar trend is seen for Ti, likely in anatase (Xiang, 2023), with averages increasing from 0.07 to 4.83 μg/g. Ba, often of hydrothermal origin, is lower in interstitial carbonates (9.26 μg/g on average) and higher in sedimentary carbonates and stromatolites (67.58 μg/g on average).

The extremely high Ba (4594.74 μg/g) in DB is due to its location atop bedded barite layers. Rb is generally low in carbonates: interstitial carbonates (0.04 μg/g on average), fracture-filling calcite (0.01 μg/g), stromatolites (0.06 μg/g), and sedimentary carbonates (0.67 μg/g).

Figure 4: Plots showing trace element concentrations (Al in wt%, others in μg/g) in the EPT carbonates. The SPF stromatolite and the Paleoarchean seawater endmember (D-2-W, details in Section 5.2.1) are marked by diamond and star, respectively. (Abbreviations: Cal. –calcite; P-primary; A-altered; Ank.-ankerite; Carb. -carbonate).

4.2 Rare earth elements and REE+Y patterns

Figure 5 displays the PAAS-normalized REE+Y patterns across different stratigraphic layers whereas in Figure 6, selected trace element ratios are present.

Figure 5: The PAAS-normalized REE+Y patterns of EPT carbonates and referenced counterparts, stratigraphically organized. (a) North Star Basalt, (b) Dresser Formation, (c) Mt Ada Basalt, (d) Apex Basalt, (e) Strelley Pool Formation, and (f) Euro Basalt. Abbreviations: "ICal" denotes interstitial calcite (P = primary facies, A = altered facies); "IAnk" indicates interstitial ankerite; "Sed Carb" represents sedimentary carbonate; "FFCal" refers to fracture-filling calcite. "ICal-I" and "ICal-II" are Type I and II interstitial carbonates from Ref.2; "Carbi" in (f) denotes carbonate inclusions in Euro pillow basalt margins (Ref.7). "Ref-X" indicates data from reference X, while "Ref-X.mv" represents the mean of referenced data in Figure A.1. References: Ref.1 - Van Kranendonk et al. (2003); Ref.2 - Marien et al. (2023); Ref.3 - Nakamura and Kato (2004); Refs.4-6 - Van Kranendonk et al. (2003), Allwood et al. (2010), Viehmann et al. (2020); Ref.7 - Yamamoto et al. (2004).

Figure 6: Plots of diagnostic REE+Y ratios and the PAAS-normalized REE+Y anomalies for EPT carbonates and references. (a) Y/Ho weight ratios, (b) Y/Y*, (c) Eu/Eu* vs. total REE+Y (μg/g), (d) Ce/Ce* vs. Pr/Pr*, (e) Gd/Gd vs. La/La*, and (f) Sm/Yb_{SN} vs. Pr/Yb_{SN}. These reveal that EPT carbonates generally exhibit near-chondritic or elevated Y/Ho ratios, no Ce anomaly, and positive La, Eu, and Y anomalies, along with LREE depletion. Reference data are sourced from Van Kranendonk et al. (2003), Nakamura and Kato (2004), Yamamoto et al. (2004), Allwood et al. (2010), Viehmann et al. (2020) and Marien et al. (2023). (Abbreviations: Cal. – calcite; P – primary; A – altered; Carb. – carbonate; SPF- Strelley Pool Formation; ref.- reference).

Total REE+Y concentrations increase from fracture-filling calcite (2.27 ± 0.05 μg/g) and stromatolite (4.43 μg/g) to sedimentary carbonates (41.54 ± 9.87 μg/g). Interstitial carbonates, however, display a wide range of concentrations due to sparse data availability: primary interstitial calcite ranges from 23.32 to 142.95 μg/g, altered interstitial calcite from 13.19 to 399.79 μg/g, and interstitial ankerite from 18.10 to 128.68 μg/g.

Absolute Y/Ho ratios are relatively consistent across most samples, with primary interstitial calcite showing 32.86 ± 2.94, altered interstitial calcite 35.24 ± 4.90, interstitial ankerite 33.53 ± 4.61, fracture-

filling calcite 33.53 ± 4.30, and sedimentary carbonates 31.38 ± 2.34. The stromatolite sample stands out with a significantly higher Y/Ho ratio of 46.50, suggesting a unique geochemical signature.

Average Y/Y* ratios vary more widely, with primary interstitial calcite at 1.57 ± 0.98, altered interstitial calcite at 2.08 ± 1.50, interstitial ankerite at 4.07 ± 5.13 (ranging from 0.87 to 11.68), and sedimentary carbonates at 1.63 ± 0.60. Fracture-filling calcite and stromatolite exhibit even higher values of 21.49 ± 0.21 and 28.49, respectively, indicating distinct Y anomalies in these samples.

The Eu/Eu* ratios increase from fracture-filling calcite with a ratio of 1.18 ± 0.19, the ratios increase through primary (1.69 ± 0.20) and altered (1.58 ± 0.36) interstitial calcites, with a maximum in interstitial ankerite (2.99 ± 1.00). Sedimentary carbonates (2.30 ± 0.60) and stromatolite (2.32) fall within the range observed for ankerite, indicating a similar degree of Eu anomaly.

Ce/Ce* ratios are relatively uniform, with primary interstitial calcite at 1.04 ± 0.03, altered interstitial calcite at 1.08 ± 0.06, interstitial ankerite at 0.95 ± 0.08, fracture-filling calcite at 1.06 ± 0.01, and sedimentary carbonates at 0.98 ± 0.06 (excluding the outlier DB with a value of 0.36). Stromatolite shows a Ce/Ce* ratio of 1.03, consistent with the other samples.

La/La* anomalies present a diverse range: primary interstitial calcite at 2.10 ± 0.39, altered interstitial calcite at 2.07 ± 0.67, interstitial ankerite at 0.70 ± 1.21, fracture-filling calcite at 2.26 ± 0.04, sedimentary carbonates at 2.63 ± 1.01, and stromatolite at 5.00.

Pr_{SN}/Yb_{SN} ratios also exhibit a wide range, with primary interstitial calcite from 0.07 to 0.16, altered interstitial calcite from 0.07 to 0.38, interstitial ankerite from 0.22 to 1.48, fracture-filling calcite from 0.04 to 0.13, sedimentary carbonates from 0.08 to 0.72, and stromatolite at 0.2. Similarly, Sm_{SN}/Yb_{SN} ratios vary from primary interstitial calcite (0.17 to 0.48), altered interstitial calcite (0.12 to 0.83), interstitial ankerite (1.12 to 3.04), fracture-filling calcite (0.11 to 0.35), sedimentary carbonates (0.24 to 1.41), to stromatolite (0.72). The feature of Pr_{SN}/Yb_{SN} and $Sm_{SN}/Yb_{SN} < 1$ indicates that most of these carbonates show HREE enrichment, and interstitial ankerite displays MREE enrichment, while partial sedimentary carbonates may exhibit LREE depletion, consistent with their REE+Y pattern shapes (Fig.5).

Overall, EPT carbonates exhibit HREE enrichment, no Ce anomaly, slight La and Gd positivity, and strong positive Eu and Y anomalies, consistent with prior studies (Fig. 5, 6; Van Kranendonk et al., 2003; Nakamura and Kato, 2004; Yamamoto et al., 2004; Allwood et al., 2010; Viehmann et al., 2020; Marien et al., 2023). However, some exceptions exist: CP-1 (highest REE+Y) shows only a positive Eu anomaly, while three low-REE+Y Dresser Formation samples exhibit only Y anomalies (Fig. 5a, b). A decline in Y anomalies with increasing total REE+Y is observed, but no clear correlation exists for Eu anomalies (Fig. 6a-c). Notably, the convex REE+Y pattern with MREE enrichment and strong Eu positivity is also seen in highly silicified SPF stromatolite (SHAW), which combines features of its less altered counterpart and Mt Ada interstitial ankerite (Fig. 6a-c).

4.3 Stable $\delta^{13}C_{VPDB}$, $\delta^{18}O_{VPDB}$ and radiogenic $^{87}Sr/^{86}Sr$ isotopes

The carbon and oxygen isotopic compositions of various carbonate types are listed in Table 1 with data sourced from Xiang et al. (2024). Average $\delta^{13}C_{VPDB}$ values increase sequentially: altered interstitial calcite registers the lowest at -0.29 ± 1.30‰, followed by interstitial ankerite at 0.53 ± 0.38‰, primary interstitial calcite at 0.63 ± 0.12‰, sedimentary carbonate at 1.39 ± 0.38‰ (with the notable exception of sample DB at -5.10‰), fracture-filling calcite at 2.27 ± 0.10‰, and stromatolite peaking at 2.50‰. For $\delta^{18}O_{VPDB}$, interstitial carbonates show lower values: primary (-16.70 ± 0.56‰), altered (-18.71 ± 0.99‰), ankerite (-16.77 ± 1.96‰), fracture-filling (-15.42 ± 3.38‰); sedimentary carbonate is -14.62 ± 1.4‰ (except DB at -7.88‰), and stromatolite is -13.16‰.

Table 2 presents age-corrected radiogenic Sr isotopic compositions of EPT carbonates. Fracture-filling calcites exhibit the lowest $^{87}Sr/^{86}Sr$ ratios (0.700596), comparable to Dresser barites (McCulloch, 1994; Chen et al., 2022), suggesting a plausible 3.5 Ga seawater origin. Primary interstitial calcites range from 0.701796 to 0.704172 (mean: 0.703094 ± 0.000979), while altered interstitial calcites are slightly higher (0.701917–0.706543; mean: 0.704306 ± 0.001725). Interstitial ankerites show a broader range (0.705341–0.712832; mean: 0.708688 ± 0.003115). Sedimentary carbonates vary widely (0.702203–0.715458; mean: 0.709158 ± 0.004810), exceeding interstitial calcites and aligning with interstitial ankerite. SPF stromatolites have an intermediate ratio (0.705217).

Table 2: The age-corrected radiogenic Sr isotopic compositions of the EPT carbonates.

5. Discussion

5.1 Clastic Contamination

Even trace amounts of clastic or terrigenous components can alter the REE+Y patterns and Sr isotopic compositions of carbonates due to the contrasting REE+Y concentrations between shale (high) and carbonate (low) (Kamber and Webb, 2001). However, this study minimized the effect of clastic contamination through several measures. Firstly, petrographic analysis of thin sections revealed no textural evidence or detrital material. Secondly, the use of micro-drilling for interstitial carbonates and chemical separation with low-concentration HNO_3 at room temperature significantly reduced potential silicate dissolution. Thirdly, systematic relationships between Fe contents and Mg/Ca molar ratios indicated that soluble Fe originated from calcite or ankerite, not iron silicates or (oxy)hydroxides (Fig. 3b, c).

To further support the absence of clastic components, multiple parameters were evaluated. The minor dissolution of detrital contaminants (typically aluminosilicate minerals) can elevate Al, Th, Sc, and Zr concentrations in leachates. Accordingly, positive correlations between Al and these elements were used to identify terrigenous detrital contamination (Webb and Kamber, 2000; Nothdurft et al., 2004; Ling et al., 2013). Empirical "cut-off values" such as 2000 μg/g Al and 5 μg/g Zr (Schier et al., 2018), and 0.5 μg/g Th and 2 μg/g Sc (Ling et al., 2013) were applied. In this study, most samples (except two interstitial

calcites) had Al contents below 2000 μg/g, unrelated to inferred silicate contents. Zr and Th concentrations in all samples were below empirical thresholds, though some samples had higher Sc concentrations. However, the lack of systematic correlations between Al and other elements points against detrital contamination (Fig. 7).

Figure 7: Plots of Al content (wt%) versus the concentrations (μg/g) of (a) Sc, (b) Th, (c) Zr, (d) Ti, (e) Rb, and (f) total REE to evaluate potential detritus contamination. The grey dashed line represents the binary mixing line between seawater endmember D-2-W and the EPT basalt endmember (mean value, MV), while another line shows the binary mixing line between D-2-W and the MUQ endmember, with grey numbers indicating the weight fractions of basalt or MUQ (methods in Appendix A) The plots reveal that only a few sedimentary carbonates may have been slightly affected by detritus, with contamination fractions up to 0.03. (Abbreviations: Cal. – calcite; P – primary; A – altered; Ank. – ankerite; Carb. – carbonate; SPF – Strelley Pool Formation).

Binary mixing lines (Fig. 7; methods in Appendix A) between Paleoarchean seawater (D-2-W), average Paleoarchean EPT basalt compositions (data from Van Kranendonk and Pirajno, 2004; Yamamoto et al., 2004; Nakamura and Kato, 2004; Smithies et al., 2005; Jenner et al., 2009; Johnson et al., 2017; Nakamura et al., 2020; Tusch et al., 2021; Tympel et al., 2021; Caruso et al., 2021), and MUQ (Mud from Queensland, Kamber et al., 2005) further support the scarcity of dissolved components from basaltic rocks and weathered crust. Most EPT carbonates deviated significantly from these mixing lines, indicating minimal volcanic detritus. Sedimentary carbonates, however, showed higher Th and Rb levels closer to the MUQ mixing line, Ti near the basalt line, and Zr near both, suggesting a potential detrital input of approximately 1.5% (maximum 3%). Yet, this minor fraction would not significantly alter the REE+Y patterns of sedimentary carbonates, as demonstrated by subtracting 3% of the average EPT basalt and MUD compositions from the sedimentary carbonate mean value based on the binary mixing model (Fig. 8).

Figure 8: PAAS-normalized REE+Y patterns for EPT carbonates and referenced data showing mean values and ranges across lithologies: (a) primary interstitial calcite (Primary ICal.), altered recrystallized interstitial calcite (Recryst. ICal.), interstitial ankerite (Ank.), and fracture-filling calcite (Fracture Cal.); (b) sedimentary carbonates (Carb.) and Strelley Pool Formation (SPF) stromatolites (dashed blue line: highly silicified counterpart of stromatolite). The orange dashed line represents a 3% reduction from the sedimentary carbonate mean, based on a binary mixing model, indicating maximum basalt detritus contribution (Fig.7). Similarly, the brown dashed line reflects a 3% MUD composition reduction. The mean REE+Y patterns normalized to Primitive Mantle (PM; Palme and O'Neil, 2014) are shown for (c) EPT carbonates and (d) modern references (note: true values ×10⁶ on log y-scale). In (c), mean values of carbonates from the Euro pillow basalt margin ("Euro Carb(i)", Yamamoto et al., 2004) and Type-I and II interstitial carbonates ("Euro ICarb-I" and "Euro ICarb-II", Marien et al., 2023) are plotted. All lines illustrate a distinct shift from seawater to interstitial carbonates. Abbreviations in (d): HT – High Temperature; LT – Low Temperature; NPDW – North Pacific Deep Water; NPSW – North Pacific Surface Water. Data sources: a. Hongo and Nozaki (2001); b. Bau and Dulski (1999); c. Alibo and Nozaki (1999).

Thus, experimental methods, diagnostic element correlations, and binary mixing models confirm that the studied EPT carbonates are largely free from clastic influence, making their geochemical compositions reliable proxies for further discussion.

5.2 Primary Geochemical Proxies of Paleoarchean Marine Fluids

Based on diagnostic geochemical signatures (e.g., REE+Y patterns, $\delta^{13}C$ and $^{87}Sr/^{86}Sr$ ratios), two distinct pristine carbonate facies can be distinguished that precipitated respectively from surface seawater and low-temperature hydrothermal fluids, respectively.

5.2.1 Surface Seawater Composition Recorded in High-Strontium Calcite

Among interstitial carbonates, fracture-filling calcite stands out as it precipitates from fluids circulating through fractures in the basaltic basement, possibly leading to recrystallization of earlier interstitial carbonate formed from seawater-derived hydrothermal fluids. Three pieces of evidence suggest its parent fluids are plausible representatives of Paleoarchean seawater.

Firstly, fracture-filling calcite exhibits seawater-like carbon isotopic compositions. Xiang et al. (2024) observed a decreasing $\delta^{13}C$ trend among EPT carbonates, from the SPF stromatolites (3.08 ± 0.30‰), marine sedimentary carbonates (1.85 ± 0.48‰), to interstitial carbonate (0.22 ± 0.98‰), aligning with reference data (Lindsay et al., 2005; Flannery et al., 2018; Shibuya et al., 2012; Nakamura and Kato, 2004). This trend arises from the mixing of seawater and mantle-derived CO_2. In restricted marine settings, photoautotrophs sequester ^{12}C, enrich environmental ^{13}C and lead to positive $\delta^{13}C$ values in marine carbonates (Melezhik et al., 2001; Arp et al., 2011; Xiang et al., 2024). As hydrothermal and mantle CO_2 mixing increases, carbonates precipitate with lower $\delta^{13}C$. Fracture-filling calcite shows an average $\delta^{13}C$ of 2.27 ± 0.10‰, within the range of stromatolites and marine sedimentary carbonates, suggesting its formation in a shallow marine environment influenced by microbial activity and minimal hydrothermal input.

Secondly, the unique seawater-like REE+Y pattern of fracture-filling calcite indicates that it retains original Paleoarchean ocean signatures, at least regionally. Its REE+Y concentrations are significantly lower than other interstitial and sedimentary carbonates, and slightly lower than SPF stromatolites (Fig. 8). This calcite exhibits HREE enrichment, lacks Ce but shows positive La and Y anomalies, aligning with SPF stromatolite patterns except for near-chondritic Y/Ho ratios and the absence of Eu anomaly (Figs. 6, 8). Super-chondritic Y/Ho ratios (>44) are common in marine sedimentary carbonates and SPF stromatolites (Fig. 6b; Van Kranendonk et al., 2003; Allwood et al., 2010; Viehmann et al., 2020), as Ho and other REEs are scavenged by particulate matter (inorganic and organic) or iron (oxy)hydroxides (Nozaki et al., 1997; Bau and Dulski, 1999; Qu et al., 2009; Smrzka et al., 2019). Conversely, the near-chondritic Y/Ho ratios (33.53 ± 4.30) in fracture-filling calcites result from the lack of iron (oxy)hydroxides (Fe and Mn mainly in the calcite lattice) and particulate matter. Its positive Y/Y* anomalies (21.49 ± 0.21) are much higher than in other interstitial carbonates (up to 11.68) and closer to that in SPF stromatolite (28.49), pointing to a seawater origin. Additionally, it displays a subparallel

REE+Y pattern and lower concentrations compared to Type-II carbonates, which likely precipitated from hot seawater circulating through degassing spaces in pillow Euro basalts, preserving typical seawater-like REE+Y systematics (Marien et al., 2023). Marien et al. (2023) noted that even minor (<1%) hydrothermal fluid or fluid-rock interaction can markedly shift the composition of seawater-derived carbonates to produce the observed REE+Y pattern in calcite. Additionally, when normalized to PM, fracture-filling calcite closely mirrors the modern marine REE+Y pattern, except for the negative Ce anomaly (Fig. 8d; Alibo and Nozaki, 1999; Hongo and Nozaki, 2001), reinforcing its seawater origin with negligible hydrothermal alteration.

Thirdly, the remarkably low $^{87}Sr/^{86}Sr$ ratios of fracture-filling calcite provide compelling evidence for its seawater origin. A widely accepted principle in seawater Sr isotope studies is that the lowest $^{87}Sr/^{86}Sr$ ratios offer the most reliable maximum estimate of contemporaneous seawater values (Veizer and Compston, 1974; Burke et al., 1982). However, nearly all ~1000 Precambrian carbonate samples in the Precambrian Marine Carbonate Isotope Database (PMCID) have undergone post-depositional alteration, skewing their $^{87}Sr/^{86}Sr$ ratios to higher values (Shields and Veizer, 2002). Consequently, barite $^{87}Sr/^{86}Sr$ ratios have been used as a proxy for seawater radiogenic Sr isotopic composition, yielding a minimum value of 0.700447 at ~3.5 Ga (from Dresser Formation barites; Chen et al., 2022). Yet, barite often has hydrothermal or hybrid origins, potentially inheriting less radiogenic Sr isotopic signatures that may not exclusively reflect seawater. In contrast, integrating Sr, O, and C isotopic analyses with REE+Y patterns on the same carbonate samples can effectively resolve this uncertainty. The fracture-filling calcite exhibits a $^{87}Sr/^{86}Sr$ ratio as low as 0.700596 (sample D-2-W), matching values from 3.48 Ga Dresser Formation barites (McCulloch, 1994; Chen et al., 2022) and lower than those of Type-II vesicle carbonates (0.701049–0.701097 at 3.34 Ga; Marien et al., 2023), both interpreted as seawater signals.

These findings collectively suggest that the parent fluid for the fracture-filling calcites was shallow marine water at 3.5 Ga, which infiltrated the basaltic basement along fractures likely caused by tectonic activity, without subsequent hydrothermal alteration or water-rock interaction modification. Therefore, the D-2-W calcite, with the lowest $^{87}Sr/^{86}Sr$ ratio, will serve as the 3.5 Ga seawater endmember in subsequent discussions on seawater-basalt reactions and hydrothermal effects on carbonate geochemistry. Its key geochemical features are: high Sr concentration (1789 μg/g), $\delta^{13}C_{VPDB}$ (+2.20‰), $\delta^{18}O_{VPDB}$ (-13.03‰), initial $^{87}Sr/^{86}Sr$ ratio (0.700596), low REE+Y concentration (2.24 μg/g), and a PAAS-normalized REE+Y pattern showing HREE enrichment (Pr_{SN}/Yb_{SN} 0.04 and Sm_{SN}/Yb_{SN} 0.11), no Ce (1.07) or Eu (1.05) anomalies, but positive La (2.24) and Y (21.64) anomalies with a near-chondritic Y/Ho ratio (36.57).

5.2.2 Low-Temperature Hydrothermal Signatures from Seafloor Alteration

Textural evidence (interpillow and vesicle- fillings), geochemical signatures (REE, C-O-Sr isotopes matching seawater), and syn-eruptive ages (Sm-Nd isochrons) suggest most Archean interstitial carbonates precipitated from basalt-seawater interaction (Nakamura and Kato, 2002, 2004; Yamamoto et al., 2004; Shibuya et al., 2012; Marien et al., 2023; Xiang et al., 2024). Their abiotic precipitation is implied by the lack of organic influence (Xiang et al., 2024), supported by experiments and simulations (22–350 °C; Gudbrandsson et al., 2011; Stockmann et al., 2011; Gysi and Stefánsson, 2012; Galeczka et

al., 2014; McGrail et al., 2017; Menefee et al., 2018; Xiong et al., 2018; Voigt et al., 2018; Lahir et al., 2025; Luo et al., 2025), showing carbonate formation triggered by alkalinity, salinity, and temperature fluctuations during the reaction (Degens et al., 1984; Kempe, 1990; Reitner et al., 1995; Flügel and Munnecke, 2010). In modern settings, such carbonates are abundant in older crusts, forming from low- to moderate-temperature hydrothermal fluids during late-stage seafloor alteration (Bach et al., 2001, 2003, 2011; Gillis et al., 2001; Heft et al., 2008; Coogan and Gillis, 2013). CO_2-rich seawater, heated by intrusions, circulates within oceanic crust, reacts with rocks at up to several hundred °C, enriching fluids with cations like Ca, Fe, Mn, and Mg, which later precipitate as carbonates during cooling (Brauhart et al., 2000; Doyle and Allen, 2003; Nakamura and Kato, 2004; Yamamoto et al., 2004; Shibuya et al., 2012; Xiang et al., 2024). Thus, interstitial carbonates stand as pivotal indicators for basalt-seawater interaction, given their direct derivation from this process.

The REE+Y patterns in interstitial carbonates offer crucial insights: consistent fluid-carbonate partition coefficients confirm that carbonate REE concentrations reflect those of the fluids (Toyama and Terakado, 2019; Nishino et al., 2022), while pattern shapes and anomalies reveal hydrothermal processes and conditions (Debruyne et al., 2016). In modern oceans, hydrothermal vent fluids typically show uniform LREE depletion and pronounced positive Eu anomalies normalized to LREE-rich PAAS (Bau and Dulski, 1999; Hongo and Nozaki, 2001), but LREE enrichment and weaker positive Eu anomalies when normalized to a LREE-depleted PM composition (Fig. 8d; Debruyne et al., 2016). For example, despite PAAS-normalized similarities of carbonates within basaltic degassing spaces, dolomite inclusions show pronounced PM- normalized MREE enrichment and strong positive Eu anomalies, reflecting non-equilibrium interactions between basalt and seawater (Yamamoto et al., 2004), whereas Type-II calcite displays HREE enrichment, negative Eu, and positive Y anomalies, suggesting direct seawater precipitation with minimal fluid-rock interaction (Marien et al., 2023). Thus, selecting an appropriate reference framework and accurately interpreting REE+Y data are essential. Generally, PAAS is in favor as a reference for the seawater and PM for hydrothermal precipitates (Debruyne et al., 2016).

Despite similar geochemical traits, REEs with smaller ionic radii fractionate during hydrothermal processes due to higher element mobility, selective leaching from source rocks (e.g., carbonatites, basalts), and ligand complexation (e.g., Cl^-, F^-, CO_3^{2-}, SO_4^{2-}) during transport (Bau, 1991; Debruyne et al., 2016; Zhao et al., 2021, 2022). For instance, high-temperature fluids leach REE+Y from oceanic crust, particularly plagioclase, yielding LREE-enriched patterns and positive Eu anomalies due to Eu^{3+} reduction to Eu^{2+} (Michard and Albarede, 1986; Klinkhammer et al., 1994; Douville et al., 1999; Bao et al., 2008; Yoshida et al., 2024). Low-temperature fluids and seawater mixing rapidly scavenge REE+Y via Fe-Mn oxyhydroxides, preferentially removing LREE and Eu, flattening patterns and reducing Eu anomalies with distance from vents (Owen and Olivarez, 1988; Ruhlin and Owen, 1986; Barrett and Jarvis, 1988; Olivarez and Owen, 1989, 1991; Zhao et al., 2022).

The pattern shape and lack of Eu anomaly in primary interstitial calcite (Fig. 8), the initial carbonate phase formed during water-rock reactions (Xiang et al., 2024), suggest a low-temperature hydrothermal fluid origin. This calcite exhibits elevated REE+Y concentrations, a near-chondritic Y/Ho ratio, and a PAAS-normalized REE+Y pattern marked by HREE enrichment, no Ce anomaly, and positive La, Gd, Eu, and Y anomalies. Notably, when normalized to PM, minimal REE fractionation and a slightly

positive Y anomaly are observed (Fig. 8), reinforcing the low-temperature hydrothermal fluid interpretation. This Y-enriched flat REE pattern suggests this fluid originated from seawater circulating through basaltic basement of presumed mantle origin, with its REE+Y abundances modified during water-rock reactions.

Parent hydrothermal fluid temperatures can be estimated using stable oxygen isotopes. Marine carbonate $\delta^{18}O$ values reflect both the isotopic composition of precipitating fluids and temperature-dependent fractionation during formation and potential recrystallization. For undiagenetized primary interstitial calcite, formation temperatures can be inferred from its $\delta^{18}O$ value if the parent fluid's $\delta^{18}O$ is known, using the paleotemperature equation (Shackleton and Kennett, 1975):

$$T\,(^{\circ}C) = 16.9 - 4.38(\,\delta^{18}O_{CaCO3} - \delta^{18}O_{w}) + 0.1\,(\,\delta^{18}O_{CaCO3} - \delta^{18}O_{w})^{2} \qquad \text{(Eq.1)}$$

Here, $\delta^{18}O_{CaCO3}$ is referenced to PDB, and $\delta^{18}O_{w}$ to VSMOW. Since the low-temperature hydrothermal fluids derived from seawater and its unknown $\delta^{18}O$ value, here take seawater $\delta^{18}O$ value in the calculation. Given ongoing debate over Paleoarchean seawater $\delta^{18}O$, a range of scenarios spanning −13.3‰ (Jaffrés et al., 2007), −8‰ (Kutyrev et al., 2024), −5‰ (Herwartz et al., 2021), −1.2‰ (Shackleton and Kennett, 1975), 0‰ (Hoefs, 2018), and +3.3‰ (Johnson and Wing, 2020) were evaluated (Table 3). As seawater $\delta^{18}O$ increases from −13.3‰ to +3.3‰, calculated seawater temperatures rise from 15.7 °C to 115.1 °C, while hydrothermal fluid temperatures range from 33.0 ± 2.8 °C to 144.5 ± 4.6 °C, consistent with low-temperature hydrothermal circulation. The low-temperature seafloor alteration (<200 °C) was also evidenced by fluid inclusion studies in ca. 2.22 Ga basaltic andesites from the Kaapvaal Craton, driven solely by volcanic pile cooling (Gutzmer et al., 2003). Such fluid temperatures are plausible through heat loss during oceanic crust cooling in modern off-axis settings (Wheat et al., 2017; Coogan and Gillis, 2018).

Table 3: Temperatures calculated with the $\delta^{18}O_{PDB}$ values (‰) of the seawater endmember (D-2-W) and primary interstitial calcites, and various seawater $\delta^{18}O_{SMOW}$ values (‰).

The collective evidence supports a low-temperature hydrothermal origin for the primary interstitial calcite, offering insights into seafloor alteration processes. Its geochemical characteristics are as follows: $\delta^{13}C_{VPDB}$ (0.63 ± 0.12 ‰), $\delta^{18}O_{VPDB}$ (-16.70 ± 0.56 ‰), an initial $^{87}Sr/^{86}Sr$ ratio of 0.703094 ± 0.000979, low REE+Y concentrations (23.32 to 142.95 μg/g), and a PAAS-normalized REE+Y pattern displaying HREE enrichment (Pr_{SN}/Yb_{SN} 0.07 to 0.16 and Sm_{SN}/Yb_{SN} 0.17 to 0.48), no Ce (1.04 ± 0.03), but positive La (2.10 ± 0.39), Eu (1.69 ± 0.20) and Y (1.57 ± 0.98) anomalies alongside a near-chondritic Y/Ho ratio (32.86 ± 2.94). Elemental analysis reveals elevated Mg, Fe, Mn, Al, Sc, Ti, V, Rb, Mo, and U concentrations, contrasted by much lower Sr levels compared to the seawater endmember

5.3 Post-Depositional Modification of Geochemical Tracers

Geochemical proxies, such as high spatial sampling resolution Mg/Ca, $\delta^{18}O$, $\delta^{13}C$, and $^{87}Sr/^{86}Sr$ measurements facilitate climate reconstruction, constrain weathering and hydrothermal fluxes, and track seawater evolution (Hess et al., 1986; Capo and DePaolo, 1990; Veizer et al., 1999; Zachos et al., 2001;

McArthur et al., 2001; Fantle et al., 2020). However, some proxy records from ancient carbonates may reflect diagenetic rather than primary signals, and thus should be validated through petrographic observations or multiple isotopic and trace elemental proxies to detect diagenetic processes (Banner and Hanson, 1990; Swart, 2015; Fantle et al., 2020). Chemical disequilibrium is crucial for triggering carbonate geochemical alteration; without it, minimal to no alteration occurs, despite obvious textural or physical alteration signs (Fantle et al., 2020). Disequilibrium may arise from fluid chemistry differing from the formational environment, and/or variations in fractionation factors or partition coefficients between formational and diagenetic settings, which may depend on system thermodynamics, e.g., temperature, kinetics, or metastable solids (Fantle et al., 2020). Consequently, shifts in diagnostic features of secondary carbonates can offer insights into water-rock reactions during diagenesis.

Petrographic analysis identifies two alteration processes in primary interstitial calcite (Xiang et al., 2024): recrystallization (forming altered interstitial calcite) and ankeritization (producing interstitial ankerite). Key diagnostic features, including Sr-Mn-Fe concentrations, REE+Y abundance, Y/Ho ratio, Eu anomaly, $^{87}Sr/^{86}Sr$, and $\delta^{13}C$ values, were selected and visualized in radar plots to depict potential geochemical variations across carbonate facies (Fig. 9). In these radar plots, the minimum data values mark the lower axis boundary, and the maximum values define the upper limit. The percentages for each carbonate facies are then computed to emphasize the observed deviations.

Figure 9: Radar plots integrate diagnostic geochemical features across carbonate facies, including Sr-Mn-Fe concentrations, REE+Y abundance, Y/Ho ratios, Eu anomalies, $^{87}Sr/^{86}Sr$, and $\delta^{13}C$ values. Data ranges (min-max) define axis boundaries, with percentages calculated per facies to highlight compositional deviations. (a) Radar plots for fracture-filling calcite, primary/altered interstitial calcite, and interstitial ankerite reveal fluid-driven geochemical signatures. (b) Comparative radar plots of sedimentary carbonates and stromatolites enable rapid diagnosis of depositional environments and diagenetic histories through patterned geochemical deviations and similarities.

5.3.1 Trace Element Redistribution during Recrystallization

Carbonate recrystallization entails changes in crystal size, shape, and lattice orientation without altering mineralogy (Flügel and Munnecke, 2010; Fantle et al., 2020). This process impacts carbonate geochemistry, affecting Sr concentration, $^{87}Sr/^{86}Sr$ ratio, $\delta^{18}O$, and Mg/Ca ratio (Baker et al., 1982; Killingley, 1983; Kastner et al., 1986; Richter and DePaolo, 1988; Schrag et al., 1995; Fantle and DePaolo, 2006; Swart, 2015). The geochemical composition of recrystallized calcite hinges on that of parent calcite and the altering fluid. For example, Kastner et al. (1986) found increased Sr and Mg in recrystallized carbonate, likely due to advective fluid flow through mid-ocean ridge flank sediments involving low-temperature alteration of volcanic glass. Additionally, meteoric water, with its low salinity, high oxygen, and low $\delta^{18}O$ and $\delta^{13}C$ values, yields chemically and isotopically unique diagenetic products (Brand and Veizer, 1980, 1981; Allan and Matthews, 1982; Lohmann, 1988).

Compared to primary interstitial calcite, altered interstitial calcite exhibits elevated REE+Y abundance, Y/Ho, and $^{87}Sr/^{86}Sr$ ratios, alongside lower Fe and $\delta^{13}C$, while maintaining consistent Sr, Mn, and Eu/Eu* (Fig. 9a). Its radar plot shape closely resembles that of primary interstitial calcite, suggesting that the

fluid responsible for dissolution-recrystallization shares the same origin, i.e., a low-temperature hydrothermal fluid derived from seawater-basalt interaction. This fluid likely forms through prolonged fluid-rock interaction. Evidence lies in the covariations of $\delta^{13}C$ with $\delta^{18}O$ and of $^{87}Sr/^{86}Sr$ ratios with Eu/Eu*.

In recrystallized calcite, $\delta^{13}C$ and $\delta^{18}O$ values are mainly controlled by the isotopic composition of reactive fluids and the system's openness to fluid exchange (Swart, 2015; He et al., 2024). Temperature, pH, and precipitation kinetics also impact fractionation (O'Neil and Epstein, 1966; Zeebe and Wolf-Gladrow, 2001; McConnaughey, 2003), but are often restricted by fluid composition and system openness. Open systems enable continuous fluid flow for sustained exchange, making isotopes align with fluid-dominated values (e.g., meteoric water influx reduces $\delta^{18}O$); closed systems, with limited fluid access, retain original isotopic features (Swart, 2015).

Compared with primary interstitial and fracture-filling calcites, the altered interstitial calcite shows a negative co-variation of $\delta^{13}C$ and $\delta^{18}O$ (Fig. 10a). Biological processes can result in carbonate $\delta^{13}C$ and $\delta^{18}O$ deviating from physicochemical equilibrium values (known as "vital effects"; Lee and Carpenter, 2001; Swart, 2015), usually yielding lower $\delta^{13}C$ and $\delta^{18}O$ values. Yet, these vital effects can be excluded since interstitial carbonate is an abiotic product of water-rock reactions in the oceanic crust without organic matter (Nakamura and Kato, 2004; Yamamoto et al., 2004; Shibuya et al., 2012; Marien et al., 2023; Xiang et al., 2024). The observed trend may stem from either the mixing of Archean seawater with hydrothermal fluids interacting with mantle-derived rocks or carbonate precipitation under non-equilibrium conditions causing isotope fractionation (Marien et al., 2023). Xiang et al. (2024) supported this by showing that vein calcites in basalt, in a relatively closed system and more affected by basalt alteration, have lower $\delta^{13}C$ and $\delta^{18}O$ values than interstitial calcite. Thus, the $\delta^{13}C$-$\delta^{18}O$ covariation in the altered interstitial calcite suggests it may have taken in more basalt-derived signals.

Figure 10: The cross-plots of (a) $\delta^{13}C$ vs $\delta^{18}O$, and (b) the age-corrected $^{87}Sr/^{86}Sr$ ratios vs the PAAS-normalized Eu/ Eu* ratios of the EPT carbonates. The co-variations reflect progressive seawater-basalt reaction (indicated by black arrows). The grey line indicates the regression line based on data of fracture-filling calcite D-2-W, the primary interstitial calcite and interstitial ankerite, and the grey envelope is plotted with the confidence interval of 95%, generated via Seaborn regplot (default). To be noted, some altered interstitial calcite and SPF stromatolite are located in the area. Data sources: (a) Modern seawater data from Kroopnick (1980) and Tan (1988); Carbonatized Apex basalt data from Nakamura and Kato (2004); Mantle flux data from Degens et al. (1984) and Hayes and Waldbauer (2006); (b) Type-I and Type-II Euro interstitial calcite data from Marien et al. (2023). (Abbreviations: P-primary; A-altered; Cal. –calcite; Carb. -carbonate).

The second piece of evidence is the strong positive correlation (Pearson's r = +0.96) between Eu anomalies and $^{87}Sr/^{86}Sr$ ratios in fracture-filling calcite, primary interstitial calcite, and ankerite (Fig. 10b). The interstitial ankerite likely precipitated from high-temperature hydrothermal fluids, formed as seawater circulated into the deep oceanic crust, heated, and reacted with basaltic wall rock (detailed in Section 5.3.2). This positive covariation suggests increasing hydrothermal alteration of basaltic rocks

with temperature. It is important to note that part of the altered interstitial calcites, along with Euro Type-I and Type-II carbonates (as classified by Marien et al., 2023), cluster within the 95% confidence interval of the regression line. This clustering suggests a shared cause for the elevated Eu anomalies and $^{87}Sr/^{86}Sr$ ratios observed. Furthermore, a comparable correlation was observed in Late Ediacaran rhodochrosite, implying that radiogenic Sr was contributed by deep-sourced hydrothermal fluids that extracted radiogenic Sr from underlying sediments (Gao et al., 2021). The similar geochemical behavior of Eu and Sr during hydrothermal alteration is due to the comparable radii of Eu^{2+} and Sr^{2+} (McCarthy, 1971; Shannon, 1976), possibly leading to analogous geochemical responses. As the temperature rises during hydrothermal transformation, water-rock reactions continue to occur, leading to synchronous changes in the contents of Eu and Sr elements in the fluid. However, the similarity in Sr concentrations, $^{87}Sr/^{86}Sr$ ratios, and Eu/Eu* values between altered interstitial calcite and primary facies implies limited Sr and Eu redistribution during the process. This, in turn, suggests that even minor water-rock reactions can readily trigger calcite recrystallization.

5.3.2 Elemental Reset Mechanisms in Ankeritization

Ankeritization converts calcite ($CaCO_3$) to ankerite ($Ca(Fe,Mg)(CO_3)_2$) via Fe^{2+}- and Mg^{2+}-rich fluid influx from adjacent rocks during burial or hydrothermal activity (Boles, 1978; Hendry et al., 2000). Petrographic studies show interstitial ankerite in schistose basalts, while basalts with less dynamic transform contain interstitial calcite (Xiang, 2023; Xiang et al., 2024). The Fe and Mg in fluids that drive ankeritization mainly derives from chlorite breakdown. In metamorphism, Fe and Mg in basalt are retained by secondary chlorite, which has a high affinity for these elements (Cathelineau and Nieva, 1985), thereby reducing Fe incorporation into calcite by trapping much of the dissolved Fe^{2+} and Mg. Nevertheless, as water-rock interactions continue, chlorite migrates into interstitial fluids and decomposes, releasing Mg and Fe that prompt the dissolution of interstitial calcite and the formation of interstitial ankerite. The validity of this origin is reinforced by the pronounced positive correlation between Eu anomalies and $^{87}Sr/^{86}Sr$ ratios (Fig. 10b), as shown in Section 5.3.1.

However, despite the similarity in $\delta^{13}C$ and $\delta^{18}O$ values between interstitial ankerite and calcite，their isotopic covariance is weaker than the correlation observed between Eu anomalies and $^{87}Sr/^{86}Sr$ ratios (Fig.10). This discrepancy likely stems from mineralogical controls. No research on ankerite exists, but dolomite studies may offer insights. Dolomite typically has higher $\delta^{13}C$ and $\delta^{18}O$ compared to calcite when both minerals form or coexist under equilibrium conditions (Sheppard and Schwarcz, 1970). For instance, at 20–25°C, dolomite is enriched in ^{18}O by ~4.9–6.8‰ and in ^{13}C by ~2.4‰ relative to calcite, though these differences diminish with rising temperature (Degens and Epstein, 1964; O'Neil and Epstein, 1966; Sheppard and Schwarcz, 1970; Matthews and Katz, 1977). Carbon isotope fractionation is less temperature-sensitive than oxygen isotope fractionation (Rubinson and Clayton, 1969; Romanek et al., 1992), with $\delta^{13}C$ differences being smaller, more variable, and influenced by local carbon sources (Tan and Hudson, 1971; Mozley and Burns, 1993). Consequently, $\delta^{13}C$ was prioritized over $\delta^{18}O$ as a diagnostic indicator in this study (Fig. 9).

Ankeritization tends to occur at relatively high temperatures. Experiments indicate that under hydrothermal and metamorphic conditions, chlorite subtly dissolves at 100–275 °C (Smith et al., 2013),

decomposes at 300 – 400°C, releasing Fe and Mg into fluids (Saccocia and Seyfried, 1994; Hwang, 1988). Unlike other carbonates, PAAS- and PM-normalized REE+Y patterns in interstitial ankerite show higher REE+Y abundance, remarkably, MREE enrichment and strong positive Eu anomalies (Figs. 6, 8). REEs prefer calcite to dolomite, with K_D (dolomite/calcite) fairly stable (0.17-0.23), while both show a gradual LREE-to-HREE decrease (Dawson and Hinton, 2003). Hence, MREE enrichment originates from parent fluids, not mineralogy. Roberts et al. (2009) attributed similar MREE enrichment in dolomitic schist samples (~880– 550 Ma) to their precipitiation from hot (~250°C), saline brines interacting with schist basement. This unique REE+Y pattern and the high Eu Eu/Eu* ratios (2.99 ± 1.00) of interstitial ankerite suggests its precipitation from high-temperature hydrothermal fluids (>250°C) rather than low-temperature systems.

Typically, high-temperature hydrothermal fluids usually originate from the interplay of deep heat sources (magmatic or tectonic), water–rock reactions at depth, and fluid circulation through faults or fractures, often exceeding 350-400°C (Witt, 1988; Charlou et al., 2002; Koschinsky et al., 2008; McDermott et al., 2018; Tao et al., 2020; Witt et al., 2024). A study on hydrothermal pipes in 3.47 – 3.43 Ga volcanic rocks from the Barberton Greenstone Belt showed initial fluid-temperatures of 200–270°C due to seawater-basalt reactions or deep granitic intrusions before mixing with cold seawater (de Wit and Furnes, 2016). In North Pole Dome, multiple faulting, intrusion, and eruption events created numerous hydrothermal channels and diverse basalt alteration facies (Hickman and Van Kranendonk, 2004; Gifkins et al., 2005; Van Kranendonk, 2006; Caruso et al., 2021; Brenner et al., 2024). In Mt Ada Basalt (with interstitial ankerite), five hydrothermal episodes were recorded, with heat sources including nearby granite intrusion, fluid flow along high-permeability bedding planes, and prolonged alteration with repeated new basalt flow eruptions (Brenner et al., 2024). Notably, the marked positive link between Eu anomalies and $^{87}Sr/^{86}Sr$ ratios strongly backs the idea that high-temperature fluids, heated by prolonged seawater reactions with deep or newly-erupted basalt flows and circulating via faults/fractures, likely triggered ankeritization.

5.3.3 Validation in Sedimentary Carbonates and Stromatolitic Facies

Based on the discussion above, it is possible to determine the depositional environments and diagenetic evolution of sedimentary carbonates and SPF stromatolites, by comparing the similarities and differences in their radar plots with those of interstitial carbonates. For instance, sedimentary carbonates have been discerned to originate from either marine or terrestrial environments, based on sedimentological, petrological analyses, and their $\delta^{13}C$ signatures (Xiang et al., 2024), with each facies exhibiting distinct radar plot configurations.

Sedimentary carbonates exhibit certain hydrothermal geochemical signatures. Those in marine settings are identified as ankerite (Fig. 3a), and their radar-plot shape closely resembles that of interstitial ankerite (Fig. 9b). Despite showing higher Fe-Mn concentrations and lower Eu/Eu*-$^{87}Sr/^{86}Sr$ ratios, this similarity in radar shape strongly points to the influence of high-temperature hydrothermal fluids. In contrast, the one sample (DB) that likely originated in a terrestrial hydrothermal pond is low-Mn calcite (Fig. 3a) and shows a distinct radar shape with low Fe-Mn-Sr, the lowest mantle-like $\delta^{13}C$ value, as well as the high Eu/Eu*-$^{87}Sr/^{86}Sr$ ratios (Fig. 9b). Positive Eu anomalies in sedimentary carbonates are commonly linked

to remnants of high-temperature hydrothermal fluid activity (Michard et al., 1983; Kamber and Webb, 2001; Van Kranendonk et al., 2003; Bau and Alexander, 2009; Bau et al., 2010; Johannessen et al., 2017). Notably, three marine samples and sample DB deviate from the regression line, with $^{87}Sr/^{86}Sr$ ratios rising faster than Eu/Eu* ratios (Fig.10b). This has been used to argue for Sr originating from terrestrial sources (Wei et al., 2019; Gao et al., 2021). However, Marien et al. (2023) proposed that the highly radiogenic $^{87}Sr/^{86}Sr$ in high-Mn carbonates results from contamination by co-existing Rb-rich quartz with highly radiogenic Sr. Since these samples were deposited in shallow marine slopes/lagoons or terrestrial hydrothermal ponds and all link to co-existing quartz or chert layers (Xiang et al., 2024), both explanations are somewhat plausible, warranting further research to clarify their contributions.

Stromatolites exhibit shallow marine signatures, supported by radar-plot data showing high $\delta^{13}C$ values and Y/Ho ratios, alongside low Fe and REE+Y concentrations, aligning with prior studies (Van Kranendonk et al., 2003; Lindsay et al., 2005; Allwood et al., 2010; Flannery et al., 2018; Viehmann et al., 2020; Xiang et al., 2024). It is noteworthy that the SPF Stromatolite experienced subsequent alteration, evidenced by laminae recrystallization and euhedral dolomite overgrowth on laminae margins (Allwood et al., 2009; Xiang et al., 2024). This alteration may have been slightly influenced by high-temperature hydrothermal fluids, as indicated by two pieces of evidence: (1) the stromatolite's REE+Y pattern shows MREE enrichment relative to seawater, especially in its highly silicified counterpart (Fig. 8b); (2) SPF Stromatolite data points align within the Eu/Eu*-$^{87}Sr/^{86}Sr$ regression line, close to interstitial ankerite (Fig. 10b). Allwood et al. (2006b) reported maximum temperatures of 200-500 °C during its history, but the timing remains unclear.

The upper Strelley Pool Formation, preserving SPF stromatolites, is intersected by colloform-crustiform black and white chert veins that don not extend into the overlying Euro Basalt (Van Kranendonk and Pirajno, 2004; Sugitani et al., 2015; Zepeda et al., 2023). Brenner et al. (2024) suggested this upper part likely marks the epithermal capping horizon of a hydrothermal system, with activities around ~3.35 Ga. Van Kranendonk and Pirajno (2004) inferred that hydrothermal circulation was possibly driven by heat from the Euro Basalt and influenced by older continental crust. For more precise dating, isotopic studies are crucial. The Sm-Nd isotopic ages of SPF stromatolites (3.25 ± 0.32 Ga) match the deposition age of the Strelley Pool Formation's deposition age within error but also overlap with a thermal event linked to the 3.2 Sulfur Springs Group eruption or a younger event at 2.72 ± 0.22 Ga (Viehmann et al., 2020).

In summary, radar plot comparisons offer a rapid, effective tool for distinguishing depositional settings and diagenetic pathways in carbonates and stromatolites. However, pinpointing specific geological processes requires integrating this method with sedimentological, petrographic, and lithofacies data to ensure robust interpretations.

5.4 Implications for Early Seawater Strontium Isotope Evolution

The radiogenic Sr isotopic composition of seawater is primarily shaped by the interplay between radiogenic riverine inputs from continental weathering and less radiogenic mantle inputs via mid-ocean

ridges, preserved in well-preserved marine carbonates (Veizer, 1989). However, this continental weathering-dominated Sr cycling model may not apply to Earth's early history.

Unlike the modern ocean, where continental river discharge is a controlling factor, the Archean ocean was dominated by large-scale hydrothermal interactions between seawater and ocean floor basalts (Veizer et al., 1982). Thus, marine Sr isotopic composition was expected to be less radiogenic, close to Bulk Silicate Earth (BSE). Elevated $^{87}Sr/^{86}Sr$ ratios have traditionally been attributed to continental weathering (Satkoski et al., 2016, 2017; Ravindran et al., 2020; Roerdink et al., 2022; Marien et al., 2023), based on the assumption that continental materials, with higher Rb/Sr ratios, produce higher $^{87}Sr/^{86}Sr$ ratios through ^{87}Rb decay. While valid in this study, continental weathering was not the sole driver of elevated $^{87}Sr/^{86}Sr$ ratios in early Archean marine authigenic minerals.

This study presents age-corrected $^{87}Sr/^{86}Sr$ ratios of EPT carbonates from various facies (Fig. 11), alongside data from carbonates and barites (McCulloch, 1994; Shields and Veizer, 2002; Satkoski et al., 2016; Ravindran et al., 2020; Roerdink et al., 2022; Chen et al., 2022; Marien et al., 2023) and Sr isotopic evolution lines for seawater, BSE, Depleted Mantle (DM), and Upper Continental Crust (UCC; details in Appendix A). Age-corrected $^{87}Sr/^{86}Sr$ ratios of fracture-filling calcites overlap with Dresser barite data, falling between BSE and UCC evolution lines, reflecting the less radiogenic seawater composition at ~3.5 Ga. However, some carbonates show higher $^{87}Sr/^{86}Sr$ ratios, even above the UCC line, likely elevated by hydrothermal alteration of oceanic basaltic crust. This is supported by a strong positive correlation between Eu anomalies and $^{87}Sr/^{86}Sr$ ratios in interstitial carbonates (Fig. 10b; discussed in Section 5.3). Thus, hydrothermal fluids are not always less radiogenic than contemporary seawater; they can be more radiogenic if derived from interactions between seawater and oceanic basaltic crust or felsic basement with higher $^{87}Sr/^{86}Sr$ ratios. Consequently, elevated age-corrected $^{87}Sr/^{86}Sr$ ratios alone cannot serve as definitive evidence for continental weathering emergence without accounting for hydrothermal input during deposition.

Figure 11: (a) The temporal variations in Sr isotopic compositions of EPT carbonates, alongside reference data from carbonates and barites, plotted against the Sr isotopic evolution curves of Bulk Silicate Earth (BSE), Depleted Mantle (DM), and Upper Continental Crust (UCC). The region marked by the dashed black rectangle is expanded in (b). The blue line represents the inferred seawater Sr isotopic evolution, based on the least radiogenic values observed at any given time. (b) The Sr isotopic compositions of fracture-filling calcites and barites from the Dresser Formation, sharing the same labels as (a). Details of the evolution lines are provided in the Appendix A, with carbonate and barite references sourced from McCulloch (1994), Shields and Veizer (2002), Satkoski et al. (2016), Ravindran et al. (2020), Roerdink et al. (2021), Chen et al. (2022) and Marien et al. (2023). (Abbreviations: P-primary; A-altered; Carb. –carbonate; SPF- Strelley Pool Formation).

5.5 Controls on Ocean Chemistry in the Paleoarchean Eon

Modern marine geochemistry is determined by main material fluxes to ocean including river run-off (deliver materials to the surface ocean at the land-sea boundaries), atmospheric deposition (to all regions

of the surface ocean), hydrothermal activity (to deep and intermediate waters above seafloor) and subsequent fate of the material by various sinks (Chester, 2009). In the Paleoarchean, continental weathering and hydrothermal activity were the primary drivers of ocean chemistry, influencing nutrient availability, redox conditions, and the evolution of the early biosphere.

Larger impacts of continental weathering flux on ocean chemistry at 3.26 Ga than previously suggested were proposed by Satkoski et al. (2016) with evidence of more radiogenic $^{87}Sr/^{86}Sr$ ratios in barite than contemporaneous mantle. This was predated at approximately 3.7 ± 0.15 Ga by Roerdink et al. (2022) with the same method using stratiform barite from three 3.52 -3.20 Ga cratons (i.e., Kaapvaal, Pilbara and Dharwar). Despite debates over the validity of using barite or carbonate $^{87}Sr/^{86}Sr$ ratios for this purpose, the Archean continents existed, yet were mostly submerged (Arndt, 1999; Kitajima et al., 2001; Kump and Barley, 2007), with less than ~4% of Earth's surface exposed (Kump and Barley, 2007; Flament et al., 2013). Evidence of the EPT's subaerial exposure periods includes erosional unconformities, locally preserved desiccation cracks, widespread rippled sedimentary carbonate rocks and stromatolites, and alluvial paleosols (Lambert et al., 1978; Walter et al., 1980; Groves et al., 1981; Buick and Dunlop, 1990; Van Kranendonk, 2006; Djokic et al., 2017; Retallack, 2018; Van Kranendonk et al., 2019). Djokic et al. (2017, 2021) reported geyserite and siliceous sinter in the Dresser formation, interpreting them as a fluvial, subaerial hot spring, supported by abrupt lateral facies changes, associated channelized clastic deposits, and distinct geochemical data. The subaerial area is also corroborated by sedimentary carbonate rock DB, whose average mantle-like $\delta^{13}C$ value of -5.8 ‰ and sedimentological textures suggest a restricted hydrothermal pond rarely affected by seawater (Xiang et al., 2024). Thus, terrigenous inputs from subaerial weathering have likely influenced ocean geochemistry on a regional-scale. Notably, subaerial weathering would have delivered key nutrients, especially phosphorus, to the oceans, supporting early microbial life and potentially influencing the evolution of the biosphere (Jones et al., 2015; Hao et al., 2020; Roerdink et al., 2022).

In comparison, in the early Archean, hydrothermal flux via a large-scale interaction between seawater and seafloor basalts was likely a major control on ocean geochemistry (Veizer et al., 1982). There was extensive hydrothermal activity, as evidenced by the widespread presence of sediments such as cherts, BIFs, and carbonates in three greenstone belts, whose origins were explained by the chemical reactions between hydrothermal fluids and seawater (Dymek and Klein, 1988; Veizer et al., 1989; Bau and Dulski, 1996; Van Kranendonk et al. 2003; Van den Boorn et al., 2007; Allwood et al., 2010; Shibuya et al., 2010; Ledevin et al., 2014; Westall et al., 2015; Duda et al., 2018; Nutman et al, 2019a; Hickman-Lewis et al., 2020; Viehmann et al., 2020; Rouillard et al., 2021; Marien et al., 2023; Xiang et al., 2024). Widespread hydrothermal activity has imprinted distinct REE+Y abundance patterns on marine authigenic sediments, featuring smooth HREE enrichment, negative Ce anomalies, positive La and Y anomalies, and notably, a pronounced positive Eu anomaly (Van Kranendonk et al. 2003; Allwood et al., 2010; Nutman et al, 2019a, b; Hickman-Lewis et al., 2020; Viehmann et al., 2020; Marien et al., 2023; herein). Beyond being a primary REE+Y source, hydrothermal fluids also transported significant quantities of Ca, Mg, Fe, Mn, Si, and various trace elements. These elements precipitated as carbonates within pillow basalts, reacting with CO_2 in the fluids and serving as a major carbon sink on early Earth (up to 90%; Nakamura and Kato, 2004; Yamamoto et al., 2004; Marien et al., 2023; Xiang et al., 2024).

Additionally, some elements were released into the anoxic Archean ocean, providing essential metal nutrients for early life (Catling and Zahnle, 2020; Lepot, 2020).

Microbial activity shaped early Archean ocean geochemistry, with microbes driving C, S, and Fe biogeochemical cycles via metabolism (Zhelezinskaia et al., 2014; Lepot, 2020; Johnson et al., 2022; Mateos et al., 2023). Regarding carbon isotopes, anoxygenic photoautotrophs in the photic layer prefer ^{12}C, enriching ^{13}C in shallow marine carbonates (e.g., sedimentary, stromatolites) with positive $\delta^{13}C$ values (Lindsay et al., 2005; Arp et al., 2011; Flannery et al., 2018; Xiang et al., 2024). Methanotrophs, in contrast, oxidize ^{13}C-depleted methane, producing organic matter/DIC with negative $\delta^{13}C$ values incorporated into carbonates (Schopf et al., 2017; Lepot, 2020). Microorganisms also affect seawater REE+Y patterns: their particulate organic carbon adsorbs LREEs (Cantrell and Byrne, 1987; Hathorne et al., 2015; Smrzka et al., 2019) and scavenges Ho faster than Y (Nozaki et al., 1997; Zhang et al., 1994; Qu et al., 2009), causing LREE depletion and super-chondritic Y/Ho ratios in shallow seawater and carbonates.

Consequently, a dual-regime ocean emerged, shaped by the interplay of continental weathering, hydrothermal venting, and microbial activity. Hydrothermal venting mainly governed deep-ocean chemistry, whereas continental weathering and microbial activity predominantly influenced shallower ocean areas. Given that carbonates only capture the geochemical conditions of adjacent fluids, they offer at most a regional view of the water column. Hence, caution is crucial when extending the geochemical traits of some samples to a global scale. Moreover, to gain a comprehensive understanding of the geochemical cycles and compositional evolution of seawater, especially concerning Sr isotopic composition, further studies on ancient carbonates from diverse facies and depositional settings are highly encouraged.

6. Conclusion

Paleoarchean rocks (3.5 to 3.3 Ga) of the East Pilbara Terrane (EPT), Western Australia, contain carbonates in a variety of facies, including interstitial carbonate between pillow basalts, fracture-filling calcite, sedimentary carbonates and carbonate associated with stromatolites. High spatial resolution analysis of geochemical features encoded in these carbonates (major and trace elements, the REE+Y patterns, stable C, O and radiogenic Sr isotopes, emphasizes the significance of EPT carbonates as valuable archives for reconstructing early Earth environments on Early Earth. More specifically, our investigations yielded the following key findings:

(1) The fracture-filling calcite D-2-W from the Middle Basalt Member of Dresser Formation (3.48 Ga) serves as a proxy for Paleoarchean shallow seawater, featuring high Sr (1789 μg/g), $\delta^{13}C$ (+2.20‰), $\delta^{18}O_{VPDB}$ (-13.03‰), age-corrected $^{87}Sr/^{86}Sr$ (0.700596), low REE+Y, near-chondritic Y/Ho, and PAAS-normalized REE+Y patterns with HREE enrichment, positive La and Y anomalies, and no Ce/Eu anomalies, reflecting a shallow marine setting likely influenced by anoxygenic photosynthetic processes and low-intensity volcanic-hydrothermal interactions.

(2) EPT interstitial carbonates reliably reflect hydrothermally driven by basalt-seawater interactions in the Paleoarchean seafloor. With rising temperatures during hydrothermal alteration, water-rock reactions occur, enriching carbonates in basalt-derived trace elements (Mg, Fe, Mn, LREE), lowering Sr and $\delta^{13}C$, and synchronously increasing $^{87}Sr/^{86}Sr$ and Eu/Eu*. Thus, the elevated carbonate $^{87}Sr/^{86}Sr$ ratios alone (even more radiogenic $^{87}Sr/^{86}Sr$ than contemporary Bulk Silicate Earth), cannot prove continental weathering emergence without considering hydrothermal influence.

(3) Interstitial carbonates undergo two post-depositional alteration, i.e. recrystallization and ankeritization. Recrystallization, often induced by low-temperature hydrothermal fluids, slightly shifts geochemical compositions toward those of the altering fluid but minimally affects normalized REE+Y patterns and $\delta^{13}C$ values. In contrast, ankeritization, triggered by high-temperature hydrothermal fluids, causes dissolution and neomorphism, resulting in elevated basalt-derived element abundances, altered REE+Y patterns with MREE enrichment and strong positive Eu anomalies, and a higher $^{87}Sr/^{86}Sr$ ratio, while $\delta^{13}C$ remains consistent.

(4) Compared with interstitial carbonates, deviations in eight key diagnostic indicators (Sr-Mn-Fe concentrations, REE+Y abundance, Y/Ho ratio, Eu anomaly, $^{87}Sr/^{86}Sr$, and $\delta^{13}C$ value) enable rapid diagnosis to differentiate depositional settings and diagenetic pathways in sedimentary carbonates and stromatolites.

(5) A dual-regime ocean emerged from continental weathering, hydrothermal venting and microbial activity, with hydrothermal venting controlling deep-ocean chemistry and the latter two influencing shallower areas. As carbonates reflect nearby fluid conditions and offer a regional view, caution is required in globalizing sample features, and more ancient carbonate studies across facies and settings are needed to fully understand seawater's geochemical cycles and evolution.

Acknowledgements

We gratefully acknowledge A. Hackmann and W. Dröse for sample preparation, V. Karius for ICP-OES measurements, as well as D. Hoffmann, N. Messling, B. Dietrich, and E. Schiffczyk for their assistance in measuring rare earth elements and strontium isotopic compositions, T. Di Rocco, D. Kohl, and T. Wasselin for performing stable isotope measurements, all of whom are affiliated with the Geoscience Faculty of the University of Göttingen. We extend our appreciation to W. Bach (University of Bremen) and G. Shields (University College London) for data analysis related to rare earth elements and strontium isotopes. We are indebted to M. van Kranendonk (Curtin University, Perth, Western Australia), as well as F. Myers and G. Myers, for their valuable assistance during fieldwork and for providing rock materials. A. Hickman (Geological Survey of Western Australia) and A. Hofmann (University of Johannesburg, South Africa) thanked for providing information of the Pilbara Craton and the Barberton Greenstone Belt, respectively. The core library of the Geological Survey of Western Australia, is acknowledged for permission to sample drill core materials from the Pilbara region (approval for P954, 1014, 1091). This study was financially supported by the China Council Scholarship (CSC), the German Research Foundation (DFG) priority program (SPP)1833 "Building a Habitable Earth" (RE 665/42-2; DU 1450/3-

995 1; DU 1450/3-2; TH 713/13-2; WI 3579/3-1), the Göttingen Academy of Sciences and Humanities in Lower Saxony, the National Natural Science Foundation of China (42502035), Leshan Normal University Scientific Research Start-up Project for Introducing High-level Talents (RC2024007), as well as DFG grants INST 186/1274-1 FUGG and WI 3579/5-1.

Author contributions

WX, JR and JD designed the framework. WX is responsible for data collection, analysis and interpretation, and drafting the manuscript. JR and JP contributed to the fieldwork and sample collections. AP and MW were involved in methodology and data interpretation. All co-authors have been involved in revising the content of the manuscript, and approved the final manuscript for submission.

Data availability

The data are presented in the manuscript; and can be requested from the corresponding author.

Conflict of interest statement

Authors declare no competing interests.

Appendix A. Supplementary Material

Supplementary material includes methodology on the binary mixing model (Fig. 7), Sr isotopic evolution line (Fig. 11), and related supporting figures (Figs. A.1 and A.2), along with geochemical data for reference samples Cal-s, Jls-1, and JDo-1 (Table A.1). Figure A.1 displays PAAS-normalized REE+Y patterns of the referenced EPT carbonates in Figure 5. Figure A.2 presents histograms showing the concentrations of Al (wt%), Th, Sc, Ti, Zr, Rb, and total REE (μg/g) in EPF basalts, with their mean values (MV) used in the binary mixing model of Figure 7.

Reference

Abd-Elhameed, M., Attia, G., Salama, Y., El-Moghazy, A., & Mahmoud, A., 2025. Microfacies analysis and diagenetic history of Lower to Middle Eocene carbonates at Umm Russies area in the northeastern desert of Egypt. Scientific Reports, 15(1), 20159. https://doi.org/10.1038/s41598-025-05365-7.

Alexander, B. W., Bau, M., Andersson, P., & Dulski, P., 2008. Continentally-derived solutes in shallow Archean seawater: Rare earth element and Nd isotope evidence in iron formation from the 2.9 Ga Pongola Supergroup, South Africa. Geochimica et Cosmochimica Acta, 72(2), 378–394. https://doi.org/10.1016/j.gca.2007.10.028.

Alibo, D. S., & Nozaki, Y., 1999. Rare earth elements in seawater: Particle association, shale-normalization, and Ce oxidation. Geochimica et Cosmochimica Acta, 63(3), 363–372. https://doi.org/10.1016/S0016-7037(98)00279-8.

Allan, J. R., & Matthews, R. K., 1982. Isotope signatures associated with early meteoric diagenesis. Sedimentology, 29(6), 797–817. https://doi.org/10.1111/j.1365-3091.1982.tb00085.x.

Allwood, A. C., Walter, M. R., Kamber, B. S., Marshall, C.P., & Burch, I. W., 2006a. Stromatolite reef from the Early Archaean era of Australia. Nature, 441(7094): 714-718. https://doi.org/10.1038/nature04764.

Allwood, A. C., Walter, M. R., & Marshall, C.P., 2006b. Raman spectroscopy reveals thermal palaeoenvironments of c. 3.5 billion-year-old organic matter. Vibrational Spectroscopy, 41(2): 190-197. https://doi.org/10.1016/j.vibspec.2006.02.006.

Allwood, A. C., Walter, M. R., Burch, I. W., & Kamber, B. S., 2007. 3.43 billion-year-old stromatolite reef from the Pilbara Craton of Western Australia: Ecosystem-scale insights to early life on Earth. Precambrian Research, 158(3–4), 198–227. https://doi.org/10.1016/j.precamres.2007.04.013.

Allwood, A. C., Grotzinger, J. P., Knoll, A. H., Burch, I. W., Anderson, M. S., Coleman, M. L., & Kanik, I., 2009. Controls on development and diversity of Early Archean stromatolites. Proceedings of the National Academy of Sciences, 106(24), 9548–9555. https://doi.org/10.1073/pnas.0903323106.

Allwood, A. C., Kamber, B. S., Walter, M. R., Burch, I. W., & Kanik, I., 2010. Trace elements record depositional history of an Early Archean stromatolitic carbonate platform. Chemical Geology, 270(1–4), 148–163. https://doi.org/10.1016/j.chemgeo.2009.11.013.

Arndt, N., 1999. Why was flood volcanism on submerged continental platforms so common in the Precambrian? Precambrian Research, 97(3), 155–164. https://doi.org/10.1016/S0301-9268(99)00030-3.

Arndt, N., Bruzak, G., Reischmann, T., 2001. The oldest continental and oceanic plateaus: geochemistry of basalts and komatiites of the Pilbara Craton, Australia. In: Ernst, R.E., Buchan, K.L. (Eds.), Mantle Plumes: Their Identification through Time. Geological Society of America, pp. 359-387. Special Paper 352.

Arp, G., Helms, G., Karlinska, K., Schumann, G., Reimer, A., Reitner, J., & Trichet, J., 2011. Photosynthesis versus Exopolymer Degradation in the Formation of Microbialites on the Atoll of Kiritimati, Republic of Kiribati, Central Pacific. Geomicrobiology Journal, 29(1), 29–65. https://doi.org/10.1080/01490451.2010.521436.

Arp, G., Reimer, A., & Reitner, J., 2001. Photosynthesis-Induced Biofilm Calcification and Calcium Concentrations in Phanerozoic Oceans. Science, 292(5522), 1701–1704. https://doi.org/10.1126/science.1057204.

Bach, W., Alt, J. C., Niu, Y., Humphris, S. E., Erzinger, J., & Dick, H. J. B., 2001. The geochemical consequences of late-stage low-grade alteration of lower ocean crust at the SW Indian Ridge: Results from ODP Hole 735B, Leg 176). Geochimica et Cosmochimica Acta, 65(19), 3267–3287. https://doi.org/10.1016/S0016-7037(01)00677-9.

Bach, W., Peucker-Ehrenbrink, B., Hart, S. R., & Blusztajn, J. S., 2003. Geochemistry of hydrothermally altered oceanic crust: DSDP/ODP Hole 504B – Implications for seawater-crust exchange budgets and Sr- and Pb-isotopic evolution of the mantle. Geochemistry, Geophysics, Geosystems, 4(3). https://doi.org/10.1029/2002GC000419.

Bach, W., Rosner, M., Jöns, N., Rausch, S., Robinson, L. F., Paulick, H., & Erzinger, J., 2011. Carbonate veins trace seawater circulation during exhumation and uplift of mantle rock: Results from ODP Leg 209. Earth and Planetary Science Letters, 311(3), 242–252. https://doi.org/10.1016/j.epsl.2011.09.021.

Baker P. A., Gieskes J. M. & Elderfield H., 1982. Diagenesis of carbonates in deep-sea sediments – evidence from Sr/Ca ratios and interstitial dissolved Sr2+ data. Journal of Sedimentary Research, 52, 71– 82. https://doi.org/10.1306/212F7EE1-2B24-11D7-8648000102C1865D.

Banner, J. L., & Hanson, G. N., 1990. Calculation of simultaneous isotopic and trace element variations during water-rock interaction with applications to carbonate diagenesis. Geochimica et Cosmochimica Acta, 54(11), 3123–3137. https://doi.org/10.1016/0016-7037(90)90128-8.

Bao, S.-X., Zhou, H.-Y., Peng, X.-T., Ji, F.-W., & Yao, H.-Q., 2008. Geochemistry of REE and yttrium in hydrothermal fluids from the Endeavour segment, Juan de Fuca Ridge. Geochemical Journal, 42(4), 359–370. https://doi.org/10.2343/geochemj.42.359.

Barley, M. E., 1993. Volcanic, sedimentary and tectonostratigraphic environments of the ~3.46 Ga Warrawoona Megasequence: A review. Precambrian Research, 60(1–4), 47–67. https://doi.org/10.1016/0301-9268(93)90044-3.

Barley, M. E., Sylvester, G. C., Groves, D. I., Borley, G. D., & Rogers, N., 1984. Archaean calc-alkaline volcanism in the Pilbara Block, Western Australia. Precambrian Research, 24(3), 285–319. https://doi.org/10.1016/0301-9268(84)90062-7.

Barrett, T. J., & Jarvis, I., 1988. Rare-earth element geochemistry of metalliferous sediments from DSDP Leg 92: The East Pacific Rise transect. Chemical Geology, 67(3), 243–259. https://doi.org/10.1016/0009-2541(88)90131-3.

Bathurst, R.G.C., 1975. Carbonate Sediment and Their Diagenesis. Amsterdam: Elsevier. 2nd ed.

Bau, M., 1991. Rare-earth element mobility during hydrothermal and metamorphic fluid-rock interaction and the significance of the oxidation state of europium. Chemical Geology, 93(3), 219–230. https://doi.org/10.1016/0009-2541(91)90115-8.

Bau, M., 1993. Effects of syn- and post-depositional processes on the rare-earth element distribution in Precambrian iron-formations. European Journal of Mineralogy, 5(2), 257–268. https://doi.org/10.1127/ejm/5/2/0257.

Bau, M., 1996. Controls on the fractionation of isovalent trace elements in magmatic and aqueous systems: Evidence from Y/Ho, Zr/Hf, and lanthanide tetrad effect. Contributions to Mineralogy and Petrology, 123(3), 323–333. https://doi.org/10.1007/s004100050159.

Bau, M., 1999. Scavenging of dissolved yttrium and rare earths by precipitating iron oxyhydroxide: Experimental evidence for Ce oxidation, Y-Ho fractionation, and lanthanide tetrad effect. Geochimica et Cosmochimica Acta, 63(1), 67–77. https://doi.org/10.1016/S0016-7037(99)00014-9.

Bau, M., & Alexander, B. W., 2009. Distribution of high field strength elements, Y, Zr, REE, Hf, Ta, Th, U) in adjacent magnetite and chert bands and in reference standards FeR-3 and FeR-4 from the Temagami iron-formation, Canada, and the redox level of the Neoarchean ocean. Precambrian Research, 174(3), 337–346. https://doi.org/10.1016/j.precamres.2009.08.007.

Bau, M., & Dulski, P., 1996. Distribution of yttrium and rare-earth elements in the Penge and Kuruman iron-formations, Transvaal Supergroup, South Africa. Precambrian Research, 79(1), 37–55. https://doi.org/10.1016/0301-9268(95)00087-9.

Bau, M., & Dulski, P., 1999. Comparing yttrium and rare earths in hydrothermal fluids from the Mid-Atlantic Ridge: Implications for Y and REE behaviour during near-vent mixing and for the Y/Ho ratio of Proterozoic seawater. Chemical Geology, 155(1), 77–90. https://doi.org/10.1016/S0009-2541(98)00142-9.

Bau, M., & Möller, P., 1992. Rare earth element fractionation in metamorphogenic hydrothermal calcite, magnesite and siderite. Mineralogy and Petrology, 45(3), 231–246. https://doi.org/10.1007/BF01163114.

Bau, M., Balan, S., Schmidt, K., & Koschinsky, A., 2010. Rare earth elements in mussel shells of the Mytilidae family as tracers for hidden and fossil high-temperature hydrothermal systems. Earth and Planetary Science Letters, 299(3), 310–316. https://doi.org/10.1016/j.epsl.2010.09.011.

Bau, M., Koschinsky, A., Dulski, P., & Hein, J. R., 1996. Comparison of the partitioning behaviours of yttrium, rare earth elements, and titanium between hydrogenetic marine ferromanganese crusts and seawater. Geochimica et Cosmochimica Acta, 60(10), 1709–1725. https://doi.org/10.1016/0016-7037(96)00063-4.

Bau, M., Usui, A., Pracejus, B., Mita, N., Kanai, Y., Irber, W., & Dulski, P., 1998. Geochemistry of low-temperature water–rock interaction: Evidence from natural waters, andesite, and iron-oxyhydroxide precipitates at Nishiki-numa iron-spring, Hokkaido, Japan. Chemical Geology, 151(1), 293–307. https://doi.org/10.1016/S0009-2541(98)00086-2.

Baumgartner, R. J., Van Kranendonk, M. J., Wacey, D., Fiorentini, M. L., Saunders, M., Caruso, S., Pages, A., Homann, M., & Guagliardo, P., 2019. Nano−porous pyrite and organic matter in 3.5-billion-year-old stromatolites record primordial life. Geology, 47(11), 1039–1043. https://doi.org/10.1130/G46365.1.

Bickle, M. J., Bettenay, L. F., Barley, M. E., Chapman, H. J., Groves, D. I., Campbell, I. H., & de Laeter, J. R., 1983. A 3500 Ma plutonic and volcanic calc-alkaline province in the Archaean East Pilbara Block. Contributions to Mineralogy and Petrology, 84(1), 25–35. https://doi.org/10.1007/BF01132327.

Bickle, M. J., Bettenay, L. F., Chapman, H. J., Groves, D. I., McNaughton, N. J., Campbell, I. H., & de Laeter, J. R., 1993. Origin of the 3500-3300 Ma calc-alkaline rocks in the Pilbara Archaean: Isotopic

and geochemical constraints from the Shaw Batholith. Precambrian Research, 60(1), 117–149. https://doi.org/10.1016/0301-9268(93)90047-6.

Bilal, B. A., 1991. Thermodynamic Study of Eu^{3+} /Eu^{2+} Redox Reaction in Aqueous Solutions at Elevated Temperatures and Pressures by Means of Cyclic Voltammetry. Zeitschrift Für Naturforschung A, 46(12), 1108–1116. https://doi.org/10.1515/zna-1991-1216.

Biswas, S., 1983. Microfacies Analysis of Limestones. Journal Geological Society of India. https://doi.org/10.17491/jgsi/1983/241006.

Boelrijk, N. A. I. M., 1968. A general formula for "double" isotope dilution analysis. Chemical Geology, 3(4), 323–325. https://doi.org/10.1016/0009-2541(68)90037-5.

Boles, J. R., 1978. Active ankerite cementation in the subsurface Eocene of southwest Texas. Contributions to Mineralogy and Petrology, 68(1), 13–22. https://doi.org/10.1007/BF00375443.

Bolhar, R., Van Kranendonk, M. J., & Kamber, B. S., 2005. A trace element study of siderite–jasper banded iron formation in the 3.45 Ga Warrawoona Group, Pilbara Craton—Formation from hydrothermal fluids and shallow seawater. Precambrian Research, 137(1), 93–114. https://doi.org/10.1016/j.precamres.2005.02.001.

Brand, U., & Veizer, J., 1980. Chemical Diagenesis of a Multicomponent Carbonate System-1: Trace Elements. Journal of Sedimentary Research, 50, 1219-1236. https://doi.org/10.1306/212F7BB7-2B24-11D7-8648000102C1865D.

Brand, U., & Veizer, J., 1981. Chemical Diagenesis of a Multicomponent Carbonate System -2: Stable Isotopes. Journal of Sedimentary Research, 51, 987-997. https://doi.org/10.1306/212F7DF6-2B24-11D7-8648000102C1865D.

Brauhart, C. W., Huston, D. L., & Andrew, A. S., 2000. Oxygen isotope mapping in the Panorama VMS district, Pilbara Craton, Western Australia: Applications to estimating temperatures of alteration and to exploration. Mineralium Deposita, 35(8), 727–740. https://doi.org/10.1007/s001260050275.

Brenner, A. R., Fu, R. R., Brown, A. J., Hodgin, E. B., Flannery, D. T., & Schmitz, M. D., 2024. Episodic Seafloor Hydrothermal Alteration as a Source of Stable Remagnetizations in Archean Volcanic Rocks. Geochemistry, Geophysics, Geosystems, 25(12), e2024GC011799. https://doi.org/10.1029/2024GC011799.

Buick, R., & Dunlop, J. S. R., 1990. Evaporitic sediments of Early Archaean age from the Warrawoona Group, North Pole, Western Australia. Sedimentology, 37(2), 247–277. https://doi.org/10.1111/j.1365-3091.1990.tb00958.x.

Buick, R., & Barnes, K. R., 1984. Cherts in the Warrawoona group: early Archaean silicified sediments deposited in shallow-water environments. In: Muhling, J.R., Groves, D.I., Blake, T.S. (Eds.), Archaean and Proterozoic Basins of the Pilbara, Western Australia: Evolution and Mineralization Potential. The Geology Department and University Extension, University of Western Australia, pp. 3753. Publication 9.

Burke, W. H., Denison, R. E., Hetherington, E. A., Koepnick, R. B., Nelson, H. F., & Otto, J. B., 1982. Variation of seawater $^{87}Sr/^{86}Sr$ throughout Phanerozoic time. Geology, 10(10), 516–519. https://doi.org/10.1130/0091-7613(1982)10%253C516:VOSSTP%253E2.0.CO;2.

Byerly, G. R., Lowe, D. R., Wooden, J. L., & Xie, X., 2002. An Archean Impact Layer from the Pilbara and Kaapvaal Cratons. Science, 297(5585), 1325–1327. https://doi.org/10.1126/science.1073934.

Cantrell, K. J., & Byrne, R. H., 1987. Rare earth element complexation by carbonate and oxalate ions. Geochimica et Cosmochimica Acta, 51(3), 597–605. https://doi.org/10.1016/0016-7037(87)90072-X.

Capo, R. C., & DePaolo, D. J., 1990. Seawater Strontium Isotopic Variations from 2.5 Million Years Ago to the Present. Science, 249(4964), 51–55. https://doi.org/10.1126/science.249.4964.51.

Caruso, S., Van Kranendonk, M. J., Baumgartner, R. J., Fiorentini, M. L., & Forster, M. A., 2021. The role of magmatic fluids in the ~3.48 Ga Dresser Caldera, Pilbara Craton: New insights from the geochemical investigation of hydrothermal alteration. Precambrian Research, 362, 106299. https://doi.org/10.1016/j.precamres.2021.106299.

Cathelineau, M., & Nieva, D., 1985. A chlorite solid solution geothermometer the Los Azufres (Mexico) geothermal system. Contributions to Mineralogy and Petrology, 91(3), 235–244. https://doi.org/10.1007/BF00413350.

Catling, D. C., & Zahnle, K. J., 2020. The Archean atmosphere. Science Advances, 6(9), eaax1420. https://doi.org/10.1126/sciadv.aax1420.

Champion, D. C., & Smithies, R. H., 2007. Chapter 4.3 Geochemistry of Paleoarchean Granites of the East Pilbara Terrane, Pilbara Craton, Western Australia: Implications for Early Archean Crustal Growth. In Van Kranendonk, M. J., Smithies, R. H., & Bennett, V. C. (Eds), Developments in Precambrian Geology, Vol. 15, pp. 369–409. Elsevier. https://doi.org/10.1016/S0166-2635(07)15043-X.

Charlou, J. L., Donval, J. P., Fouquet, Y., Jean-Baptiste, P., & Holm, N., 2002. Geochemistry of high H_2 and CH_4 vent fluids issuing from ultramafic rocks at the Rainbow hydrothermal field, 36°14′N, MAR). Chemical Geology, 191(4), 345–359. https://doi.org/10.1016/S0009-2541(02)00134-1.

ChemGlobe, 2026, Periodic Table of the Elements, https://chemglobe.org/ptoe/ (accessed 10 February 2026).

Chen, X., Zhou, Y., & Shields, G. A., 2022. Progress towards an improved Precambrian seawater 87Sr/86Sr curve. Earth-Science Reviews, 224, 103869. https://doi.org/10.1016/j.earscirev.2021.103869.

Chester, R., 2009. Marine geochemistry. John Wiley & Sons.

Coogan, L. A., & Gillis, K. M., 2013. Evidence that low-temperature oceanic hydrothermal systems play an important role in the silicate-carbonate weathering cycle and long-term climate regulation. Geochemistry, Geophysics, Geosystems, 14(6), 1771–1786. https://doi.org/10.1002/ggge.20113.

Coogan, L. A., & Gillis, K. M., 2018. Low-Temperature Alteration of the Seafloor: Impacts on Ocean Chemistry. Annual Review of Earth and Planetary Sciences, 46(1), 21–45. https://doi.org/10.1146/annurev-earth-082517-010027.

Dawson, J., & Hinton, R., 2003. Trace-element content and partitioning in calcite, dolomite and apatite in carbonatite, Phalaborwa, South Africa. Mineralogical Magazine, 67, 921-930. https://doi.org/10.1180/0026461036750151.

De Baar, H. J. W., Bacon, M. P., Brewer, P. G., & Bruland, K. W., 1985. Rare earth elements in the Pacific and Atlantic Oceans. Geochimica et Cosmochimica Acta, 49(9), 1943–1959. https://doi.org/10.1016/0016-7037(85)90089-4.

de Wit, M. J., & Furnes, H., 2016. 3.5-Ga hydrothermal fields and diamictites in the Barberton Greenstone Belt—Paleoarchean crust in cold environments. Science Advances, 2(2), e1500368. https://doi.org/10.1126/sciadv.1500368.

Debruyne, D., Hulsbosch, N., & Muchez, P., 2016. Unraveling rare earth element signatures in hydrothermal carbonate minerals using a source–sink system. Ore Geology Reviews, 72, 232–252. https://doi.org/10.1016/j.oregeorev.2015.07.022.

Degens, E. T., & Epstein, S., 1964. Oxygen and carbon isotope ratios in coexisting calcites and dolomites from recent and ancient sediments. Geochimica et Cosmochimica Acta, 28(1), 23–44. https://doi.org/10.1016/0016-7037(64)90053-5.

Degens, E. T., Wong, H. K., Kempe, S., & Kurtman, F., 1984. A geological study of lake van, Eastern Turkey. Geologische Rundschau, 73(2), 701–734. https://doi.org/10.1007/BF01824978.

Djokic, T., Van Kranendonk, M. J., Campbell, K. A., Havig, J. R., Walter, M. R., & Guido, D. M., 2021. A Reconstructed Subaerial Hot Spring Field in the ~3.5 Billion-Year-Old Dresser Formation, North Pole Dome, Pilbara Craton, Western Australia. Astrobiology, 21(1), 1–38. https://doi.org/10.1089/ast.2019.2072.

Djokic, T., Van Kranendonk, M. J., Campbell, K. A., Walter, M. R., & Ward, C. R., 2017. Earliest signs of life on land preserved in ca. 3.5 Ga hot spring deposits. Nature Communications, 8(1), 15263. https://doi.org/10.1038/ncomms15263.

Douville, E., Bienvenu, P., Charlou, J. L., Donval, J. P., Fouquet, Y., Appriou, P., & Gamo, T., 1999. Yttrium and rare earth elements in fluids from various deep-sea hydrothermal systems. Geochimica et Cosmochimica Acta, 63(5), 627–643. https://doi.org/10.1016/S0016-7037(99)00024-1.

Doyle, M. G., & Allen, R. L., 2003. Subsea-floor replacement in volcanic-hosted massive sulfide deposits. Ore Geology Reviews, 23(3), 183–222. https://doi.org/10.1016/S0169-1368(03)00035-0.

Duda, J.-P., Thiel, V., Bauersachs, T., Mißbach, H., Reinhardt, M., Schäfer, N., Van Kranendonk, M. J., & Reitner, J.: Ideas and perspectives: hydrothermally driven redistribution and sequestration of early Archaean biomass–the "hydrothermal pump hypothesis", Biogeosciences, 15, 1535–1548, 2018.

Dymek, R. F., Brothers, S. C., & Schiffries, C. M., 1988. Petrogenesis of Ultramafic Metamorphic Rocks from the 3800 Ma Isua Supracrustal Belt, West Greenland. Journal of Petrology, 29(6), 1353–1397. https://doi.org/10.1093/petrology/29.6.1353.

Fantle, M. S., & DePaolo, D. J., 2006. Sr isotopes and pore fluid chemistry in carbonate sediment of the Ontong Java Plateau: Calcite recrystallization rates and evidence for a rapid rise in seawater Mg over the last 10 million years. Geochimica et Cosmochimica Acta, 70(15), 3883–3904. https://doi.org/10.1016/j.gca.2006.06.009.

Fantle, M. S., Barnes, B. D., & Lau, K. V., 2020. The Role of Diagenesis in Shaping the Geochemistry of the Marine Carbonate Record. Annual Review of Earth and Planetary Sciences, 48(1), 549–583. https://doi.org/10.1146/annurev-earth-073019-060021.

Fischer, R., & Gerya, T., 2016. Early Earth plume-lid tectonics: A high-resolution 3D numerical modelling approach. Journal of Geodynamics, 100, 198–214. https://doi.org/10.1016/j.jog.2016.03.004.

Flament, N., Coltice, N., & Rey, P. F., 2013. The evolution of the 87Sr/86Sr of marine carbonates does not constrain continental growth. Precambrian Research, 229, 177–188. https://doi.org/10.1016/j.precamres.2011.10.009.

Flannery, D. T., Allwood, A. C., Summons, R. E., Williford, K. H., Abbey, W., Matys, E. D., & Ferralis, N., 2018. Spatially-resolved isotopic study of carbon trapped in ~3.43 Ga Strelley Pool Formation stromatolites. Geochimica et Cosmochimica Acta, 223, 21–35. https://doi.org/10.1016/j.gca.2017.11.028.

Flügel, E., 2004. Microfacies of Carbonate Rocks: Analysis, Interpretation and Application. https://doi.org/10.5860/choice.42-3437.

Flügel, E., Munnecke, A., 2010. Microfacies of carbonate rocks: analysis, interpretation and application. Berlin: Springer, 2nd Edition).

Galeczka, I., Wolff-Boenisch, D., Oelkers, E. H., & Gislason, S. R., 2014. An experimental study of basaltic glass–H_2O–CO_2 interaction at 22 and 50°C: Implications for subsurface storage of CO_2. Geochimica et Cosmochimica Acta, 126, 123–145. https://doi.org/10.1016/j.gca.2013.10.044.

Gao, Z., Zhu, X., Wang, D., Pan, C., Yan, B., & Li, J., 2021. Insights into hydrothermal controls and processes leading to the formation of the Late Ediacaran Gaoyan stratiform manganese-carbonate deposit, Southwest China. Ore Geology Reviews, 139, 104524. https://doi.org/10.1016/j.oregeorev.2021.104524.

Gardiner, N. J., Wacey, D., Kirkland, C. L., Johnson, T. E., & Jeon, H., 2019. Zircon U–Pb, Lu–Hf and O isotopes from the 3414 Ma Strelley Pool Formation, East Pilbara Terrane, and the Palaeoarchaean emergence of a cryptic cratonic core. Precambrian Research, 321, 64–84. https://doi.org/10.1016/j.precamres.2018.11.023.

Gifkins, C., Herrmann, W., & Large, R. R., 2005. Altered volcanic rocks: A guide to description and interpretation. University of Tasmania.

Gillis, K. M., Muehlenbachs, K., Stewart, M., Gleeson, T., & Karson, J., 2001. Fluid flow patterns in fast spreading East Pacific Rise crust exposed at Hess Deep. Journal of Geophysical Research: Solid Earth, 106(B11), 26311–26329. https://doi.org/10.1029/2000JB000038.

Glikson, A. Y., & Hickman, A. H., 1981. Geochemistry of Archaean Volcanic Successions, Eastern Pilbara Block, Western Australia. Australian Bureau of Mineral Resources, Geology and Geophysics. Record 1981/36, 56 p.

Groves, D. I., Dunlop, J. S. R., & Buick, R., 1981. An early habitat of life. Scientific American, 245(4): 64-73.

Gudbrandsson, S., Wolff-Boenisch, D., Gislason, S. R., & Oelkers, E. H., 2011. An experimental study of crystalline basalt dissolution from $2 \leqslant pH \leqslant 11$ and temperatures from 5 to 75 °C. Geochimica et Cosmochimica Acta, 75(19), 5496–5509. https://doi.org/10.1016/j.gca.2011.06.035.

Gutzmer, J., Banks, D. A., Lüders, V., Hoefs, J., Beukes, N. J., & von Bezing, K. L., 2003. Ancient sub-seafloor alteration of basaltic andesites of the Ongeluk Formation, South Africa: Implications for the chemistry of Paleoproterozoic seawater. Chemical Geology, 201(1), 37–53. https://doi.org/10.1016/S0009-2541(03)00225-0.

Gysi, A. P., & Stefánsson, A., 2012. CO_2-water–basalt interaction. Low temperature experiments and implications for CO_2 sequestration into basalts. Geochimica et Cosmochimica Acta, 81, 129–152. https://doi.org/10.1016/j.gca.2011.12.012.

Hao, J., Knoll, A. H., Huang, F., Hazen, R. M., & Daniel, I., 2020. Cycling phosphorus on the Archean Earth: Part I. Continental weathering and riverine transport of phosphorus. Geochimica et Cosmochimica Acta, 273, 70–84. https://doi.org/10.1016/j.gca.2020.01.027.

Hathorne, E. C., Stichel, T., Brück, B., & Frank, M., 2015. Rare earth element distribution in the Atlantic sector of the Southern Ocean: The balance between particle scavenging and vertical supply. Marine Chemistry, 177, 157–171. https://doi.org/10.1016/j.marchem.2015.03.011.

Hayes, J. M., & Waldbauer, J. R., 2006. The carbon cycle and associated redox processes through time. Philosophical Transactions of the Royal Society B: Biological Sciences, 361(1470), 931–950. https://doi.org/10.1098/rstb.2006.1840.

He, M., Cai, Y., Zhao, X., Xue, G., Lu, Y., Cheng, X., Huang, S., Wang, G., Li, R., Wang, T., Ma, L., Wei, Y., Wu, Y., Lei, S., Jia, X., Li, H., Chang, H., Yan, H., & Cheng, H., 2024. Calcite recrystallization and its impact on speleothem geochemistry. Sedimentary Geology, 470, 106725. https://doi.org/10.1016/j.sedgeo.2024.106725.

Heft, K. L., Gillis, K. M., Pollock, M. A., Karson, J. A., & Klein, E. M., 2008. Role of upwelling hydrothermal fluids in the development of alteration patterns at fast spreading ridges: Evidence from the sheeted dike complex at Pito Deep. Geochemistry, Geophysics, Geosystems, 9(5). https://doi.org/10.1029/2007GC001926.

Hegner, E., Rajesh, S., Willbold, M., Mueller, D., Joachimski, M., Hofmann, M., Linnemann, U., Zieger, J., Pradeepkumar, & A.P., 2020. Sediment-derived origin of the putative Munnar carbonatite, South India. Journal of Asian Earth Sciences 200, 10.1016/j.jseaes.2020.104432.

Hendry, J. P., Wilkinson, M., Fallick, A. E., & Haszeldine, R. S., 2000. Ankerite Cementation in Deeply Buried Jurassic Sandstone Reservoirs of the Central North Sea. Journal of Sedimentary Research, 70(1), 227–239. https://doi.org/10.1306/2DC4090D-0E47-11D7-8643000102C1865D.

Herwartz, D., Pack, A., & Nagel, T. J., 2021. A CO_2 greenhouse efficiently warmed the early Earth and decreased seawater $^{18}O/^{16}O$ before the onset of plate tectonics. Proceedings of the National Academy of Sciences, 118(23), e2023617118. https://doi.org/10.1073/pnas.2023617118.

Hess, J., Bender, M. L., & Schilling, J.-G., 1986. Evolution of the Ratio of Strontium-87 to Strontium-86 in Seawater from Cretaceous to Present. Science, 231(4741), 979–984. https://doi.org/10.1126/science.231.4741.979.

Hickman, A. H., 1983. Geology of the Pilbara Block and its Environs. Bulletin 127. Western Australia Geological Survey, 268.

Hickman, A. H., & Van Kranendonk, M. J., 2004. Diapiric processes in the formation of Archaean continental crust, East Pilbara granite-greenstone terrane, Australia. In: Eriksson, P.G., Altermann, W., Nelson, D.R., Mueller, W.U., Catuneau, O. (Eds.), The Precambrian Earth: Tempos and Events. Developments in Precambrian Geology, Elsevier, Amsterdam, vol. 12, pp. 118-139.

Hickman, A. H., & Van Kranendonk, M. J., 2012. A Billion Years of Earth History: A Geological Transect Through the Pilbara Craton and the Mount Bruce Supergroup-a Field Guide to Accompany 34th IGC Excursion WA-2. Geological Survey of Western Australia.

Hickman-Lewis, K., Gourcerol, B., Westall, F., Manzini, D., & Cavalazzi, B., 2020. Reconstructing Palaeoarchaean microbial biomes flourishing in the presence of emergent landmasses using trace and rare earth element systematics. Precambrian Research, 342, 105689. https://doi.org/10.1016/j.precamres.2020.105689.

Hoefs, J., 2018. Stable isotope geochemistry, eighth ed. Springer.

Hohl, S. V., Lin, Y.-B., Wei, H.-Z., Wei, G.-Y., & Viehmann, S., 2024. Barium isotopes in stromatolites through deep-time: A novel tracer for metal cycling in the photic zone. Earth and Planetary Science Letters, 632, 118639. https://doi.org/10.1016/j.epsl.2024.118639.

Hongo, Y., & Nozaki, Y., 2001. Rare earth element geochemistry of hydrothermal deposits and Calyptogena shell from the Iheya Ridge vent field, Okinawa Trough. Geochemical Journal, 35(5), 347–354. https://doi.org/10.2343/geochemj.35.347.

Huston, D. L., Morant, P., Pirajno, F., Cummins, B., Baker, D., & Mernagh, T. P., 2007. Chapter 4.4 Paleoarchean Mineral Deposits of the Pilbara Craton: Genesis, Tectonic Environment and Comparisons with Younger Deposits. In Van Kranendonk, M. J., Smithies, R. H., & Bennett, V. C. (Eds), Developments in Precambrian Geology. Elsevier, Vol. 15, pp. 411–450. https://doi.org/10.1016/S0166-2635(07)15044-1.

Hwang, J., 1988. Dissolution of Chlorite and Sericite by the Treatment with Dilute H2SO4 Solution. Journal of the Clay Science Society of Japan, 28, 119-125. https://doi.org/10.11362/jcssjnendokagaku1961.28.3_119.

Jaffrés, J. B. D., Shields, G. A., & Wallmann, K., 2007. The oxygen isotope evolution of seawater: A critical review of a long-standing controversy and an improved geological water cycle model for the past 3.4 billion years. Earth-Science Reviews, 83(1), 83–122. https://doi.org/10.1016/j.earscirev.2007.04.002.

Jenner, F. E., Bennett, V. C., Nutman, A. P., Friend, C. R. L., Norman, M. D., & Yaxley, G., 2009. Evidence for subduction at 3.8 Ga: Geochemistry of arc-like metabasalts from the southern edge of the Isua Supracrustal Belt. Chemical Geology, 261(1), 83–98. https://doi.org/10.1016/j.chemgeo.2008.09.016.

Johannessen, K. C., Vander Roost, J., Dahle, H., Dundas, S. H., Pedersen, R. B., & Thorseth, I. H., 2017. Environmental controls on biomineralization and Fe-mound formation in a low-temperature hydrothermal system at the Jan Mayen Vent Fields. Geochimica et Cosmochimica Acta, 202, 101–123. https://doi.org/10.1016/j.gca.2016.12.016.

Johannesson, K. H., Hawkins, D. L., & Cortés, A., 2006. Do Archean chemical sediments record ancient seawater rare earth element patterns? Geochimica et Cosmochimica Acta, 70(4), 871–890. https://doi.org/10.1016/j.gca.2005.10.013.

Johnson, B. W., & Wing, B. A., 2020. Limited Archaean continental emergence reflected in an early Archaean ^{18}O-enriched ocean. Nature Geoscience, 13(3), 243–248. https://doi.org/10.1038/s41561-020-0538-9.

Johnson, C. M., Zheng, X.-Y., Djokic, T., Van Kranendonk, M. J., Czaja, A. D., Roden, E. E., & Beard, B. L., 2022. Early Archean biogeochemical iron cycling and nutrient availability: New insights from a 3.5 Ga land-sea transition. Earth-Science Reviews, 228, 103992. https://doi.org/10.1016/j.earscirev.2022.103992.

Johnson, T. E., Brown, M., Gardiner, N. J., Kirkland, C. L., & Smithies, R. H., 2017. Earth's first stable continents did not form by subduction. Nature, 543(7644), 239–242. https://doi.org/10.1038/nature21383.

Jones, C., Nomosatryo, S., Crowe, S. A., Bjerrum, C. J., & Canfield, D. E., 2015. Iron oxides, divalent cations, silica, and the early earth phosphorus crisis. Geology, 43(2), 135–138. https://doi.org/10.1130/G36044.1.

Kamber, B. S., & Webb, G. E., 2001. The geochemistry of late Archaean microbial carbonate: Implications for ocean chemistry and continental erosion history. Geochimica et Cosmochimica Acta, 65(15), 2509–2525. https://doi.org/10.1016/S0016-7037(01)00613-5.

Kamber, B. S., Bolhar, R., & Webb, G. E., 2004). Geochemistry of late Archaean stromatolites from Zimbabwe: Evidence for microbial life in restricted epicontinental seas. Precambrian Research, 132(4), 379–399. https://doi.org/10.1016/j.precamres.2004.03.006

Kamber, B. S., Greig, A., & Collerson, K. D., 2005. A new estimate for the composition of weathered young upper continental crust from alluvial sediments, Queensland, Australia. Geochimica et Cosmochimica Acta, 69(4), 1041–1058. https://doi.org/10.1016/j.gca.2004.08.020.

Kastner, M., Gieskes, J. M., & Hu, J.-Y., 1986. Carbonate recrystallization in basal sediments: Evidence for convective fluid flow on a ridge flank. Nature, 321(6066), 158–161. https://doi.org/10.1038/321158a0.

Kato, Y., & Nakamura, K., 2003. Origin and global tectonic significance of Early Archean cherts from the Marble Bar greenstone belt, Pilbara Craton, Western Australia. Precambrian Research, 125(3), 191–243. https://doi.org/10.1016/S0301-9268(03)00043-3.

Kempe, S., 1990. Alkalinity: the link between anaerobic basins and shallow water carbonates?, Naturwissenschaften, 77, 426–427, https://doi.org/10.1007/BF01135940.

Killingley, J. S., 1983. Effects of diagenetic recrystallization on $^{18}O/^{16}O$ values of deep-sea sediments. Nature, 301(5901), 594–597. https://doi.org/10.1038/301594a0.

Kitajima, K., Maruyama, S., Utsunomiya, S., & Liou, J. G., 2001. Seafloor hydrothermal alteration at an Archaean mid-ocean ridge. Journal of Metamorphic Geology, 19(5), 583–599. https://doi.org/10.1046/j.0263-4929.2001.00330.x.

Klinkhammer, G. P., Elderfield, H., Edmond, J. M., & Mitra, A., 1994. Geochemical implications of rare earth element patterns in hydrothermal fluids from mid-ocean ridges. Geochimica et Cosmochimica Acta, 58(23), 5105–5113. https://doi.org/10.1016/0016-7037(94)90297-6.

Komiya, T., Hirata, T., Kitajima, K., Yamamoto, S., Shibuya, T., Sawaki, Y., Ishikawa, T., Shu, D., Li, Y., & Han, J., 2008. Evolution of the composition of seawater through geologic time, and its influence on the evolution of life. Gondwana Research, 14(1–2), 159–174. https://doi.org/10.1016/j.gr.2007.10.006.

Koschinsky, A., Garbe-Schönberg, D., Sander, S., Schmidt, K., Gennerich, H.-H., & Strauss, H., 2008. Hydrothermal venting at pressure-temperature conditions above the critical point of seawater, 5°S on the Mid-Atlantic Ridge. Geology, 36(8), 615. https://doi.org/10.1130/G24726A.1.

Kroopnick, P., 1980. The distribution of ^{13}C in the Atlantic Ocean. Earth and Planetary Science Letters, 49(2), 469–484. https://doi.org/10.1016/0012-821X(80)90088-6.

Kump, L. R., & Barley, M. E., 2007. Increased subaerial volcanism and the rise of atmospheric oxygen 2.5 billion years ago. Nature, 448(7157), 1033–1036. https://doi.org/10.1038/nature06058.

Kutyrev, A., Bindeman, I. N., O'Neil, J., & Rizo, H., 2024. Seawater-oceanic crust interaction constrained by triple oxygen and hydrogen isotopes in rocks from the Saglek-Hebron complex, NE

Canada: Implications for moderately low-$\delta^{18}O$ Eoarchean Ocean. Chemical Geology, 670, 122378. https://doi.org/10.1016/j.chemgeo.2024.122378.

Lahiri, N., Kovarik, L., Taylor, S. D., Crum, J. V., Ilton, E. S., Depp, C. T., Miller, Q. R. S., & Schaef, H. T., 2025. Complex carbonate phases drive geologic CO_2 mineralization. Communications Earth & Environment, 6(1), 344. https://doi.org/10.1038/s43247-025-02273-6.

Lambert, I. B., Donnelly, T. H., Dunlop, J. S. R., & Groves, D. I., 1978). Stable isotopic compositions of early Archaean sulphate deposits of probable evaporitic and volcanogenic origins. Nature, 276(5690), 808–811. https://doi.org/10.1038/276808a0

Lawrence, M. G., Greig, A., Collerson, K. D., & Kamber, B. S., 2006. Rare Earth Element and Yttrium Variability in South East Queensland Waterways. Aquatic Geochemistry, 12(1), 39–72. https://doi.org/10.1007/s10498-005-4471-8.

Ledevin, M., Arndt, N., Simionovici, A., Jaillard, E., & Ulrich, M., 2014. Silica precipitation triggered by clastic sedimentation in the Archean: New petrographic evidence from cherts of the Kromberg type section, South Africa. Precambrian Research, 255, 316–334. https://doi.org/10.1016/j.precamres.2014.10.009.

Lee, D., & Carpenter, S. J., 2001. Isotopic disequilibrium in marine calcareous algae. Chemical Geology, 172(3), 307–329. https://doi.org/10.1016/S0009-2541(00)00258-8.

Lepot, K., 2020. Signatures of early microbial life from the Archean (4 to 2.5 Ga) eon. Earth-Science Reviews, 209, 103296. https://doi.org/10.1016/j.earscirev.2020.103296.

Lindsay, J. F., Brasier, M. D., McLoughlin, N., Green, O. R., Fogel, M., Steele, A., & Mertzman, S. A., 2005. The problem of deep carbon—An Archean paradox. Precambrian Research, 143(1), 1–22. https://doi.org/10.1016/j.precamres.2005.09.003.

Ling, H.-F., Chen, X., Li, D., Wang, D., Shields-Zhou, G. A., & Zhu, M., 2013. Cerium anomaly variations in Ediacaran–earliest Cambrian carbonates from the Yangtze Gorges area, South China: Implications for oxygenation of coeval shallow seawater. Precambrian Research, 225, 110–127. https://doi.org/10.1016/j.precamres.2011.10.011.

Lohmann, K. C., 1988. Eocene endo- and exoskeleton diagenesis in corals from the shallow Bahama fore-reef, Hole 633A, ODP Leg 101 in the northern Bahamas. Proceedings of the Ocean Drilling Program, Part B: Scientific Results, 101, 607-628.

Lowe, D. R., 1983. Restricted shallow-water sedimentation of Early Archean stromatolitic and evaporitic strata of the Strelley Pool Chert, Pilbara Block, Western Australia. Precambrian Research, 19(3), 239–283. https://doi.org/10.1016/0301-9268(83)90016-5.

Lowe, D. R., Byerly, G. R., 1986. Early Archean silicate spherules of probable impact origin, South Africa and Western Australia. Geology, 14(1), 83–86. https://doi.org/10.1130/0091-7613(1986)14%253C83:EASSOP%253E2.0.CO;2.

Luo, K., Ma, J.-L., Teng, F.-Z., Wei, G.-J., Zhu, G.-H., Zeng, T., & Wang, Z.-B., 2025. Magnesium Isotope Fractionation During Basalt Weathering: An Index of Weathering Fluxes and CO_2 Consumption. Journal of Geophysical Research: Earth Surface, 130(1), e2024JF007774. https://doi.org/10.1029/2024JF007774.

Luong, L. D., Shinjo, R., Hoang, N., Shakirov, R. B., & Syrbu, N., 2018. Spatial variations in dissolved rare earth element concentrations in the East China Sea water column. Marine Chemistry, 205, 1–15. https://doi.org/10.1016/j.marchem.2018.07.004.

Marien, C. S., Jäger, O., Tusch, J., Viehmann, S., Surma, J., Van Kranendonk, M. J., & Münker, C., 2023. Interstitial carbonates in pillowed metabasaltic rocks from the Pilbara Craton, Western Australia: A vestige of Archean seawater chemistry and seawater-rock interactions. Precambrian Research, 394, 107109. https://doi.org/10.1016/j.precamres.2023.107109.

Matthews, A., & Katz, A., 1977. Oxygen isotope fractionation during the dolomitization of calcium carbonate. Geochimica et Cosmochimica Acta, 41(10), 1431–1438. https://doi.org/10.1016/0016-7037(77)90249-6.

McArthur, J. M., Howarth, R. J., & Bailey, T. R., 2001. Strontium Isotope Stratigraphy: LOWESS Version 3: Best Fit to the Marine Sr-Isotope Curve for 0–509 Ma and Accompanying Look-up Table for Deriving Numerical Age. The Journal of Geology, 109(2), 155–170. https://doi.org/10.1086/319243.

McCarthy, G. J., 1971. Divalent europium compounds in the systems Eu Mo O and Eu W O. Materials Research Bulletin, 6(1), 31–39. https://doi.org/10.1016/0025-5408(71)90156-5.

McConnaughey, T. A., 2003. Sub-equilibrium oxygen-18 and carbon-13 levels in biological carbonates: Carbonate and kinetic models. Coral Reefs, 22(4), 316–327. https://doi.org/10.1007/s00338-003-0325-2.

McCulloch, M. T., 1994. Primitive $^{87}Sr/^{86}Sr$ from an Archean barite and conjecture on the Earth's age and origin. Earth and Planetary Science Letters, 126(1), 1–13. https://doi.org/10.1016/0012-821X(94)90238-0.

McDermott, J. M., Sylva, S. P., Ono, S., German, C. R., & Seewald, J. S., 2018. Geochemistry of fluids from Earth's deepest ridge-crest hot-springs: Piccard hydrothermal field, Mid-Cayman Rise. Geochimica et Cosmochimica Acta, 228, 95–118. https://doi.org/10.1016/j.gca.2018.01.021.

McGrail, B. P., Schaef, H. T., Spane, F. A., Cliff, J. B., Qafoku, O., Horner, J. A., Thompson, C. J., Owen, A. T., & Sullivan, C. E., 2017. Field Validation of Supercritical CO2 Reactivity with Basalts. Environmental Science & Technology Letters, 4(1), 6–10. https://doi.org/10.1021/acs.estlett.6b00387.

McNaughton, N. J., Compston, W., & Barley, M. E., 1993. Constraints on the age of the Warrawoona Group, eastern Pilbara Block, Western Australia. Precambrian Research, 60(1), 69–98. https://doi.org/10.1016/0301-9268(93)90045-4.

Melezhik, V. A., Gorokhov, I. M., Fallick, A. E., & Gjelle, S., 2001. Strontium and carbon isotope geochemistry applied to dating of carbonate sedimentation: An example from high-grade rocks of the Norwegian Caledonides. Precambrian Research, 108(3), 267–292. https://doi.org/10.1016/S0301-9268(01)00135-8.

Menefee, A. H., Giammar, D. E., & Ellis, B. R., 2018. Permanent CO_2 Trapping through Localized and Chemical Gradient-Driven Basalt Carbonation. Environmental Science & Technology, 52(15), 8954–8964. https://doi.org/10.1021/acs.est.8b01814.

Michard, A., & Albarède, F., 1986. The REE content of some hydrothermal fluids. Chemical Geology, 55(1), 51–60. https://doi.org/10.1016/0009-2541(86)90127-0.

Michard, A., Albarède, F., Michard, G., Minster, J. F., & Charlou, J. L., 1983. Rare-earth elements and uranium in high-temperature solutions from East Pacific Rise hydrothermal vent field, 13 °N). Nature, 303(5920), 795–797. https://doi.org/10.1038/303795a0.

Mozley, P. S., & Burns, S. J., 1993. Oxygen and carbon isotopic composition of marine carbonate concretions; an overview. Journal of Sedimentary Research, 63(1), 73–83. https://doi.org/10.1306/D4267A91-2B26-11D7-8648000102C1865D.

Nakamura, H., Sano, A., Kagami, S., Yokoyama, T., Ishikawa, A., Komiya, T., & Iwamori, H., 2020. Compositional heterogeneity of Archean mantle estimated from Sr and Nd isotopic systematics of basaltic rocks from North Pole, Australia, and the Isua supracrustal belt, Greenland. Precambrian Research, 347, 105803. https://doi.org/10.1016/j.precamres.2020.105803.

Nakamura, K., & Kato, Y., 2002. Carbonate Minerals in the Warrawoona Group, Pilbara Craton: Implications for Continental Crust, Life, and Global Carbon Cycle in the Early Archean. Resource Geology, 52(2), 91–100. https://doi.org/10.1111/j.1751-3928.2002.tb00122.x.

Nakamura, K., & Kato, Y., 2004. Carbonatization of oceanic crust by the seafloor hydrothermal activity and its significance as a CO2 sink in the Early Archean1. Geochimica et Cosmochimica Acta, 68(22), 4595–4618. https://doi.org/10.1016/j.gca.2004.05.023.

Nijman, W., de Bruijne (K., C.) H., & Valkering, M. E., 1998. Growth fault control of Early Archaean cherts, barite mounds and chert-barite veins, North Pole Dome, Eastern Pilbara, Western Australia. Precambrian Research, 88(1), 25–52. https://doi.org/10.1016/S0301-9268(97)00062-4.

Nishino, H., Fujimori, K., & Akagi, T., 2022. A new experimental method to determine partitioning coefficients of rare earth elements on carbonate, calcite and aragonite) in seawater: Identification of two major factors causing variation: Fe hydroxide adsorption and growth/dissolution inhibition of carbonate. Geochemical Journal, 56(4), 112–128. https://doi.org/10.2343/geochemj.gj22009.

Nothdurft, L. D., Webb, G. E., & Kamber, B. S., 2004. Rare earth element geochemistry of Late Devonian reefal carbonates, Canning Basin, Western Australia: Confirmation of a seawater REE proxy in ancient limestones. Geochimica et Cosmochimica Acta, 68(2), 263–283. https://doi.org/10.1016/S0016-7037(03)00422-8.

Nozaki, Y., Zhang, J., & Amakawa, H., 1997. The fractionation between Y and Ho in the marine environment. Earth and Planetary Science Letters, 148(1), 329–340. https://doi.org/10.1016/S0012-821X(97)00034-4.

Nutman, A. P., Bennett, V. C., Friend, C. R. L., Van Kranendonk, M. J., & Chivas, A. R., 2016. Rapid emergence of life shown by discovery of 3,700-million-year-old microbial structures. Nature, 537(7621), 535–538. https://doi.org/10.1038/nature19355.

Nutman, A. P., Bennett, V. C., Friend, C. R. L., Van Kranendonk, M. J., Rothacker, L., & Chivas, A. R., 2019a. Cross-examining Earth's oldest stromatolites: Seeing through the effects of heterogeneous deformation, metamorphism and metasomatism affecting Isua, Greenland) ~3700 Ma sedimentary rocks. Precambrian Research, 331, 105347. https://doi.org/10.1016/j.precamres.2019.105347.

Nutman, A. P., Friend, C. R. L., Bennett, V. C., Van Kranendonk, M., & Chivas, A. R., 2019b. Reconstruction of a 3700 Ma transgressive marine environment from Isua, Greenland): Sedimentology, stratigraphy and geochemical signatures. Lithos, 346–347, 105164. https://doi.org/10.1016/j.lithos.2019.105164.

O'Neil, J. R., & Epstein, S., 1966. Oxygen Isotope Fractionation in the System Dolomite-Calcite-Carbon Dioxide. Science, 152(3719), 198–201. https://doi.org/10.1126/science.152.3719.198.

Olivarez, A. M., & Owen, R. M., 1989. REE/Fe variations in hydrothermal sediments: Implications for the REE content of seawater. Geochimica et Cosmochimica Acta, 53(3), 757–762. https://doi.org/10.1016/0016-7037(89)90019-7.

Olivarez, A. M., & Owen, R. M., 1991. The europium anomaly of seawater: Implications for fluvial versus hydrothermal REE inputs to the oceans. Chemical Geology, 92(4), 317–328. https://doi.org/10.1016/0009-2541(91)90076-4.

Owen, R. M., & Olivarez, A. M., 1988. Geochemistry of rare earth elements in pacific hydrothermal sediments. Marine Chemistry, 25(2), 183–196. https://doi.org/10.1016/0304-4203(88)90063-1.

Pack, A., Russell, S.S., Shelley, J.M.G., Van Zuilen, M., 2007. Geo- and cosmochemistry of the twin elements yttrium and holmium. Geochim. Cosmochim. Acta 71, 4592–4608. https://doi.org/10.1016/j.gca.2007.07.010

Palme, H., & O'Neill, H. St. C., 2014). 3.1—Cosmochemical Estimates of Mantle Composition. In Holland, H. D., & Turekian, K. K. (Eds), Treatise on Geochemistry, Second Ed. Elsevier, pp. 1–39. https://doi.org/10.1016/B978-0-08-095975-7.00201-1.

Parekh, P. P., Möller, P., Dulski, P., & Bausch, W. M., 1977. Distribution of trace elements between carbonate and non-carbonate phases of limestone. Earth and Planetary Science Letters, 34(1), 39–50. https://doi.org/10.1016/0012-821X(77)90103-0.

Pellerin, A., Thomazo, C., Ader, M., Marin-Carbonne, J., Alleon, J., Vennin, E., & Hofmann, A., 2023. Iron-mediated anaerobic ammonium oxidation recorded in the early Archean ferruginous ocean. Geobiology, 21(3), 277–289. https://doi.org/10.1111/gbi.12540.

Pin, C., Gannoun, A., & Dupont, A., 2014. Rapid, simultaneous separation of Sr, Pb, and Nd by extraction chromatography prior to isotope ratios determination by TIMS and MC-ICP-MS. Journal of Analytical Atomic Spectrometry, 29(10), 1858–1870. https://doi.org/10.1039/C4JA00169A.

Pirajno, F., 2007a. Ancient to modern earth: the role of mantle plumes in the making of continental crust. In: Van Kranendonk, M.J., Smithies, R.H., Bennett, V.C. (Eds.), Earth's Oldest Rocks, Developments in Precambrian Geology, vol. 15. Elsevier, Amsterdam, pp. 1037-1064.

Pirajno, F., 2007b. Mantle plumes, associated intraplate tectono-magmatic processes and ore systems. Episodes 30(1), 6-19.

Planavsky, N., Bekker, A., Rouxel, O. J., Kamber, B., Hofmann, A., Knudsen, A., & Lyons, T. W., 2010. Rare Earth Element and yttrium compositions of Archean and Paleoproterozoic Fe formations revisited: New perspectives on the significance and mechanisms of deposition. Geochimica et Cosmochimica Acta, 74(22), 6387–6405. https://doi.org/10.1016/j.gca.2010.07.021.

Pourmand, A., Dauphas, N., & Ireland, T. J., 2012. A novel extraction chromatography and MC-ICP-MS technique for rapid analysis of REE, Sc and Y: Revising CI-chondrite and Post-Archean Australian Shale, PAAS) abundances. Chemical Geology, 291, 38–54. https://doi.org/10.1016/j.chemgeo.2011.08.011.

Qu, C., Liu, G., & Zhao, Y., 2009. Experimental study on the fractionation of yttrium from holmium during the coprecipitation with calcium carbonates in seawater solutions. Geochemical Journal, 43(6), 403–414. https://doi.org/10.2343/geochemj.1.0036.

Rasmussen, B., & Muhling, J. R., 2023. Organic carbon generation in 3.5-billion-year-old basalt-hosted seafloor hydrothermal vent systems. Science Advances, 9(5), eadd7925. https://doi.org/10.1126/sciadv.add7925.

Rasmussen, B., Muhling, J. R., & Tosca, N. J., 2024. Nanoparticulate apatite and greenalite in oldest, well-preserved hydrothermal vent precipitates. Science Advances, 10(4), eadj4789. https://doi.org/10.1126/sciadv.adj4789.

Ravindran, A., Mezger, K., Balakrishnan, S., Kooijman, E., Schmitt, M., & Berndt, J., 2020. Initial 87Sr/86Sr as a sensitive tracer of Archaean crust-mantle evolution: Constraints from igneous and sedimentary rocks in the western Dharwar Craton, India. Precambrian Research, 337, 105523. https://doi.org/10.1016/j.precamres.2019.105523.

Reitner, J., Wilmsen, M., & Neuweiler, F., 1995. Cenomanian/Turonian sponge microbialite deep-water hardground community, Liencres, Northern Spain). Facies, 32(1), 203–212. https://doi.org/10.1007/BF02536869.

Retallack, G. J., 2018. The oldest known paleosol profiles on Earth: 3.46 Ga Panorama Formation, Western Australia. Palaeogeography, Palaeoclimatology, Palaeoecology, 489, 230–248. https://doi.org/10.1016/j.palaeo.2017.10.013.

Richter, F. M., & DePaolo, D. J., 1988. Diagenesis and Sr isotopic evolution of seawater using data from DSDP 590B and 575. Earth and Planetary Science Letters, 90(4), 382–394. https://doi.org/10.1016/0012-821X(88)90137-9.

Roberts, S., Palmer, M. R., Cooper, M. J., Buchaus, P., & Sargent, D., 2009. REE and Sr isotope characteristics of carbonate within the Cu–Co mineralized sedimentary sequence of the Nchanga Mine, Zambian Copperbelt. Mineralium Deposita, 44(8), 881–891. https://doi.org/10.1007/s00126-009-0254-2.

Roerdink, D. L., Ronen, Y., Strauss, H., & Mason, P. R. D., 2022. Emergence of felsic crust and subaerial weathering recorded in Palaeoarchaean barite. Nature Geoscience, 15(3), 227–232. https://doi.org/10.1038/s41561-022-00902-9.

Romanek, C. S., Grossman, E. L., & Morse, J. W., 1992. Carbon isotopic fractionation in synthetic aragonite and calcite: Effects of temperature and precipitation rate. Geochimica et Cosmochimica Acta, 56(1), 419–430. https://doi.org/10.1016/0016-7037(92)90142-6.

Rouillard, J., Van Kranendonk, M. J., Lalonde, S., Gong, J., & van Zuilen, M. A., 2021. Correlating trace element compositions, petrology, and Raman spectroscopy data in the ∼3.46 Ga Apex chert, Pilbara Craton, Australia. Precambrian Research, 366, 106415. https://doi.org/10.1016/j.precamres.2021.106415.

Rubinson, M., & Clayton, R. N., 1969. Carbon-13 fractionation between aragonite and calcite. Geochimica et Cosmochimica Acta, 33(8), 997–1002. https://doi.org/10.1016/0016-7037(69)90109-4.

Ruhlin, Douglas E; Owen, Robert M, 1986. Contents and accumulation rates of the rare earth and some other elements in metalliferous sediments from DSDP Hole 92-598 [dataset publication series]. Pangaea, https://doi.org/10.1594/PANGAEA.707278.https://doi.org/10.1016/0016-7037(86)90192-4.

Sabau, A., Pipon, Y., Toulhoat, N., Lomenech, C., Jordan, N., Moncoffre, N., Barkleit, A., Marmier, N., Brendler, V., Surblé, S., & Giffaut, E., 2014. Interaction of europium and nickel with calcite studied by Rutherford Backscattering Spectrometry and Time-Resolved Laser Fluorescence Spectroscopy. Nuclear Instruments and Methods in Physics Research Section B: Beam Interactions with Materials and Atoms, 332, 111–116. https://doi.org/10.1016/j.nimb.2014.02.041.

Saccocia, P. J., & Seyfried, W. E., 1994. The solubility of chlorite solid solutions in 3.2 wt% NaCl fluids from 300–400°C, 500 bars. Geochimica et Cosmochimica Acta, 58(2), 567–585. https://doi.org/10.1016/0016-7037(94)90489-8.

Satkoski, A. M., Lowe, D. R., Beard, B. L., Coleman, M. L., & Johnson, C. M., 2016. A high continental weathering flux into Paleoarchean seawater revealed by strontium isotope analysis of 3.26 Ga barite. Earth and Planetary Science Letters, 454, 28–35. https://doi.org/10.1016/j.epsl.2016.08.032.

Satkoski, A. M., Fralick, P., Beard, B. L., & Johnson, C. M., 2017. Initiation of modern-style plate tectonics recorded in Mesoarchean marine chemical sediments. Geochimica et Cosmochimica Acta, 209, 216–232. https://doi.org/10.1016/j.gca.2017.04.024.

Schidlowski, M., 1988. A 3,800-million-year isotopic record of life from carbon in sedimentary rocks. Nature, 333(6171), 313–318. https://doi.org/10.1038/333313a0.

Schier, K., Bau, M., Münker, C., Beukes, N., & Viehmann, S., 2018. Trace element and Nd isotope composition of shallow seawater prior to the Great Oxidation Event: Evidence from stromatolitic bioherms in the Paleoproterozoic Rooinekke and Nelani Formations, South Africa. Precambrian Research, 315, 92–102. https://doi.org/10.1016/j.precamres.2018.07.014.

Schopf, J. W., Kitajima, K., Spicuzza, M. J., Kudryavtsev, A. B., & Valley, J. W., 2017. SIMS analyses of the oldest known assemblage of microfossils document their taxon-correlated carbon isotope compositions. Proceedings of the National Academy of Sciences, 115(1), 53–58. https://doi.org/10.1073/pnas.1718063115.

Schrag, D. P., DePaolo, D. J., & Richter, F. M., 1995. Reconstructing past sea surface temperatures: Correcting for diagenesis of bulk marine carbonate. Geochimica et Cosmochimica Acta, 59(11), 2265–2278. https://doi.org/10.1016/0016-7037(95)00105-9.

Shackleton, N. J. & Kennett, 1975. Paleotemperature history of the Cenozoic and the initiation of Antarctic glaciation: oxygen and carbon isotope analyses in DSDP Sites 277, 279, and 281. Initial Reports Deep Sea Drilling Project, 29, 743-755.

Shannon, R. D., 1976. Revised effective ionic radii and systematic studies of interatomic distances in halides and chalcogenides. Acta Crystallographica Section A, 32(5), 751–767. https://doi.org/10.1107/S0567739476001551.

Sheppard, S. M. F., & Schwarcz, H. P., 1970. Fractionation of carbon and oxygen isotopes and magnesium between coexisting metamorphic calcite and dolomite. Contributions to Mineralogy and Petrology, 26(3), 161–198. https://doi.org/10.1007/BF00373200.

Shibuya, T., Komiya, T., Nakamura, K., Takai, K., & Maruyama, S., 2010. Highly alkaline, high-temperature hydrothermal fluids in the early Archean ocean. Precambrian Research, 182(3), 230–238. https://doi.org/10.1016/j.precamres.2010.08.011.

Shibuya, T., Tahata, M., Kitajima, K., Ueno, Y., Komiya, T., Yamamoto, S., Igisu, M., Terabayashi, M., Sawaki, Y., Takai, K., Yoshida, N., & Maruyama, S., 2012. Depth variation of carbon and oxygen isotopes of calcites in Archean altered upperoceanic crust: Implications for the CO_2 flux from ocean to oceanic crust in the Archean. Earth and Planetary Science Letters, 321–322, 64–73. https://doi.org/10.1016/j.epsl.2011.12.034.

Shields, G., & Veizer, J., 2002. Precambrian marine carbonate isotope database: Version 1.1. Geochemistry, Geophysics, Geosystems, 3(6), 1 of 12–12 12. https://doi.org/10.1029/2001GC000266.

Smith, M. M., Wolery, T. J., & Carroll, S. A., 2013. Kinetics of chlorite dissolution at elevated temperatures and CO_2 conditions. Chemical Geology, 347, 1–8. https://doi.org/10.1016/j.chemgeo.2013.02.017.

Smithies, R. H., Van Kranendonk, M. J., & Champion, D. C., 2005. It started with a plume – early Archaean basaltic proto-continental crust. Earth and Planetary Science Letters, 238(3), 284–297. https://doi.org/10.1016/j.epsl.2005.07.023.

Smrzka, D., Zwicker, J., Bach, W., Feng, D., Himmler, T., Chen, D., & Peckmann, J., 2019. The behavior of trace elements in seawater, sedimentary pore water, and their incorporation into carbonate minerals: A review. Facies, 65(4), 41. https://doi.org/10.1007/s10347-019-0581-4.

Stipp, S. L. S., Christensen, J. T., Lakshtanov, L. Z., Baker, J. A., & Waight, T. E., 2006. Rare Earth element (REE) incorporation in natural calcite: Upper limits for actinide uptake in a secondary phase. Radiochimica Acta, 94(9–11), 523–528. https://doi.org/10.1524/ract.2006.94.9-11.523.

Stockmann, G. J., Wolff-Boenisch, D., Gislason, S. R., & Oelkers, E. H., 2011. Do carbonate precipitates affect dissolution kinetics? 1: Basaltic glass. Chemical Geology, 284(3–4), 306–316. https://doi.org/10.1016/j.chemgeo.2011.03.010.

Sugitani, K., Mimura, K., Takeuchi, M., Yamaguchi, T., Suzuki, K., Senda, R., Asahara, Y., Wallis, S., & Van Kranendonk, M. J., 2015. A Paleoarchean coastal hydrothermal field inhabited by diverse microbial communities: The Strelley Pool Formation, Pilbara Craton, Western Australia. Geobiology, 13(6), 522–545. https://doi.org/10.1111/gbi.12150.

Sverjensky, D. A., 1984. Europium redox equilibria in aqueous solution. Earth and Planetary Science Letters, 67(1), 70–78. https://doi.org/10.1016/0012-821X(84)90039-6.

Swart, P. K., 2015. The geochemistry of carbonate diagenesis: The past, present and future. Sedimentology, 62(5), 1233–1304. https://doi.org/10.1111/sed.12205.

Tadbiri, S., & Van Kranendonk, M. J., 2020. Structural analysis of syn-depositional hydrothermal veins of the 3.48 Ga Dresser Formation, Pilbara Craton, Australia. Precambrian Research, 347, 105844. https://doi.org/10.1016/j.precamres.2020.105844.

Tan, F. C., 1988. Stable carbon isotopes in dissolved inorganic carbon in marine and estuarine environments. In: Fritz, P., Fontes, J.C. (Eds.), Handbook of Enviromental Isotope Geochemistry. Elsevier, Amsterdam, vol. 3, pp. 171-190.

Tan, F. C., & Hudson, J. D., 1971. Carbon and oxygen isotopic relationships of dolomites and co-existing calcites, Great Estuarine Series, Jurassic), Scotland. Geochimica et Cosmochimica Acta, 35(8), 755–767. https://doi.org/10.1016/0016-7037(71)90124-4.

Tao, C., Seyfried, W. E., Lowell, R. P., Liu, Y., Liang, J., Guo, Z., Ding, K., Zhang, H., Liu, J., Qiu, L., Egorov, I., Liao, S., Zhao, M., Zhou, J., Deng, X., Li, H., Wang, H., Cai, W., Zhang, G., Zhou, H., Lin, J. & Li, W., 2020. Deep high-temperature hydrothermal circulation in a detachment faulting system on the ultra-slow spreading ridge. Nature Communications, 11(1), 1300. https://doi.org/10.1038/s41467-020-15062-w.

Taylor, S. R., McLennan, S. M., 1985. The Continental Crust: Its Composition and Evolution. Blackwell Scientific Publications, Oxford), 312pp.

Thorpe, R. I., Hickman, A. H., Davis, D. W., Mortensen, J. K., & Trendall, A. F., 1992. U-Pb zircon geochronology of Archaean felsic units in the Marble Bar region, Pilbara Craton, Western Australia. Precambrian Research, 56(3), 169–189. https://doi.org/10.1016/0301-9268(92)90100-3.

Toyama, K., & Terakado, Y., 2019. Estimation of the practical partition coefficients of rare earth elements between limestone and seawater: Discussion and application. Geochemical Journal, 53(2), 139–150. https://doi.org/10.2343/geochemj.2.0550.

Tusch, J., Münker, C., Hasenstab, E., Jansen, M., Marien, C. S., Kurzweil, F., Van Kranendonk, M. J., Smithies, H., Maier, W., & Garbe-Schönberg, D., 2021. Convective isolation of Hadean mantle reservoirs through Archean time. Proceedings of the National Academy of Sciences, 118(2), e2012626118. https://doi.org/10.1073/pnas.2012626118.

Tympel, J. F., Hergt, J. M., Maas, R., Woodhead, J. D., Greig, A., Bolhar, R., & Powell, R., 2021. Mantle-like Hf-Nd isotope signatures in ~3.5 Ga greenstones: No evidence for Hadean crust beneath the East Pilbara Craton. Chemical Geology, 576, 120273. https://doi.org/10.1016/j.chemgeo.2021.120273.

Ueno, Y., Isozaki, Y., Yurimoto, H., Maruyama, S., 2001. Early Archean (ca. 3.5 Ga) microfossils and 13C-depleted carbonaceous matter in the North Pole area, Western Australia: Field occurrence and geochemistry. In Nakashima, S., Maruyama, S., Brack, A., Windley, B.F. (eds), Geochemistry and the Origin of Life. Tokyo: Universal Academy Press, pp.203-236. http://www.geo.titech.ac.jp/lab/ueno/pdf/Ueno01b.pdf.

Van Den Boorn, S. H. J. M., Van Bergen, M. J., Nijman, W., & Vroon, P. Z., 2007. Dual role of seawater and hydrothermal fluids in Early Archean chert formation: Evidence from silicon isotopes. Geology, 35(10), 939. https://doi.org/10.1130/G24096A.1.

Van Kranendonk, M., 2006. Volcanic degassing, hydrothermal circulation and the flourishing of early life on Earth: A review of the evidence from c. 3490-3240 Ma rocks of the Pilbara Supergroup, Pilbara Craton, Western Australia. Earth-Science Reviews, 74(3–4), 197–240. https://doi.org/10.1016/j.earscirev.2005.09.005.

Van Kranendonk, M. J., 2007. Chapter 7.2 A Review of the Evidence for Putative Paleoarchean Life in the Pilbara Craton, Western Australia. In Developments in Precambrian Geology, Elsevier, Vol. 15, pp. 855–877. https://doi.org/10.1016/S0166-2635(07)15072-6.

Van Kranendonk, M. J., & Pirajno, F., 2004. Geochemistry of metabasalts and hydrothermal alteration zones associated with c. 3.45 Ga chert and barite deposits: Implications for the geological setting of the Warrawoona Group, Pilbara Craton, Australia. Geochemistry: Exploration, Environment, Analysis, 4(3), 253–278. https://doi.org/10.1144/1467-7873/04-205.

Van Kranendonk, M. J., & Hickman, A. H., 2000. Archaean Geology of the North Shaw Region, East Pilbara Granite-Greenstone Terrane, Western Australia: A Field Guide. Department of Minerals and Energy.

Van Kranendonk, M. J., Hickman, A. H., Smithies, R. H., Nelson, D. R., & Pike, G., 2002. Geology and Tectonic Evolution of the Archean North Pilbara Terrain, Pilbara Craton, Western Australia. Economic Geology, 97(4), 695–732. https://doi.org/10.2113/gsecongeo.97.4.695.

Van Kranendonk, M. J., Webb, G. E., & Kamber, B. S., 2003. Geological and trace element evidence for a marine sedimentary environment of deposition and biogenicity of 3.45 Ga stromatolitic carbonates in the Pilbara Craton, and support for a reducing Archaean ocean. Geobiology, 1(2), 91–108. https://doi.org/10.1046/j.1472-4669.2003.00014.x.

Van Kranendonk, M. J., Hickman, A. H., Smithies, R. H., Williams, I. R., Bagas, L., 2006a. Revised Lithostratigraphy of Archean Supracrustal and Intrusive Rocks in the Northern Pilbara Craton, Western Australia. Western Australia Geological Survey. Record 2006/15, 57 p.

Van Kranendonk, M. J., Hickman, A. H., Huston, D. L., 2006b. Geology and Mineralization of the East Pilbara d A Field Guide. Western Australia Geological Survey. Record 2006/16, 94 p.

Van Kranendonk, M. J., Philippot, P., Lepot, K., Bodorkos, S., & Pirajno, F., 2008. Geological setting of Earth's oldest fossils in the ca. 3.5 Ga Dresser Formation, Pilbara Craton, Western Australia. Precambrian Research, 167(1), 93–124. https://doi.org/10.1016/j.precamres.2008.07.003.

Van Kranendonk, M. J., Hugh Smithies, R., Griffin, W. L., Huston, D. L., Hickman, A. H., Champion, D. C., Anhaeusser, C. R., & Pirajno, F., 2015. Making it thick: A volcanic plateau origin of Palaeoarchean continental lithosphere of the Pilbara and Kaapvaal cratons. Geological Society Special Publication, 389(1), 83–111. https://doi.org/10.1144/SP389.12.

Van Kranendonk, M. J., Smithies, R. H., Champion, D. C., 2019. Paleoarchean Development of a Continental Nucleus: The East Pilbara Terrane of the Pilbara Craton, Western Australia. In: Van Kranendonk, M.J., Bennett, V.C., Hoffmann, J.E. (Eds.), Earth's Oldest Rocks. Elsevier, pp. 437–462.

Veizer, J., 1983. Chapter 3 Chemical Diagenesis of Carbonates: Theory and Application of Trace Element Technique. In Arthur, M. A., Anderson, T. F., Kaplan, I. R., Veizer, J. & Land, L. S. (Eds), Stable Isotopes in Sedimentary Geology. SEPM Society for Sedimentary Geology, 10, pp.1-100. https://doi.org/10.2110/scn.83.01.0000.

Veizer, J., 1989. Strontium Isotopes in Seawater through Time. Annual Review of Earth and Planetary Sciences, 17, 141–167. https://doi.org/10.1146/annurev.ea.17.050189.001041.

Veizer, J., & Compston, W., 1974. $^{87}Sr/^{86}Sr$ composition of seawater during the Phanerozoic. Geochimica et Cosmochimica Acta, 38(9), 1461–1484. https://doi.org/10.1016/0016-7037(74)90099-4.

Veizer, J., Ala, D., Azmy, K., Bruckschen, P., Buhl, D., Bruhn, F., Carden, G. A. F., Diener, A., Ebneth, S., Godderis, Y., Jasper, T., Korte, C., Pawellek, F., Podlaha, O. G., & Strauss, H., 1999. $^{87}Sr/^{86}Sr$, $\delta^{13}C$ and $\delta^{18}O$ evolution of Phanerozoic seawater. Chemical Geology, 161(1), 59–88. https://doi.org/10.1016/S0009-2541(99)00081-9.

Veizer, J., Clayton, R. N., & Hinton, R. W., 1992. Geochemistry of precambrian carbonates: IV. Early paleoproterozoic (2.25 ± 0.25 ga) seawater. Geochimica et Cosmochimica Acta, 56(3), 875–885. https://doi.org/10.1016/0016-7037(92)90033-F.

Veizer, J., Compston, W., Hoefs, J., & Nielsen, H., 1982. Mantle buffering of the early oceans. Naturwissenschaften, 69(4), 173–180. https://doi.org/10.1007/BF00364890.

Veizer, J., Hoefs, J., Ridler, R. H., Jensen, L. S., & Lowe, D. R., 1989. Geochemistry of Precambrian carbonates: I. Archean hydrothermal systems. Geochimica et Cosmochimica Acta, 53(4), 845–857. https://doi.org/10.1016/0016-7037(89)90030-6.

Viehmann, S., Reitner, J., Tepe, N., Hohl, S. V., Van Kranendonk, M., Hofmann, T., Koeberl, C., & Meister, P., 2020. Carbonates and cherts as archives of seawater chemistry and habitability on a carbonate platform 3.35 Ga ago: Insights from Sm/Nd dating and trace element analysis from the Strelley Pool Formation, Western Australia. Precambrian Research, 344, 105742. https://doi.org/10.1016/j.precamres.2020.105742.

Voigt, M., Pearce, C. R., Baldermann, A., & Oelkers, E. H., 2018. Stable and radiogenic strontium isotope fractionation during hydrothermal seawater-basalt interaction. Geochimica et Cosmochimica Acta, 240, 131–151. https://doi.org/10.1016/j.gca.2018.08.018.

Walter, M. R., Buick, R., & Dunlop, J. S. R., 1980. Stromatolites 3,400–3,500 Myr old from the North Pole area, Western Australia. Nature, 284(5755), 443–445. https://doi.org/10.1038/284443a0.

Webb, G. E., & Kamber, B. S., 2000. Rare earth elements in Holocene reefal microbialites: A new shallow seawater proxy. Geochimica et Cosmochimica Acta, 64(9), 1557–1565. https://doi.org/10.1016/S0016-7037(99)00400-7.

Wei, G.-Y., Hood, A. v. S., Chen, X., Li, D., Wei, W., Wen, B., Gong, Z., Yang, T., Zhang, Z.-F., & Ling, H.-F., 2019. Ca and Sr isotope constraints on the formation of the Marinoan cap dolostones. Earth and Planetary Science Letters, 511, 202–212. https://doi.org/10.1016/j.epsl.2019.01.024.

Westall, F., Campbell, K. A., Bréhéret, J. G., Foucher, F., Gautret, P., Hubert, A., Sorieul, S., Grassineau, N., & Guido, D. M., 2015. Archean (3.33 Ga) microbe-sediment systems were diverse and flourished in a hydrothermal context. Geology, 43(7), 615–618. https://doi.org/10.1130/G36646.1.

Wheat, C. G., Fisher, A. T., McManus, J., Hulme, S. M., & Orcutt, B. N., 2017. Cool seafloor hydrothermal springs reveal global geochemical fluxes. Earth and Planetary Science Letters, 476, 179–188. https://doi.org/10.1016/j.epsl.2017.07.049.

Willbold, M., & Jochum, K. P., 2005. Multi-Element Isotope Dilution Sector Field ICP-MS: A Precise Technique for the Analysis of Geological Materials and its Application to Geological Reference Materials. Geostandards and Geoanalytical Research, 29(1), 63–82. https://doi.org/10.1111/j.1751-908X.2005.tb00656.x.

Witt, W. K., 1988. Evolution of high-temperature hydrothermal fluids associated with greisenization and feldspathic alteration of a tin-mineralized granite, northeast Queensland. Economic Geology, 83(2), 310–334. https://doi.org/10.2113/gsecongeo.83.2.310.

Witt, W. K., Roberts, M. P., Hagemann, S. G., & Fisher, C., 2024. Fertile, alkalic intrusions, Karari–Whirling Dervish gold deposit, Yilgarn Craton, Western Australia. Australian Journal of Earth Sciences, 71(4), 553–584. https://doi.org/10.1080/08120099.2024.2318639.

Xiang, W., 2023. Carbonate factories in the early Archean and their geobiological impacts [Ph.D. thesis, University of Göttingen]. https://doi.org/10.53846/goediss-10047.

Xiang, W., Duda, J.-P., Pack, A., Van Zuilen, M., & Reitner, J., 2024. Were early Archean carbonate factories major carbon sinks on the juvenile Earth? Biogeosciences, 21(24), 5653–5684. https://doi.org/10.5194/bg-21-5653-2024.

Xiong, D.-Y., Wang, X.-L., Li, W., Zheng, Y.-F., Anhaeusser, C. R., Hofmann, A., Wang, D., & Li, J.-Y., 2025. Potassium Isotope Evidence for Origin of Archean TTG Rocks from Seawater-Hydrothermally Altered Oceanic Crust. Geochemistry, Geophysics, Geosystems, 26(1), e2024GC011892. https://doi.org/10.1029/2024GC011892.

Xiong, W., Wells, R. K., Horner, J. A., Schaef, H. T., Skemer, P. A., & Giammar, D. E., 2018. CO_2 Mineral Sequestration in Naturally Porous Basalt. Environmental Science & Technology Letters, 5(3), 142–147. https://doi.org/10.1021/acs.estlett.8b00047.

Yamamoto, K., Itoh, N., Matsumoto, T., Tanaka, T., & Adachi, M., 2004. Geochemistry of Precambrian carbonate intercalated in pillows and its host basalt: Implications for the REE composition of circa

3.4 Ga seawater. Precambrian Research, 135(4), 331–344. https://doi.org/10.1016/j.precamres.2004.09.006.

Yarmohammadi, S., Wood, D. A., & Kadkhodaie, A., 2020. Reservoir microfacies analysis exploiting microscopic image processing and classification algorithms applied to carbonate and sandstone reservoirs. Marine and Petroleum Geology, 121, 104609. https://doi.org/10.1016/j.marpetgeo.2020.104609.

Yoshida, S., Ueda, H., Asanuma, H., & Sawaki, Y., 2024. Y-Ho fractionation during basalt alteration in hydrothermal system: An implication for superchondritic Y/Ho signature recorded in Precambrian banded iron formations. Chemical Geology, 670, 122421. https://doi.org/10.1016/j.chemgeo.2024.122421.

Zachos, J., Pagani, M., Sloan, L., Thomas, E., & Billups, K., 2001. Trends, Rhythms, and Aberrations in Global Climate 65 Ma to Present. Science, 292(5517), 686–693. https://doi.org/10.1126/science.1059412.

Zeebe, R. E., & Wolf-Gladrow, D., 2001. CO_2 in Seawater: Equilibrium, Kinetics, Isotopes, first ed., Vol. 65. Elsevier Science. https://shop.elsevier.com/books/co2-in-seawater-equilibrium-kinetics-isotopes/zeebe/978-0-444-50946-8.

Zepeda, V. K., Flannery, D. T., & Kamber, B. S., 2023. Pb isotopes reveal intracrustal exhalative hydrothermalism during deposition of the ~3.43 Ga Strelley Pool Formation. Chemical Geology, 629, 121472. https://doi.org/10.1016/j.chemgeo.2023.121472.

Zhang, J., Amakawa, H., & Nozaki, Y., 1994. The comparative behaviors of yttrium and lanthanides in the seawater of the North Pacific. Geophysical Research Letters, 21(24), 2677–2680. https://doi.org/10.1029/94GL02404.

Zhao, Y., Wei, W., Li, S., Yang, T., Zhang, R., Somerville, I., Santosh, M., Wei, H., Wu, J., Yang, J., Chen, W., & Tang, Z., 2021. Rare earth element geochemistry of carbonates as a proxy for deep-time environmental reconstruction. Palaeogeography, Palaeoclimatology, Palaeoecology, 574, 110443. https://doi.org/10.1016/j.palaeo.2021.110443.

Zhao, Y., Wei, W., Santosh, M., Hu, J., Wei, H., Yang, J., Liu, S., Zhang, G., Yang, D., & Li, S., 2022. A review of retrieving pristine rare earth element signatures from carbonates. Palaeogeography, Palaeoclimatology, Palaeoecology, 586, 110765. https://doi.org/10.1016/j.palaeo.2021.110765.

Zhelezinskaia, I., Kaufman, A. J., Farquhar, J., & Cliff, J., 2014. Large sulfur isotope fractionations associated with Neoarchean microbial sulfate reduction. Science, 346(6210), 742–744. https://doi.org/10.1126/science.1256211.

Table 1: Geochemical compositions of the various carbonates from the East Pilbara Terrane, Western Australia

Formation	North Star Basalt		Dresser Fm.	Mt Ada Basalt			Apex Basalt						
Age (Ma)	3490		3480	3470			3460						
Lithology	Interstitial Cal.(A)	Interstitial Ank.	Interstitial Cal.(A)	Interstitial Ank.			Interstitial Cal.(P)					Interstitial Cal.(A)	
Sample ID	CP-1	CP-2	D-3	A-1-C	A-1-E	A-2	A14673-1	A22-1	A22-2	ABAS-2	ABAS-3	Apex1	Apex2
(wt%)													
Dissolved fraction(%)	96.7	99.7	71.6	98.6	82.9	92.7	92.0	93.9	91.9	75.9	96.6	75.5	82.8
Al	0.014	0.003	0.005	0.009	0.403	0.008	0.072	0.007	0.024	0.996	0.013	0.020	0.201
Ca	41.596	22.069	41.162	23.701	30.644	23.819	39.796	39.637	39.000	38.418	40.570	40.896	40.387
Fe	0.292	8.925	0.710	10.409	7.322	8.423	0.810	1.152	1.434	2.534	1.109	0.558	0.797
K	bd	bd	bd	bd	bd	bd	bd	bd	bd	bd	bd	bd	bd
Mg	0.153	8.191	0.244	6.099	4.624	7.245	0.199	0.465	0.612	0.774	0.198	0.115	0.254
Mn	0.940	0.598	1.068	0.827	0.834	0.497	0.780	0.951	0.808	0.623	0.611	0.685	0.544
Na	bd	bd	bd	bd	bd	bd	bd	bd	bd	bd	bd	bd	bd

$(\mu g/g)$													
Sc	7.351	0.464	0.393	1.297	10.695	0.408	1.487	2.430	11.437	15.749	3.426	1.188	2.664
Ti	0.284	0.243	0.117	0.259	5.346	0.000	1.317	0.200	0.488	8.088	0.925	0.530	1.498
V	1.006	1.273	2.118	62.298	55.349	7.350	3.968	2.658	3.125	55.570	3.309	1.320	7.666
Ni	nd	nd	nd	5.151	13.040	nd	8.585	5.233	5.988	32.884	5.251	7.634	13.230
Zn	nd	nd	nd	33.148	35.887	nd	3.413	1.950	6.740	19.351	1.390	1.888	4.699
Rb	0.116	0.030	0.011	0.090	0.110	0.042	0.030	0.012	0.039	0.038	0.020	0.029	0.007
Sr	74.047	26.952	78.124	159.617	216.531	202.047	108.339	100.443	112.337	141.104	133.304	120.572	115.930
Y	115.176	15.990	7.261	22.683	38.089	3.918	11.066	26.054	62.464	13.509	12.695	10.762	13.030
Zr	0.008	0.000	0.011	0.000	0.090	0.000	0.169	0.198	0.170	0.235	0.255	0.149	0.098
Mo	0.209	0.175	0.240	0.173	0.204	0.141	0.185	0.196	0.197	0.389	0.187	0.215	0.207
Ba	0.931	0.459	5.778	18.400	8.113	91.466	34.427	5.060	7.110	23.867	11.632	4.268	6.287
La	31.071	7.105	0.711	0.577	3.717	2.513	1.391	3.277	6.265	1.917	1.235	1.590	1.690
Ce	84.082	11.126	1.340	2.710	14.595	4.476	2.841	7.443	16.116	4.652	2.538	3.275	3.815
Pr	12.335	1.495	0.161	0.775	3.304	0.626	0.402	1.079	2.544	0.716	0.354	0.452	0.572

Nd	57.269	6.729	0.711	6.193	21.188	2.742	1.929	5.078	12.843	3.645	1.698	2.157	2.921
Sm	18.313	1.933	0.196	4.897	11.237	0.786	0.662	1.723	4.881	1.428	0.586	0.691	1.014
Eu	6.704	0.781	0.052	2.672	6.757	0.656	0.248	0.626	1.572	0.587	0.226	0.200	0.316
Gd	22.411	3.059	0.386	7.880	14.034	1.059	0.986	2.431	6.845	1.884	0.988	1.020	1.447
Tb	3.234	0.425	0.071	1.114	1.732	0.139	0.168	0.432	1.258	0.287	0.182	0.164	0.228
Dy	21.389	2.414	0.636	5.371	8.112	0.689	1.215	3.251	9.379	1.909	1.447	1.212	1.624
Ho	4.109	0.414	0.172	0.797	1.227	0.109	0.301	0.790	2.167	0.428	0.372	0.298	0.390
Er	11.098	1.116	0.593	1.702	2.577	0.223	0.933	2.557	6.762	1.271	1.250	0.968	1.249
Tm	1.670	0.135	0.107	0.194	0.291	0.023	0.138	0.410	1.075	0.190	0.206	0.152	0.190
Yb	9.693	0.756	0.688	1.067	1.619	0.126	0.895	2.724	7.529	1.295	1.471	1.038	1.317
Lu	1.238	0.098	0.109	0.134	0.206	0.015	0.145	0.450	1.251	0.212	0.247	0.179	0.228
Hf	nd	nd	nd	0.007	0.016	nd	0.004	0.007	0.019	0.007	0.004	0.006	0.005
Th	0.017	0.024	0.000	0.001	0.015	0.000	0.006	0.000	0.007	0.028	0.000	0.002	0.001
U	0.001	0.002	0.007	0.001	0.002	0.001	0.028	0.048	0.039	0.019	0.019	0.006	0.004
REE+Y	399.79	53.58	13.19	58.77	128.68	18.10	23.32	58.33	142.95	33.93	25.49	24.16	30.03

Y/Ho	28.03	38.61	42.33	28.47	31.05	36.00	36.72	32.98	28.82	31.60	34.17	36.07	33.43
Ce/Ce*	1.00	0.82	0.95	0.69	0.81	0.86	0.91	0.94	0.93	0.93	0.92	0.93	0.92
Pr/Pr*	0.98	0.96	0.93	0.78	0.89	0.99	0.94	0.96	0.95	0.94	0.94	0.94	0.93
La/La*	1.21	1.96	1.69	-0.13	-0.52	1.48	2.04	1.57	2.21	2.64	2.03	1.98	3.03
Gd/Gd*	1.14	1.01	1.57	0.87	0.98	0.96	1.10	1.12	1.07	1.09	1.20	1.19	1.15
Eu/Eu*	1.87	1.92	1.07	2.56	3.21	4.26	1.70	1.65	1.45	2.01	1.63	1.34	1.47
Y/Y*	0.18	2.51	5.17	1.21	0.87	11.68	2.85	0.93	0.31	1.80	1.98	2.70	1.94
Pr_{SN}/Yb_{SN}	0.38	0.59	0.07	0.22	0.61	1.48	0.13	0.12	0.10	0.16	0.07	0.13	0.13
Sm_{SN}/Yb_{SN}	0.83	1.12	0.12	2.01	3.04	2.74	0.32	0.28	0.28	0.48	0.17	0.29	0.34
(‰) [Ref.a]													
$\delta\ ^{13}C_{VPDB}$	-2.31	0.01	0.63	0.83	0.77	0.52	0.62	0.44	0.69	0.65	0.77	0.25	0.04
$\delta\ ^{18}O_{VPDB}$	-19.17	-14.34	-19.81	-18.14	-18.57	-16.05	-16.74	-17.29	-16.72	-16.97	-15.79	-17.58	-17.70

Formation	Apex Basalt	Euro Basalt	Euro Basalt	Euro Basalt	Dresser Fm.	Dresser Fm.	Dresser Fm.	Dresser Fm.	Dresser Fm.	Dresser Fm.	Euro Basalt	Strelley Pool Fm.
Age (Ma)	3460	3350	3350	3350	3480	3480	3490	3480	3480	3480	3350	3410
Lithology	Interstitial Cal.(A)	Interstitial Cal.(A)	Interstitial Cal.(A)	Interstitial Cal.(A)	Fracture Cal.	Fracture Cal..	Sedimentary Carb.	Sedimentary Carb.	Sedimentary Carb.	Sedimentary Carb.	Sedimentary Carb.	Stromatolite
Sample ID	Apex3	E-1	E-2	E-3	D-2-R	D-2-W	D-1	PDP	DB	TSU	E-4	Strelley
(wt%)												
Dissolved fraction(%)	86.0	90.2	92.0	32.5	99.0	99.9	30.5	81.3	16.5	27.9	63.4	76.7
Al	0.025	0.022	0.001	0.007	0.002	0.003	0.113	0.008	0.100	0.031	0.074	0.000
Ca	40.442	41.153	40.372	40.405	42.159	42.199	21.088	26.167	36.557	21.543	22.504	22.664
Fe	0.661	0.556	0.187	0.093	0.000	0.068	12.098	9.623	0.156	10.008	7.339	1.671
K	bd	bd	bd	bd	bd	bd	bd	bd	bd	bd	bd	bd
Mg	0.162	0.129	0.091	0.090	0.000	0.177	6.470	9.884	2.255	7.323	9.339	11.986
Mn	0.732	0.508	0.757	0.817	0.000	0.007	0.965	1.331	0.200	1.060	0.962	0.440
Na	bd	bd	bd	bd	bd	bd	bd	bd	bd	bd	bd	bd

$(\mu g/g)$												
Sc	1.200	2.391	14.310	1.002	0.266	0.236	9.557	4.768	46.775	7.298	11.821	1.813
Ti	0.565	0.405	0.000	0.369	0.102	0.034	8.776	0.134	5.300	2.403	7.548	1.429
V	1.574	1.716	0.856	1.013	0.178	0.194	36.445	5.201	5.481	19.733	51.124	2.169
Ni	7.404	6.204	5.833	nd	nd	nd	nd	nd	nd	nd	167.581	nd
Zn	1.433	0.000	0.000	nd	nd	nd	nd	nd	nd	nd	30.683	nd
Rb	0.046	0.011	0.013	0.033	0.012	0.009	1.018	0.019	1.379	0.435	0.514	0.060
Sr	112.434	100.155	67.115	46.766	1198.471	1789.259	46.869	127.956	66.446	37.982	21.624	47.821
Y	15.885	15.600	32.563	18.240	1.116	1.363	14.653	26.309	23.191	10.961	12.443	2.133
Zr	0.136	0.073	0.004	0.003	0.000	0.000	0.332	0.095	0.865	1.154	1.052	0.936
Mo	0.223	0.134	0.154	0.306	0.026	0.012	0.456	0.301	0.100	0.238	1.832	0.103
Ba	6.425	7.887	4.430	3.005	112.364	1.456	33.261	132.848	4594.744	110.834	5.418	55.556
La	2.248	1.994	5.661	2.100	0.121	0.083	1.863	2.410	2.175	1.257	3.673	0.274
Ce	4.392	4.039	13.882	3.386	0.236	0.120	4.716	4.654	1.517	3.206	9.950	0.439
Pr	0.602	0.562	2.011	0.441	0.034	0.016	0.784	0.709	0.658	0.517	1.579	0.069

Nd	2.863	2.715	9.406	2.142	0.166	0.072	4.059	3.555	3.282	2.710	7.183	0.360
Sm	0.920	0.861	3.246	0.727	0.061	0.027	1.829	1.627	1.316	1.180	2.101	0.166
Eu	0.266	0.339	1.547	0.288	0.020	0.008	0.737	1.035	0.985	0.461	0.798	0.088
Gd	1.432	1.365	4.678	1.488	0.125	0.078	2.712	2.629	2.354	1.610	2.746	0.302
Tb	0.231	0.223	0.781	0.251	0.021	0.015	0.417	0.463	0.432	0.261	0.409	0.046
Dy	1.674	1.634	5.297	2.090	0.168	0.151	2.484	3.305	3.486	1.665	2.276	0.253
Ho	0.410	0.400	1.114	0.519	0.037	0.037	0.499	0.745	0.768	0.348	0.408	0.046
Er	1.298	1.247	3.065	1.696	0.103	0.122	1.339	2.242	2.313	1.029	0.977	0.118
Tm	0.203	0.183	0.435	0.284	0.014	0.019	0.180	0.328	0.383	0.156	0.115	0.016
Yb	1.299	1.153	2.850	1.834	0.076	0.111	1.144	2.151	2.411	1.075	0.651	0.101
Lu	0.219	0.188	0.446	0.300	0.010	0.015	0.170	0.317	0.341	0.167	0.091	0.016
Hf	0.005	0.004	0.012	nd	nd	nd	nd	nd	nd	nd	0.039	nd
Th	0.000	0.001	0.010	0.000	0.000	0.000	0.340	0.002	0.013	0.174	0.161	0.015
U	0.012	0.016	0.009	0.005	0.002	0.001	0.096	0.005	0.413	0.036	0.016	0.027
REE+Y	33.95	32.50	86.98	35.79	2.31	2.24	37.59	52.48	45.61	26.60	45.40	4.43

Y/Ho	38.74	38.96	29.24	35.17	30.48	36.57	29.35	35.33	30.19	31.50	30.52	46.50
Ce/Ce*	0.91	0.91	0.97	0.85	0.88	0.79	0.90	0.85	0.30	0.92	0.95	0.77
Pr/Pr*	0.94	0.94	0.97	0.91	0.94	0.95	0.95	0.94	1.23	0.93	1.02	0.94
La/La*	2.05	2.16	1.41	3.02	2.29	2.24	2.93	2.82	2.64	3.76	1.01	5.00
Gd/Gd*	1.16	1.16	1.02	1.44	1.33	2.06	0.96	1.04	1.23	0.98	0.93	0.91
Eu/Eu*	1.32	1.77	2.20	1.62	1.32	1.05	1.89	2.77	3.11	1.85	1.88	2.32
Y/Y*	2.16	2.26	0.69	1.50	21.34	21.64	1.59	1.14	0.95	2.22	2.26	28.49
Pr_{SN}/Yb_{SN}	0.14	0.14	0.21	0.07	0.13	0.04	0.20	0.10	0.08	0.14	0.72	0.20
Sm_{SN}/Yb_{SN}	0.31	0.33	0.50	0.17	0.35	0.11	0.70	0.33	0.24	0.48	1.41	0.72
(‰) [Ref.a]												
$\delta\ ^{13}C_{VPDB}$	0.21	0.21	0.99	-2.37	2.34	2.20	0.97	1.26	-5.10	1.46	1.88	2.50
$\delta\ ^{18}O_{VPDB}$	-17.37	-19.23	-19.52	-19.31	-17.81	-13.03	-15.95	-12.69	-7.88	-14.66	-15.19	-13.16

Note:

1. Anomalies were calculated based on PAAS-normalized values (after Pourmand et al., 2012):

$Ce/Ce^* = Ce_{SN}/(0.5Pr_{SN} + 0.5La_{SN})$ and $Pr/Pr^* = Pr_{SN}/(0.5Ce_{SN} + 0.5Nd_{SN})$ (after Bau and Dulski, 1996)

$La/La^* = La_{SN}/(3Pr_{SN} – 2Nd_{SN})$ and $Gd/Gd^* = Gd_{SN}/(2Tb_{SN} - Dy_{SN})$ (after Alexander et al., 2008)

$Eu/Eu^* = Eu_{SN}/(Sm_{SN}^2 * Tb_{SN})^{1/3}$ and $Y/Y^* = Y_{SN}/(0.5Er_{SN} \times 0.5Ho_{SN})$ (after Lawrence et al. 2006)

2. bd: below the limits of detection; nd: not determined

3. Stable carbon and oxygen isotopes are from Ref. a (Xiang et al., 2024).

4. Abbreviations: Cal. –calcite; P-primary; A-altered; Ank. - dolomite; Carb. -carbonate; Fm. -Formation; SPF- Strelley Pool Formation.

Table 2: The age-corrected radiogenic Sr isotopic compositions of the EPT carbonates.

Lithology	Formation	Age (Ma)	SampleID	Sr (μg/g)	Rb (μg/g)	$^{87}Rb/^{86}Sr$	$^{87}Sr/^{86}Sr$	2sigma (2σ)	N	$^{87}Sr/^{86}Sr$ (i)
Interstitial Cal.(P)	Apex Basalt	3460	A14673-1	93.89	0.03	0.0009	0.703205	0.000004	95	0.703159
			A22-2	103.2	0.03	0.0007	0.704209	0.000004	96	0.704172
			ABAS-2	127.9	0.04	0.0008	0.703291	0.000005	92	0.703250
			ABAS-3	119.7	0.02	0.0005	0.701822	0.000004	96	0.701796
Interstitial Cal.(A)	Euro Basalt	3350	E-1	98.21	0.01	0.0002	0.706552	0.000004	98	0.706543
			E-3	34.91	0.02	0.0016	0.706605	0.000005	95	0.706540
	Apex Basalt	3460	Apex1	112.02	0.03	0.0008	0.704684	0.000005	95	0.704657
			Apex2	105.78	0.01	0.0003	0.703327	0.000006	97	0.703326
			Apex3	102.38	0.02	0.0007	0.703687	0.000005	97	0.703664
	Dresser Fm.	3480	D-3	71.57	0.01	0.0003	0.701919	0.000005	94	0.701917
	North Star Basalt	3490	CP-1	62.72	0.08	0.0038	0.703678	0.000004	97	0.703496
Interstitial Ank.	Mt Ada Basalt	3470	A-1-C	116.99	0.07	0.0017	0.707917	0.000004	97	0.707833
			A-1-E	160.05	0.09	0.0016	0.708825	0.000004	97	0.708746
			A-2	165.2	0.03	0.0005	0.712846	0.000005	98	0.712832
	North Star Basalt	3490	CP-2	20.02	0.02	0.0025	0.705454	0.000004	93	0.705341
Fracture Carb.	Dresser Fm.	3480	D-2-R	1089.56	0	0	0.700666	0.000005	96	0.700678
			D-2-W	1754.68	0	0	0.700583	0.000005	96	0.700596
Sedimentary. Carb.	Euro Basalt	3350	E-4	14.81	0.36	0.0706	0.714446	0.000006	99	0.711009
	Dresser Fm.	3480	D-1	33.11	0.72	0.0632	0.71216	0.000005	98	0.708969
			DB	61.34	1.09	0.0516	0.718059	0.000005	96	0.715458
			TSU	30.79	0.36	0.0337	0.70985	0.000004	96	0.708153
			PDP	103.96	0.01	0.0003	0.702207	0.000005	97	0.702203

SPF Stromatolite	Strelley Pool Fm.	3410	Strelley	40.05	0.05	0.0035	0.705377	0.000005	96	0.705217

Note:

1. $^{86}Sr/^{88}Sr$ ratio was normalized to 0.1194 using an exponential law.
2. $^{86}Sr/^{87}Sr$ ratio of NIST SRM 987 is 0.710246 ± 0.000009 (2σ, n =48).
3. $^{86}Sr/^{87}Sr$ ratios of JDo-1 and JLs-1 are 0.707575±28 (2σ, n=2) and 0.707847±19 (2σ, n=2), respectively.
4. $^{86}Sr/^{87}Sr$ (i) are $^{86}Sr/^{87}Sr$ ratios after correction of Rb and age.
5. Abbreviations: Cal. –calcite; P-primary; A-altered; Ank. - ankerite; Carb. –carbonate; SPF- Strelley Pool Formation; Fm. – formation.

Table 3: Temperatures calculated with the $\delta^{18}O_{PDB}$ values (‰) of the seawater endmember (D-2-W) and primary interstitial calcites, and various seawater $\delta^{18}O_{SMOW}$ values (‰).

SampleID	Lithology	Formation	Age (Ma)	Calcite $\delta^{18}O$ (PDB, ‰)	Temperature (°C) calculated via seawater $\delta^{18}O$ (‰)					
					-13.3 [a]	-8 [b]	-5 [c]	-1.2 [d]	0 [e]	3.3 [f]
A14673-1	Primary interstitial calcite	Apex Basalt	3460	-16.74	33.2	62.8	82.1	109.1	118.3	144.9
A22-1				-17.29	35.9	66.2	85.8	113.2	122.5	149.4
A22-2				-16.72	33.0	62.7	81.9	108.9	118.1	144.6
ABAS-2				-16.97	34.3	64.3	83.7	110.9	120.0	146.8
ABAS-3				-15.79	28.4	57.1	75.8	102.1	111.0	137.0
D-2-W	Seawater calcite	Dresser Formation	3480	-13.03	15.7	41.5	58.5	82.7	91.0	115.1

Note:

1. The paleotemperatures are calculated via equation (Shackleton & Kennett, 1975):

$$T(°C) = 16.9 - 4.38\,(\delta^{18}O_{CaCO3} - \delta^{18}O_w) + 0.1\,(\delta^{18}O_{CaCO3} - \delta^{18}O_w)^2$$

2. References: a. Jaffrés et al., 2007; b. Kutyrev et al., 2024; c. Herwartz et al., 2021; d. Shackleton & Kennett, 1975; e. Hoefs, 2018; f. Johnson and Wing, 2020.

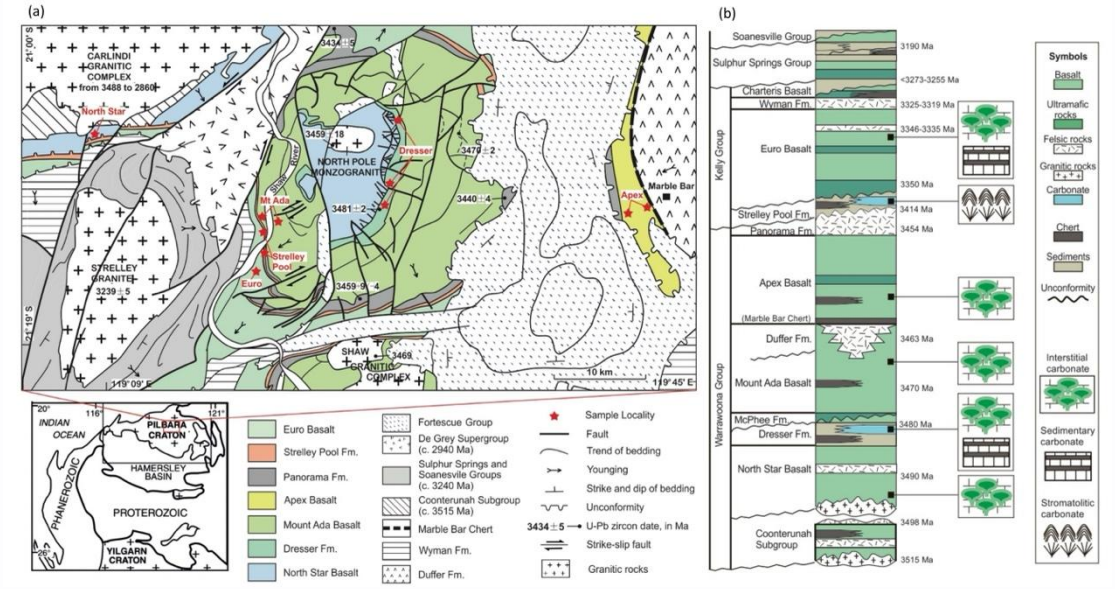

Figure 1: (a) Simplified geological map of the North Pole Dome, Eastern Pilbara Terrane, Western Australia, including sampling localities (red stars). (b) Simplified stratigraphy of the studied Archean rocks (Xiang et al., 2024; modified from Van Kranendonk and Hickman, 2000; Van Kranendonk et al., 2007b; Hickman and Van Kranendonk, 2012).

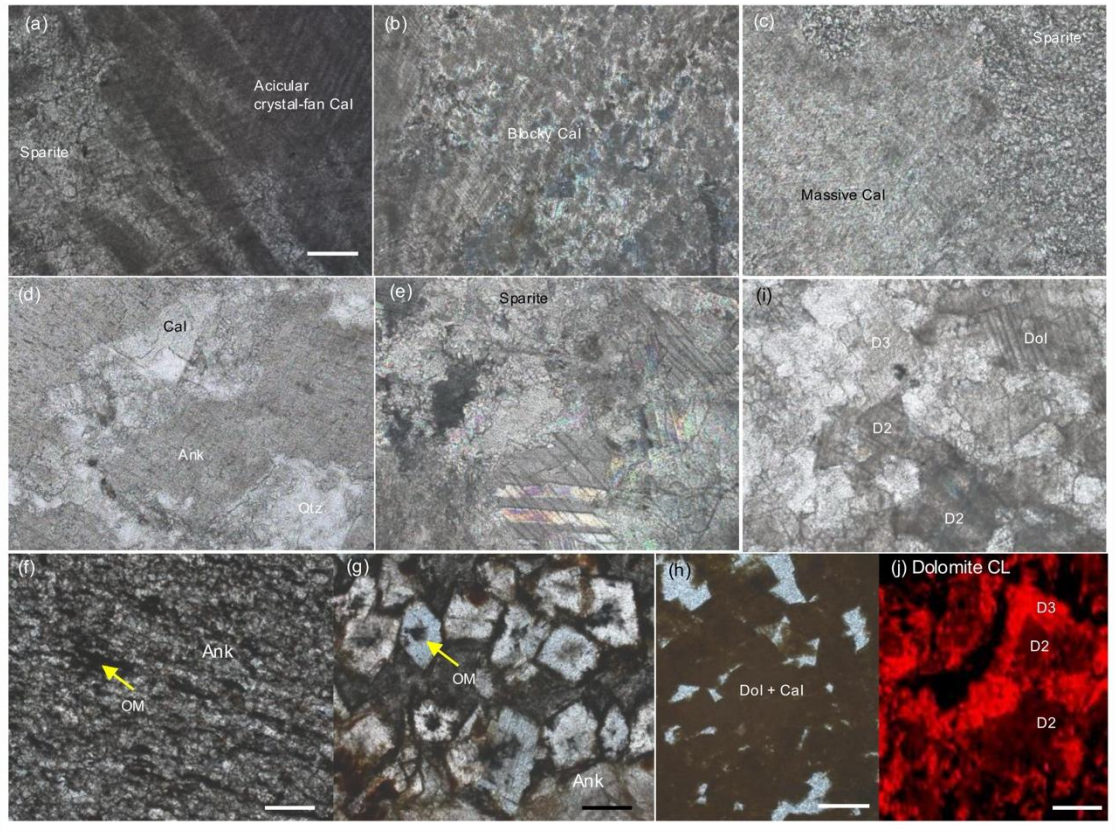

Figure 2: Thin-section photomicrographs from the North Pole Dome, Eastern Pilbara Terrane (Western Australia). The samples reveal four distinct types of interstitial carbonates: (1) primary facies: the acicular crystal-fan calcite (a); (2) recrystallized/altered facies: blocky calcite (b) and

massive calcite and sparry calcite (sparite) in (c); (3) The blocky ankerites often exhibiting the calcite overgrowth; (4) Fracture-filling calcite precipitated in wide fractures. Sedimentary carbonates include two types, namely marine ankerite associated with organic matter (f, g) and terrestrial hydrothermal dolomite-calcite assemblages (h). (I, j) show stromatolite from the Strelley Pool Formation displays tri-generational dolomite, with initial generation (D1) partially recrystallized into subsequent generations (D2-D3). Samples (a-c) derive from the Apex Basalt, (d) from Mt Ada Basalt, and (e, f-h) from the Dresser Formation. All photographs were taken under plane-polarized light except (b, c) under cross-polarized light and (j) under Cathodoluminescence. Scale bars in (a, f-h) are 200 µm (also applies to b-e, i), whereas the scale bar in (j) is 25 µm. (Mineral abbreviation: Cal-calcite, Qtz- quartz, Ank-ankerite, Dol-dolomite).

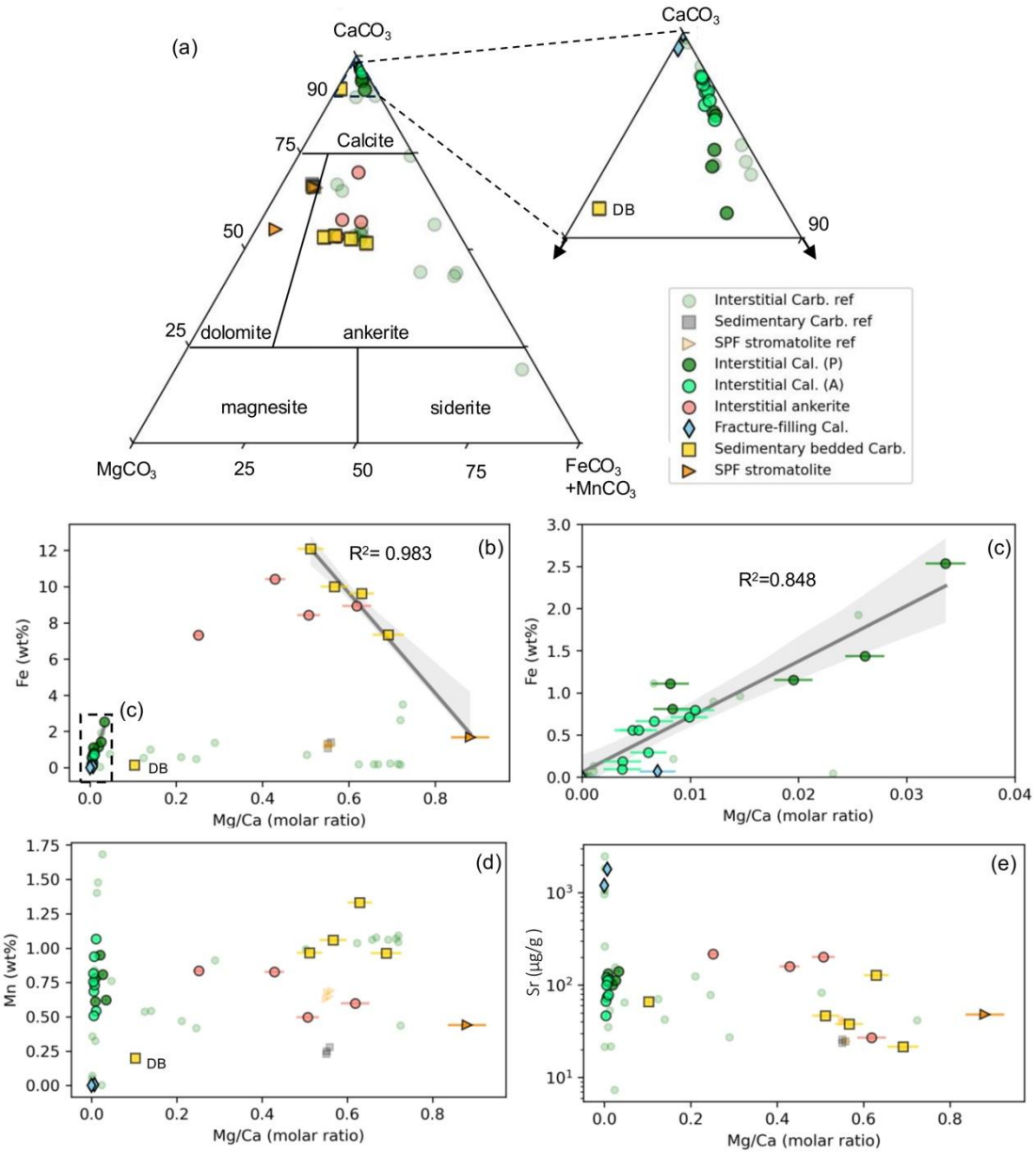

Figure 3: (a) Carbonate rock classification based on converted $CaCO_3$-$MgCO_3$-$(Fe+Mn)CO_3$ compositions (wt%). It reveals that the EPT carbonates mainly comprise calcite, dolomite, and

ankerite. Cross-plots of EPT carbonates display molar Mg/Ca ratio vs. (b, c) Fe (wt%), (d) Mn (wt%), and (e) Sr (µg/g), revealing varied Fe, Mn, and Sr levels across carbonate facies. The dashed square in (b) is enlarged in (c), with grey lines and envelope indicating strong Fe-lithology correlations, suggesting dissolved Fe mainly from carbonates. Data on interstitial carbonates are sourced from Nakamura and Kato (2004), Yamamoto et al. (2004), and Marien et al. (2023), while sedimentary carbonate and stromatolite data come from Viehmann et al. (2020). (Abbreviations: Cal. –calcite; P-primary; A-altered; Carb. -carbonate; SPF- Strelley Pool Formation; ref-reference).

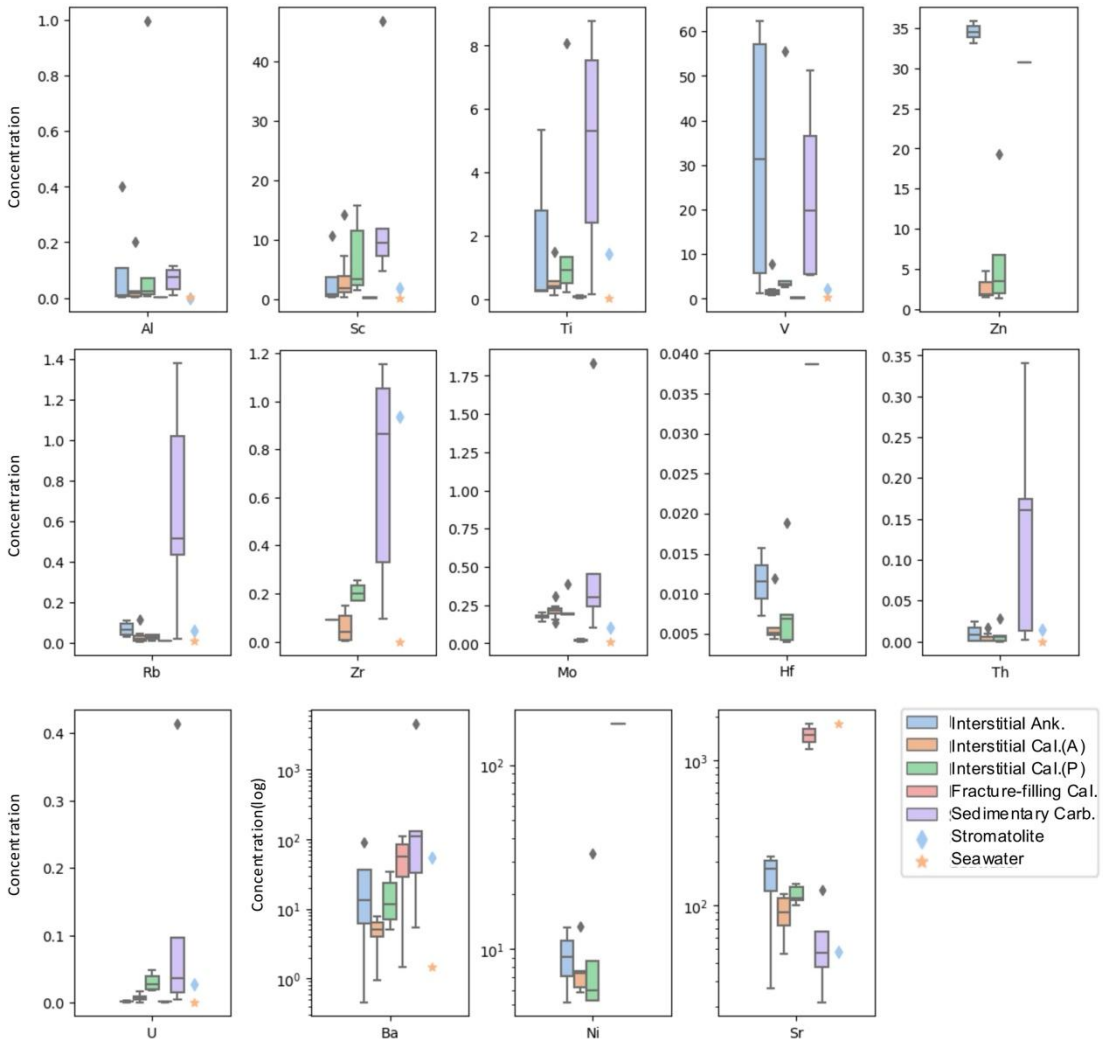

Figure 4: Plots showing trace element concentrations (Al in wt%, others in µg/g) in the EPT carbonates. The SPF stromatolite and the Paleoarchean seawater endmember (D-2-W, details in Section 5.2.1) are marked by diamond and star, respectively. (Abbreviations: Cal. –calcite; P-primary; A-altered; Ank.-ankerite; Carb. -carbonate).

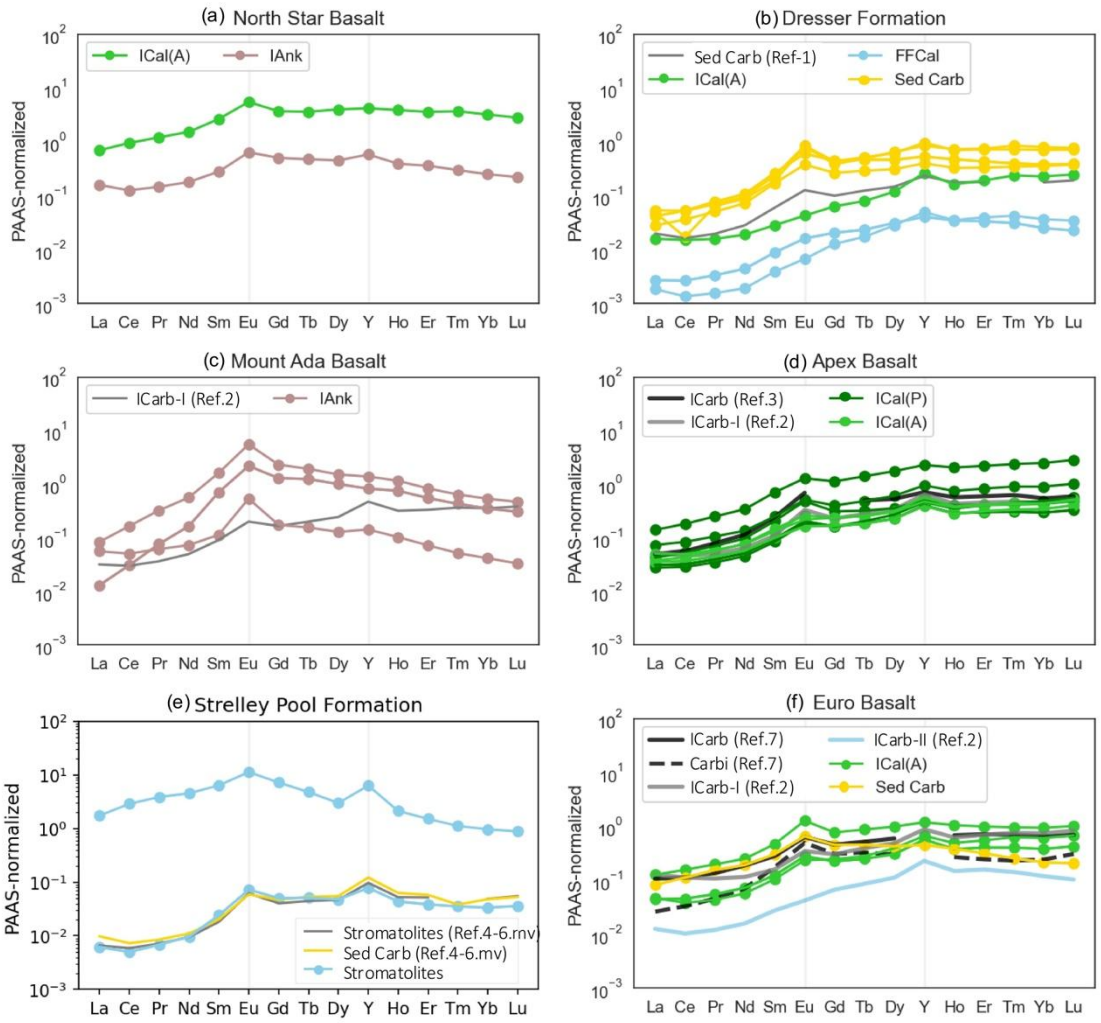

Figure 5: The PAAS-normalized REE+Y patterns of EPT carbonates and referenced counterparts, stratigraphically organized. (a) North Star Basalt, (b) Dresser Formation, (c) Mt Ada Basalt, (d) Apex Basalt, (e) Strelley Pool Formation, and (f) Euro Basalt. Abbreviations: "ICal" denotes interstitial calcite (P = primary facies, A = altered facies); "IAnk" indicates interstitial ankerite; "Sed Carb" represents sedimentary carbonate; "FFCal" refers to fracture-filling calcite. "ICal-I" and "ICal-II" are Type I and II interstitial carbonates from Ref.2; "Carbi" in (f) denotes carbonate inclusions in Euro pillow basalt margins (Ref.7). "Ref-X" indicates data from reference X, while "Ref-X.mv" represents the mean of referenced data in Figure A.1. References: Ref.1 - Van Kranendonk et al. (2003); Ref.2 - Marien et al. (2023); Ref.3 - Nakamura and Kato (2004); Refs.4-6 - Van Kranendonk et al. (2003), Allwood et al. (2010), Viehmann et al. (2020); Ref.7 - Yamamoto et al. (2004).

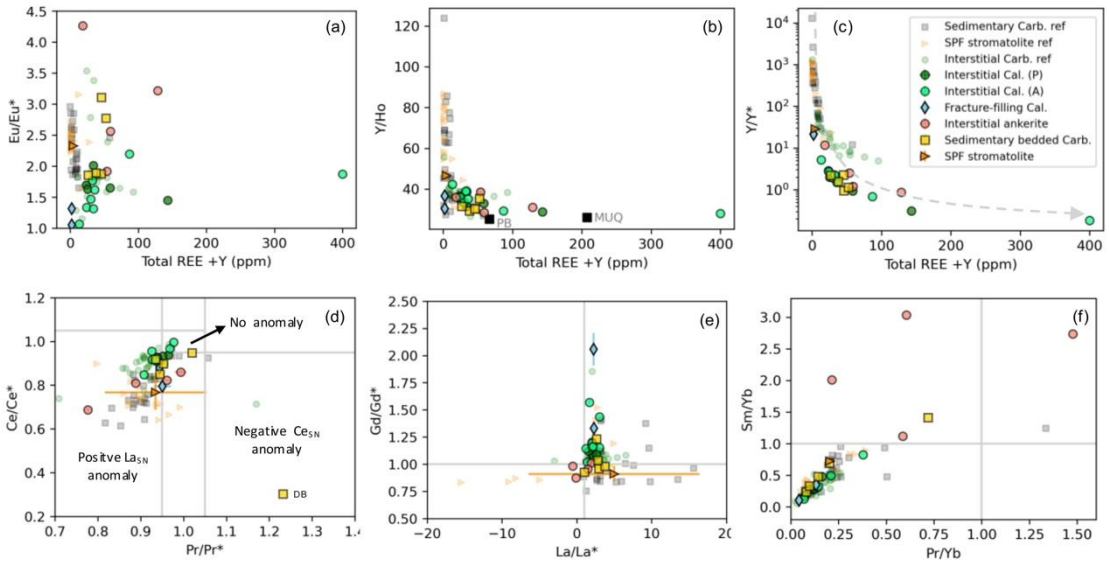

Figure 6: Plots of diagnostic REE+Y ratios and the PAAS-normalized REE+Y anomalies for EPT carbonates and references. (a) Y/Ho weight ratios, (b) Y/Y*, (c) Eu/Eu* vs. total REE+Y (µg/g), (d) Ce/Ce* vs. Pr/Pr*, (e) Gd/Gd vs. La/La*, and (f) Sm/Yb$_{SN}$ vs. Pr/Yb$_{SN}$. These reveal that EPT carbonates generally exhibit near-chondritic or elevated Y/Ho ratios, no Ce anomaly, and positive La, Eu, and Y anomalies, along with LREE depletion. Reference data are sourced from Van Kranendonk et al. (2003), Nakamura and Kato (2004), Yamamoto et al. (2004), Allwood et al. (2010), Viehmann et al. (2020) and Marien et al. (2023). (Abbreviations: Cal. – calcite; P – primary; A – altered; Carb. – carbonate; SPF- Strelley Pool Formation; ref.- reference).

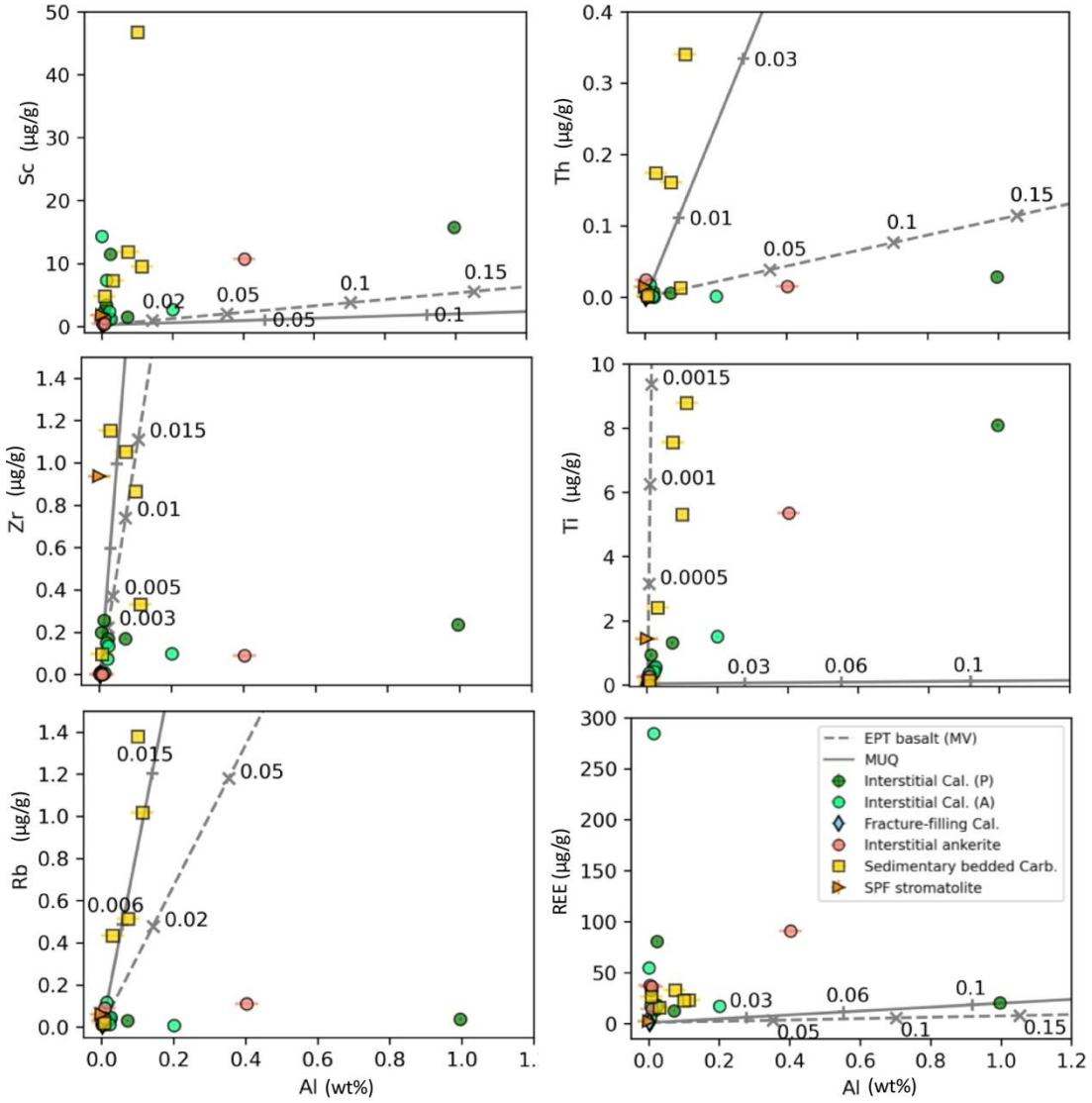

Figure 7: Plots of Al content (wt%) versus the concentrations (µg/g) of (a) Sc, (b) Th, (c) Zr, (d) Ti, (e) Rb, and (f) total REE to evaluate potential detritus contamination. The grey dashed line represents the binary mixing line between seawater endmember D-2-W and the EPT basalt endmember (mean value, MV), while another line shows the binary mixing line between D-2-W and the MUQ endmember, with grey numbers indicating the weight fractions of basalt or MUQ (methods in Appendix A) The plots reveal that only a few sedimentary carbonates may have been slightly affected by detritus, with contamination fractions up to 0.03. (Abbreviations: Cal. – calcite; P – primary; A – altered; Ank. – ankerite; Carb. – carbonate; SPF – Strelley Pool Formation).

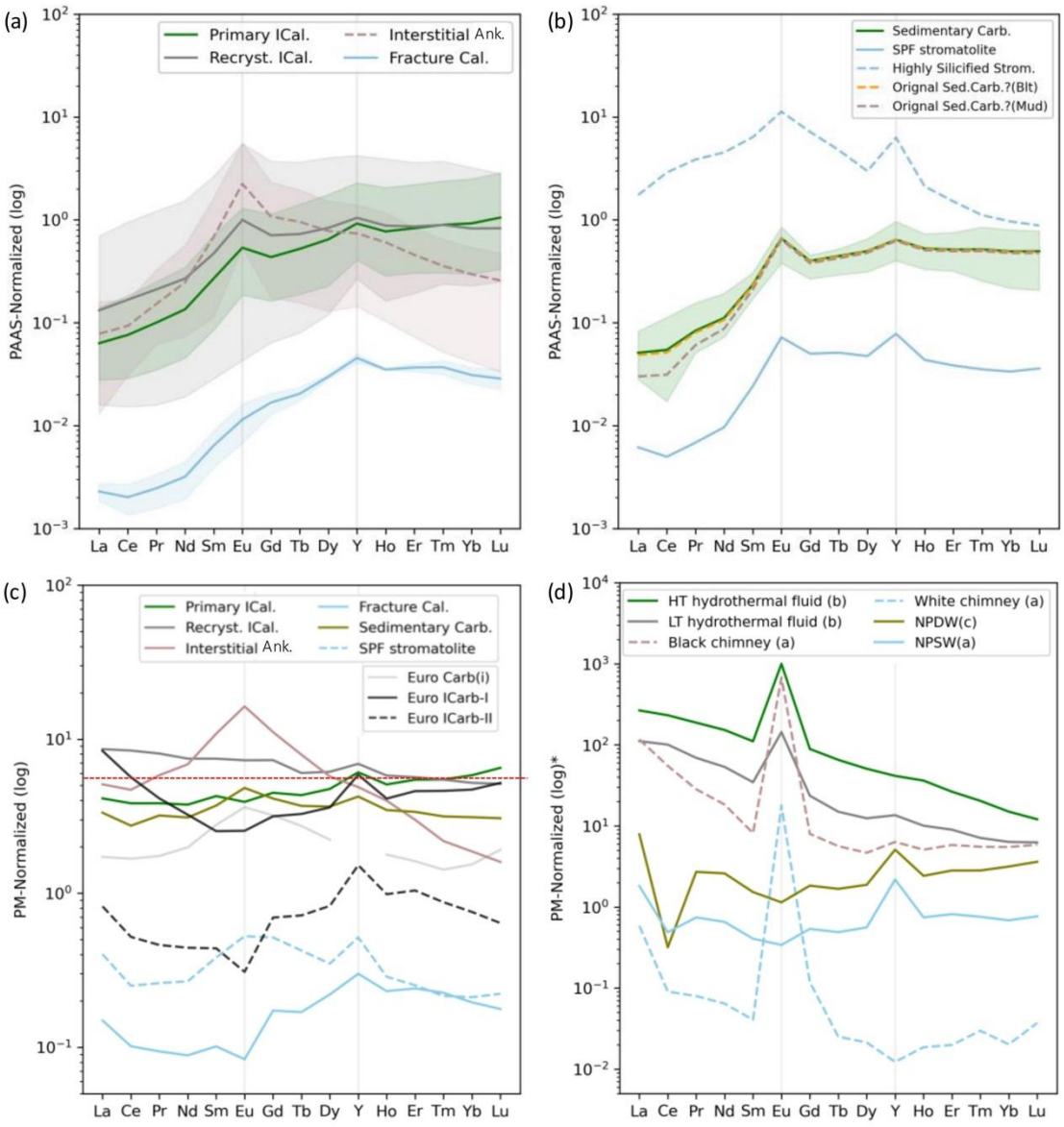

Figure 8: PAAS-normalized REE+Y patterns for EPT carbonates and referenced data showing mean values and ranges across lithologies: (a) primary interstitial calcite (Primary ICal.), altered recrystallized interstitial calcite (Recryst. ICal.), interstitial ankerite (Ank.), and fracture-filling calcite (Fracture Cal.); (b) sedimentary carbonates (Carb.) and Strelley Pool Formation (SPF) stromatolites (dashed blue line: highly silicified counterpart of stromatolite). The orange dashed line represents a 3% reduction from the sedimentary carbonate mean, based on a binary mixing model, indicating maximum basalt detritus contribution (Fig.7). Similarly, the brown dashed line reflects a 3% MUD composition reduction. The mean REE+Y patterns normalized to Primitive Mantle (PM; Palme and O'Neil, 2014) are shown for (c) EPT carbonates and (d) modern references (note: true values ×10⁶ on log y-scale). In (c), mean values of carbonates from the Euro pillow basalt margin ("Euro Carb(i)", Yamamoto et al., 2004) and Type-I and II interstitial carbonates ("Euro ICarb-I" and "Euro ICarb-II", Marien et al., 2023) are plotted. All lines illustrate a distinct shift from seawater to interstitial carbonates. Abbreviations in (d): HT – High Temperature; LT – Low

Temperature; NPDW – North Pacific Deep Water; NPSW – North Pacific Surface Water. Data sources: a. Hongo and Nozaki (2001); b. Bau and Dulski (1999); c. Alibo and Nozaki (1999).

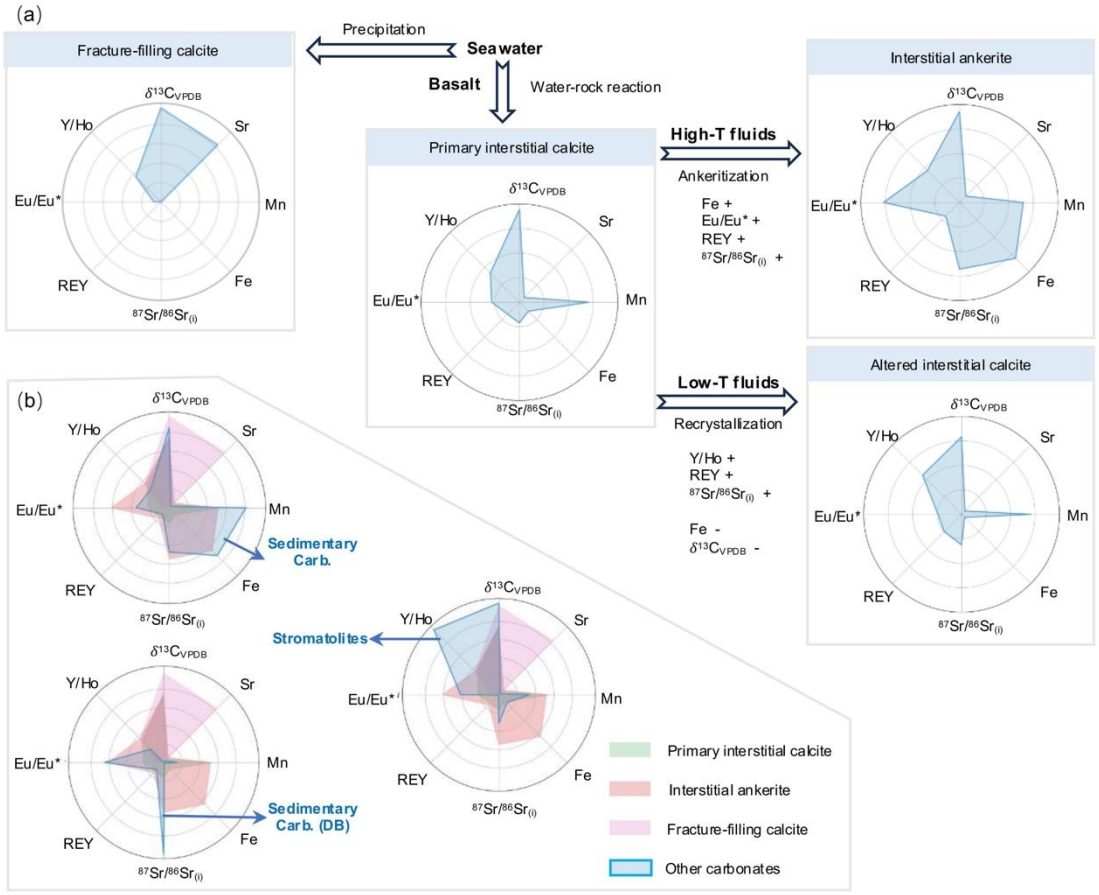

90 **Figure 9: Radar plots integrate diagnostic geochemical features across carbonate facies, including Sr-Mn-Fe concentrations, REE+Y abundance, Y/Ho ratios, Eu anomalies, $^{87}Sr/^{86}Sr$, and $\delta^{13}C$ values. Data ranges (min-max) define axis boundaries, with percentages calculated per facies to highlight compositional deviations. (a) Radar plots for fracture-filling calcite, primary/altered interstitial calcite, and interstitial ankerite reveal fluid-driven geochemical signatures. (b)**
95 **Comparative radar plots of sedimentary carbonates and stromatolites enable rapid diagnosis of depositional environments and diagenetic histories through patterned geochemical deviations and similarities.**

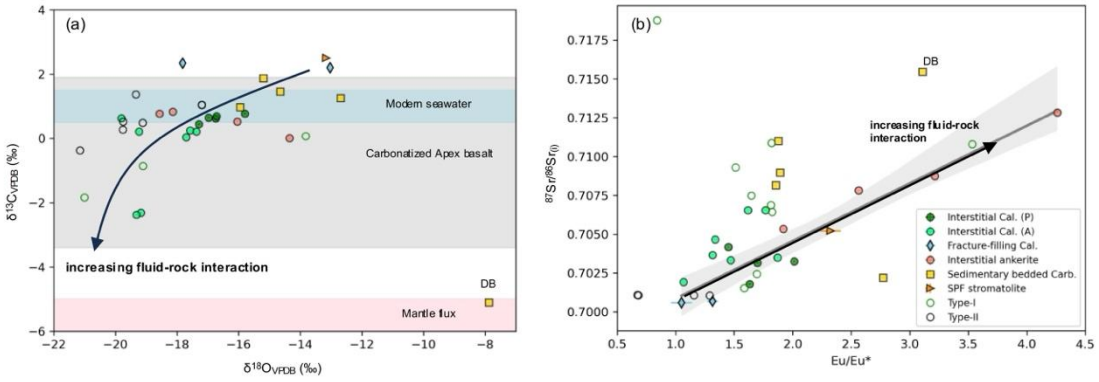

Figure 10: The cross-plots of (a) $\delta^{13}C$ vs $\delta^{18}O$, and (b) the age-corrected $^{87}Sr/^{86}Sr$ ratios vs the PAAS-normalized Eu/ Eu* ratios of the EPT carbonates. The co-variations reflect progressive seawater-basalt reaction (indicated by black arrows). The grey line indicates the regression line based on data of fracture-filling calcite D-2-W, the primary interstitial calcite and interstitial ankerite, and the grey envelope is plotted with the confidence interval of 95%, generated via Seaborn regplot (default). To be noted, some altered interstitial calcite and SPF stromatolite are located in the area. Data sources: (a) Modern seawater data from Kroopnick (1980) and Tan (1988); Carbonatized Apex basalt data from Nakamura and Kato (2004); Mantle flux data from Degens et al. (1984) and Hayes and Waldbauer (2006); (b) Type-I and Type-II Euro interstitial calcite data from Marien et al. (2023). (Abbreviations: P-primary; A-altered; Cal. –calcite; Carb. -carbonate).

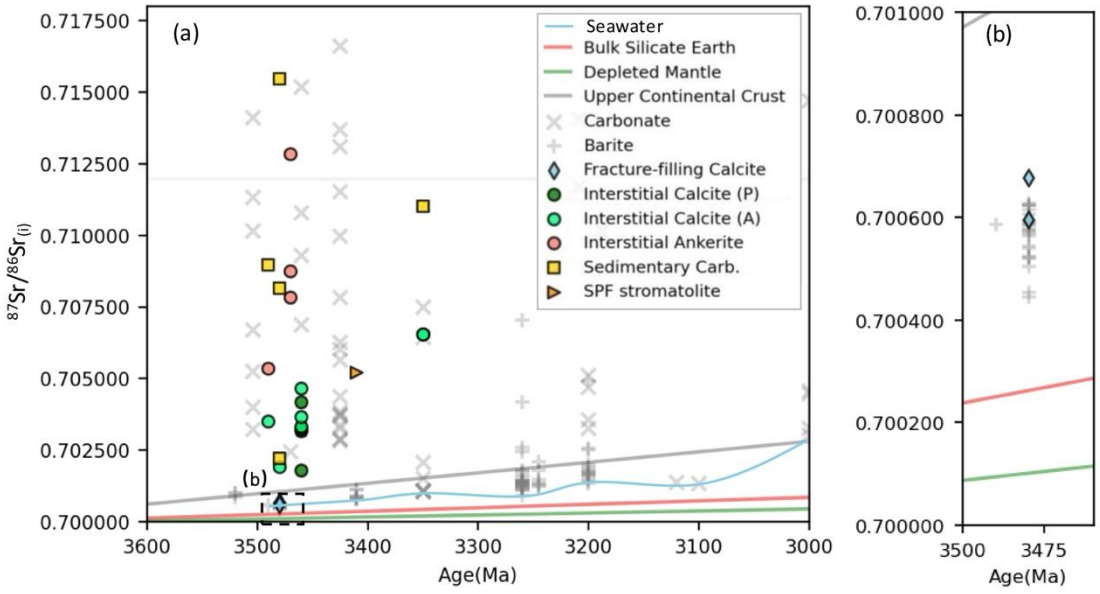

Figure 11: (a) The temporal variations in Sr isotopic compositions of EPT carbonates, alongside reference data from carbonates and barites, plotted against the Sr isotopic evolution curves of Bulk Silicate Earth (BSE), Depleted Mantle (DM), and Upper Continental Crust (UCC). The region marked by the dashed black rectangle is expanded in (b). The blue line represents the inferred seawater Sr isotopic evolution, based on the least radiogenic values observed at any given time. (b) The Sr isotopic compositions of fracture-filling calcites and barites from the Dresser Formation, sharing the same labels as (a). Details of the evolution lines are provided in the Appendix A, with carbonate and barite references sourced from McCulloch (1994), Shields and Veizer (2002), Satkoski et al. (2016), Ravindran et al. (2020), Roerdink et al. (2021), Chen et al. (2022) and Marien et al. (2023). (Abbreviations: P-primary; A-altered; Carb. –carbonate; SPF- Strelley Pool Formation).

Appendix A of

Paleoarchean seawater and seafloor hydrothermal processes: insights from 3.5 to 3.3 Ga carbonate geochemistry

Xiang, Wanli[a, b], Duda, Jan-Peter[b], Pack, Andreas[c], Willbold, Matthias[c], Reitner, Joachim[b, d]

[a] College of Tourism and Geographical Science, Leshan Normal University, Leshan, 614000, China.
[b] Department of Geobiology, University of Göttingen, Göttingen, 37077, Germany.
[c] Department of Geochemistry and Isotope Geology, University of Göttingen, Göttingen, 37077, Germany.
[d] Göttingen Academy of Science and Humanities in Lower Saxony. Göttingen, 37073, Germany

Correspondence to: Reitner, Joachim (jreitne@gwdg.de) and Xiang, Wanli (xiangwanli@lsnu.edu.cn)

1. Binary mixing model

The influence from possible detritus component can be assessed based on the binary mixing model (or two-component mixing model) following the equation:

$$C^E_{mix} = C^E_A \times F + C^E_B \times (1 - F) \qquad \text{(Eq. A.1)}$$

where C^E_A, C^E_B, C^E_{mix} are the concentrations of element E in component A, B and mixture, respectively, while F is a weight fraction. In this work, the binary mixing lines are calculated using the composition of fracture-filling calcite D-2-W as seawater endmember, the mean value of EPT basalts as the basaltic endmember (Van Kranendonk and Pirajno, 2004; Yamamoto et al., 2004; Nakamura and Kato, 2004; Smithies et al., 2005; Jenner et al., 2009; Johnson et al., 2017; Nakamura et al., 2020; Tusch et al., 2021; Tympel et al., 2021; Caruso et al., 2021), and the composition of MUQ (MUd from Queensland, Kamber et al., 2005) as an endmember of the weathered upper continental crust. For the EPT basalts, Al and Ti contents were usually given by the contents of oxides Al_2O_3 and TiO_2, and in this study calculated through Equation A.2, if lack of Al and Ti concentrations:

$$C^E = C^{ox} \times M^E \times m \div M^{ox} \qquad \text{(Eq. A.2)}$$

where C^E and C^{ox} represents the concentrations of element E (here Al or Ti) and oxide E_nO_m, while M^E and M^{ox} represents the atomic weight of element E and molecular weight of its oxide. The histograms of the element concentrations of EPT basalts used for estimating detritus contribution are illustrated in Figure A.2, showing the mean value of Al 7.00 wt% (N=373), Th 0.76 μg/g (N =396), Sc 35.75 μg/g (N=366), Ti 6216.94 μg/g (N=273), Zr 73.95 μg/g (N=308), total REE 47.24 μg/g (N=410) and Rb 23.43 μg/g (N=395).

2. Sr isotopic evolution line

The Sr isotopic evolution lines of the Bulk Silicate Earth (BSE), Depleted Mantle (DM) and Upper Continental Crust (UCC) are calculated based on assumptions below. The BSE Sr isotopic evolution line is calculated from the Basaltic Achondrite Best Initial (BABI) at 4.56 Ga of $^{87}Sr/^{86}Sr = 0.69897$ (Hans et al., 2013) and bulk Earth $^{87}Rb/^{86}Sr = 0.085$ (Taylor and McLennan, 1995). The differentiation occurred at 3.8 Ga (White, 2005; Alexander Bentley, 2006). After that, UCC evolved highly heterogeneously in its $^{87}Sr/^{86}Sr$ due to substantial Rb/Sr fractionation during igneous differentiation processes (White, 2014), thus in this work using the assumed $^{87}Rb/^{86}Sr$ of 0.26 to generate a present-day $^{87}Sr/^{86}Sr$ ratio of 0.714053 (an average present-day isotope composition of $^{87}Sr/^{86}Sr$ ~0.715, Yokoo et al., 2004). Similarly, the present-day DM is also heterogeneous in its Sr isotope composition, owing to melt extraction and re-fertilization by recycled crust (White, 2014). Therefore, a present-day $^{87}Sr/^{86}Sr$ value ~0.702 to 0.703 of the global mid-ocean ridge basalts (MORB) on average (DePaolo and Wasserburg, 1977; Salters and Stracke, 2004) is considered to be representative for the upper depleted mantle, and accordingly an evolution line with $^{87}Rb/^{86}Sr = 0.05$ and the present-day $^{87}Sr/^{86}Sr$ ratio of 0.702603 is used in this work

to indicate the DM evolution. The related decay equation is listed below with a Rb decay constant ($\lambda\ ^{87}$Rb) of 1.394 $\times 10^{-11}$ /a (with t in millions of years, Nebel et al., 2011):

$$(^{87}Sr/^{86}Sr)_{present} = (^{87}Sr/^{86}Sr)_{initial} + (^{87}Rb/^{86}Sr) \times (e^{\lambda t}-1) \quad \text{(Eq. A. 3)}$$

Table A.1: The concentrations of major and trace elements of the references Cal-s, Jls-1 and JDo-1.

Sample ID	Cal-s						JLs-1							Jdo-1						
Reference	Ref. a		this work				Ref. b, c		this work					Ref. b, c		this work				
	(µg/g)		1st		2nd		(µg/g)		1st			2nd		(µg/g)		1st			2nd	
	MV (N=25)	RSD %	MV (N=2, 4*)	RSD%	MV (N=4*)	RSD%	MV (N=7)	RSD %	MV (N=2, 4*)	RSD%	Offset	MV (N=3*)	RSD% Offset	MV (N=7)	RSD %	MV (N=4*)	RSD%	Offset	MV (N=2*)	RSD% Offset
(wt%)																				
Al			0.015	141.4			1383.2		0.008	23.4				637		0.023	141.4			
Ca			39.499	2.6			414000		41.401	0.6				247000		24.923	4.4			
Fe	294		<0.011				106		<0.035					147		<0.028				
K			<0.509				N.A.		<1.636					N.A.		<1.314				
Mg	2358		<0.063				4400		0.220	19.1				227000		11.247	1.5			
Mn	12.076		<0.001				16.4		0.001	8.9				51		0.005	6.5			
Na			<0.414				N.A.		<1.330					N.A.		<1.068				
(µg/g)																				
Sc			0.255	8.1	0.356	6.9			0.226	10.9		0.315	12.5			0.296	12.6		0.400	6.3	
Ti			1.895	11.8	1.320	0.9			0.675	8.8		0.886	6.6			1.491	5.1		2.024	1.5	
V			1.700	2.3	1.271	6.0			2.268	1.3		1.893	5.8			3.526	1.6		2.976	0.7	
Ni	5.000	100.0	N.A.	N.A.	6.860	2.3			N.A			6.572	3.4			N.A			6.160	0.8	
Zn	15.440	18.7	N.A.	N.A.	10.675	2.9			N.A			4.386	4.0			N.A			38.435	0.3	
Rb	0.897	64.5	0.085	4.8	0.055	3.5	0.114	6.0	0.055	6.3	0.483	0.062	4.5	0.545	0.140	50.6	0.032	9.0	0.230	0.035	0.4	0.247
Sr	249.000	4.4	237.880	0.5	259.295	0.9	285.000	1.7	312.369	1.0	1.096	312.823	0.7	1.098	117.000	3.4	116.658	1.1	0.997	117.737	0.4	1.006
Y	1.950	4.1	1.722	0.5	1.846	1.1	0.216	1.5	0.229	0.6	1.060	0.226	1.0	1.048	10.400	4.0	9.886	1.1	0.951	9.897	0.5	0.952
Zr	1.360	86.8	0.205	1.5	0.142	1.8	0.320	11.6	0.040	2.1	0.125	0.059	2.9	0.185	0.560	16.9	0.120	3.7	0.214	0.163	1.6	0.291

Mo	0.185	25.4	0.155	1.6	0.106	2.0			0.039	8.7		0.051	8.8				0.128	4.9		0.143	1.8	
Ba	2.260	211.5	1.207	1.3	1.313	1.5	453.000	4.1	437.858	0.8	0.967	441.142	0.3	0.974	7.000	26.4	5.640	1.6	0.806	5.754	0.2	0.822
La	0.820	8.5	0.768	1.1	0.832	0.6	0.107	1.3	0.118	1.3	1.102	0.115	1.4	1.073	7.700	3.0	7.742	0.6	1.005	7.733	0.5	1.004
Ce	0.347	28.0	0.279	1.6	0.298	1.4	0.187	2.7	0.183	1.2	0.980	0.187	0.3	0.998	2.020	2.5	1.994	0.3	0.987	1.997	0.3	0.989
Pr	0.092	17.4	0.082	1.4	0.088	0.9	0.024	0.9	0.023	0.7	0.954	0.023	2.4	0.994	1.050	3.1	0.980	0.8	0.933	0.980	0.4	0.934
Nd	0.375	19.7	0.341	0.9	0.365	1.1	0.090	0.9	0.092	2.3	1.019	0.096	3.8	1.059	4.090	2.2	4.057	0.7	0.992	4.051	0.2	0.991
Sm	0.058	43.1	0.060	2.2	0.065	1.3	0.019	1.5	0.022	1.7	1.203	0.021	1.7	1.157	0.680	2.1	0.686	1.1	1.010	0.683	0.5	1.005
151Eu	0.018	44.4	0.015	3.1	0.014	1.3	0.005	5.5	0.002	51.6	0.430	0.005	10.7	1.123	0.162	2.4	0.159	1.0	0.982	0.153	0.9	0.945
153Eu	0.018	44.4	0.015	3.7	0.016	3.5	0.005	5.5	0.008	8.7	1.726	0.007	28.9	1.447	0.162	2.4	0.158	1.2	0.977	0.157	0.7	0.971
Gd	0.095	22.1	0.087	1.7	0.095	7.5	0.021	1.4	0.025	5.8	1.161	0.024	6.5	1.124	0.900	2.5	0.842	1.9	0.935	0.832	0.6	0.924
Tb	0.013	23.1	0.013	1.8	0.014	3.3	0.003	0.9	0.003	6.2	1.070	0.003	2.2	1.052	0.120	2.0	0.117	1.0	0.974	0.115	0.6	0.954
Dy	0.092	21.7	0.093	2.4	0.101	0.6	0.020	1.1	0.019	2.3	0.975	0.020	3.2	1.017	0.750	2.5	0.724	0.7	0.965	0.710	0.2	0.947
Ho	0.024	12.5	0.024	2.1	0.026	1.2	0.005	1.6	0.005	3.3	1.006	0.005	2.7	1.005	0.167	2.2	0.160	0.8	0.959	0.160	0.3	0.956
Er	0.072	16.7	0.077	1.6	0.084	2.3	0.014	3.4	0.014	2.6	1.020	0.014	3.8	1.021	0.460	2.0	0.448	0.5	0.975	0.447	1.9	0.972
Tm	0.011	27.3	0.011	3.1	0.011	2.7	0.002	3.2	0.002	9.6	0.903	0.002	5.2	0.997	0.056	2.3	0.054	1.9	0.963	0.054	2.6	0.956
Yb	0.062	22.6	0.065	1.1	0.070	6.0	0.013	1.8	0.012	1.4	0.961	0.013	4.2	1.019	0.305	1.9	0.294	0.7	0.964	0.289	0.0	0.947
Lu	0.010	30.0	0.010	2.9	0.011	9.7	0.002	1.3	0.002	4.4	1.003	0.001	12.2	0.749	0.043	3.8	0.041	1.7	0.953	0.040	1.3	0.930
Hf	0.031	77.4	N.A.	N.A.	0.004	13.0	0.008	57.9	N.A		0.000	0.002	19.8	0.201	<0.03		N.A			0.005	4.3	
Th	0.022	113.6	0.020	3.4	0.018	2.3	0.016	5.2	0.016	3.4	1.007	0.018	2.0	1.107	<0.04		0.039	0.7		0.040	1.0	
U	0.727	7.3	0.734	0.6	0.770	0.4	1.830	5.6	1.569	0.5	0.857	1.540	0.4	0.841	0.880	3.4	0.756	0.7	0.859	0.733	0.8	0.833

Note:

1. The mean value is indicated by MV. RSD% represents the relative standard deviation in percent. Offset is calculated as the ratio of the mean value to the reference value. "N.A." indicates "Not Available".

2. The reference data of Cal-s are taken from Ref. a (Potts et al., 2000), while the reference data of Jls-1 and JDo-1 are obtained from Ref. b (Schier et al., 2018) for major elements, and Ref. c (Dulski, 2001) for trace elements that the measurement number is marked with an asterisk (*) in the mean value (MV) column.

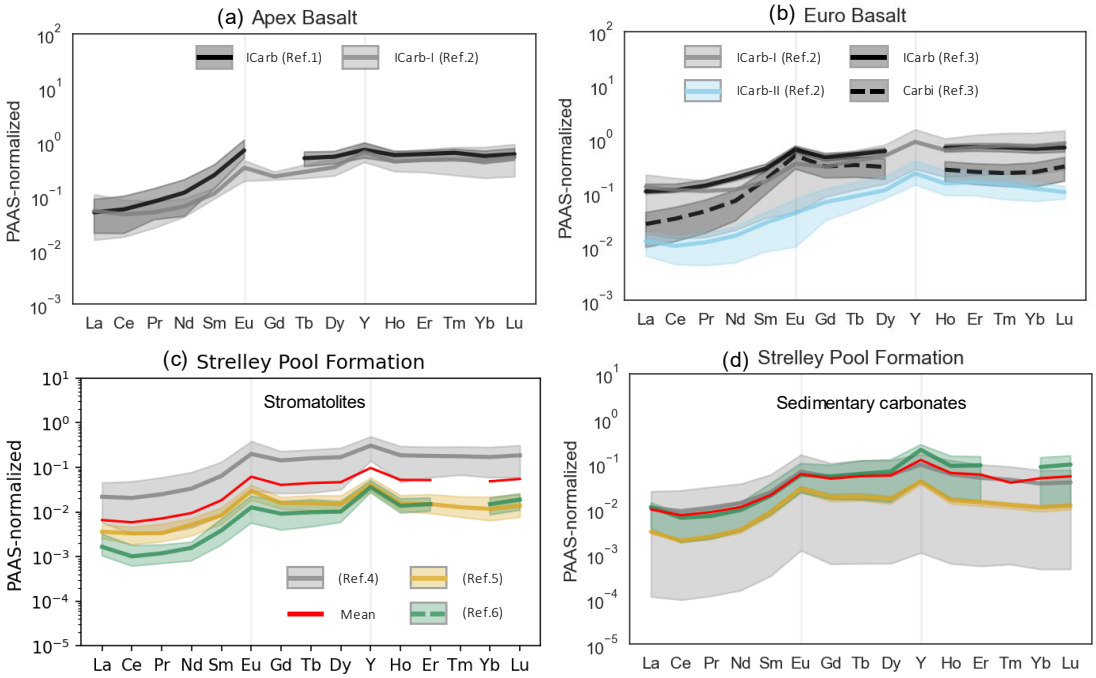

Figure A.1: The PAAS-normalized REE+Y patterns of referenced EPT carbonates, focusing on interstitial carbonates in (a) Apex Basalt and (b) Euro Basalt. "ICarb" denotes interstitial carbonates, with "ICarb-I" and "ICarb-II" representing Type I and II from Ref.2; "Carbi" in (f) refers to carbonate inclusions that are carbonates filling cavities in Euro pillow basalt margins (Ref.3). (c) and (d) display stromatolite and sedimentary carbonate results from the Strelley Pool Formation. Lines of similar color indicate varied data sources from different references; the red "Mean" line represents the average of referenced data. References: Ref.1 - Nakamura & Kato (2004); Ref.2 - Marien et al. (2023); Ref.3 - Yamamoto et al. (2004); Refs.4-6 - Allwood et al. (2010), Viehmann et al. (2020), Van Kranendonk et al. (2003).

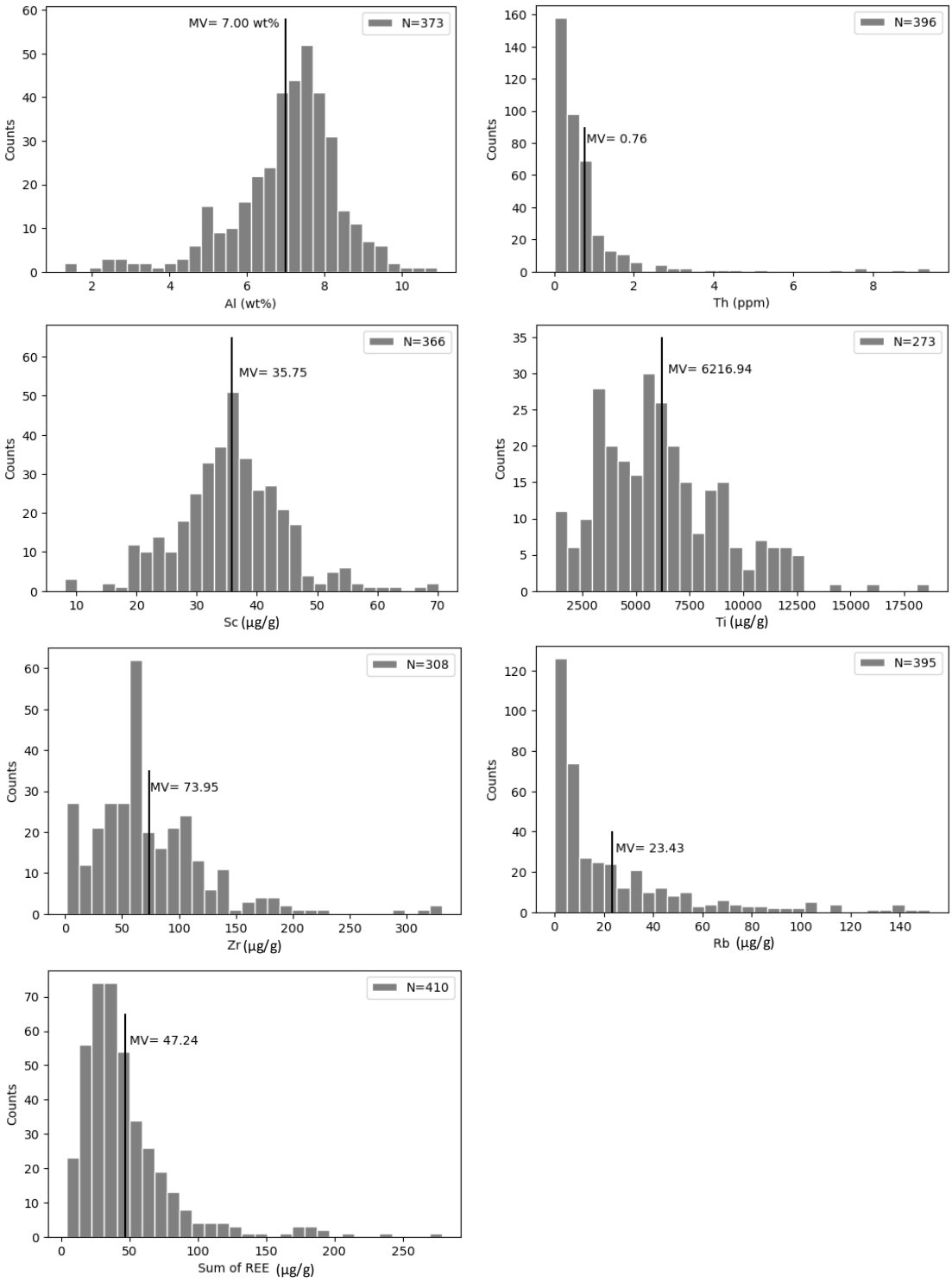

Figure A.2: The histograms about the concentrations of Al (wt%), Th, Sc, Ti, Zr, Rb and the total REE (µg/g) in the EPF basalts. The mean values (MV) are shown in every image. Data come from Van Kranendonk and Pirajno, 2004; Yamamoto et al., 2004; Nakamura and Kato, 2004; Smithies et al., 2005; Jenner et al., 2009; Johnson et al., 2017; Nakamura et al., 2020; Tusch et al., 2021; Tympel et al., 2021; Caruso et al., 2021.

Reference

Alexander Bentley, R., 2006. Strontium Isotopes from the Earth to the Archaeological Skeleton: A Review. Journal of Archaeological Method and Theory, 13(3), 135–187. https://doi.org/10.1007/s10816-006-9009-x.

Allwood, A. C., Kamber, B. S., Walter, M. R., Burch, I. W., & Kanik, I., 2010. Trace elements record depositional history of an Early Archean stromatolitic carbonate platform. Chemical Geology, 270(1–4), 148–163. https://doi.org/10.1016/j.chemgeo.2009.11.013.

Caruso, S., Van Kranendonk, M. J., Baumgartner, R. J., Fiorentini, M. L., & Forster, M. A., 2021. The role of magmatic fluids in the ~3.48 Ga Dresser Caldera, Pilbara Craton: New insights from the geochemical investigation of hydrothermal alteration. Precambrian Research, 362, 106299. https://doi.org/10.1016/j.precamres.2021.106299.

DePaolo, D. J., & Wasserburg, G. J., 1979. Petrogenetic mixing models and Nd-Sr isotopic patterns. Geochimica et Cosmochimica Acta, 43(4), 615–627. https://doi.org/10.1016/0016-7037(79)90169-8.

Dulski, P., 2001. Reference materials for geochemical studies: New analytical data by ICP-MS and critical discussion of reference values, Geostandards Newsletter, 25, 87–125. http://dx.doi.org/10.1111/j.1751-908X.2001.tb00790.x.

Hans, U., Kleine, T., & Bourdon, B., 2013. Rb–Sr chronology of volatile depletion in differentiated protoplanets: BABI, ADOR and ALL revisited. Earth and Planetary Science Letters, 374, 204–214. https://doi.org/10.1016/j.epsl.2013.05.029.

Jenner, F. E., Bennett, V. C., Nutman, A. P., Friend, C. R. L., Norman, M. D., & Yaxley, G., 2009. Evidence for subduction at 3.8 Ga: Geochemistry of arc-like metabasalts from the southern edge of the Isua Supracrustal Belt. Chemical Geology, 261(1), 83–98. https://doi.org/10.1016/j.chemgeo.2008.09.016.

Johnson, T. E., Brown, M., Gardiner, N. J., Kirkland, C. L., & Smithies, R. H., 2017. Earth's first stable continents did not form by subduction. Nature, 543(7644), 239–242. https://doi.org/10.1038/nature21383.

Kamber, B. S., Greig, A., & Collerson, K. D., 2005. A new estimate for the composition of weathered young upper continental crust from alluvial sediments, Queensland, Australia. Geochimica et Cosmochimica Acta, 69(4), 1041–1058. https://doi.org/10.1016/j.gca.2004.08.020.

Marien, C. S., Jäger, O., Tusch, J., Viehmann, S., Surma, J., Van Kranendonk, M. J., & Münker, C., 2023. Interstitial carbonates in pillowed metabasaltic rocks from the Pilbara Craton, Western Australia: A vestige of Archean seawater chemistry and seawater-rock interactions. Precambrian Research, 394, 107109. https://doi.org/10.1016/j.precamres.2023.107109.

Nakamura, H., Kagami, S., Yokoyama, T., Ishikawa, A., Komiya, T., & Iwamori, H., 2020. Compositional heterogeneity of Archean mantle estimated from Sr and Nd isotopic systematics of basaltic rocks from North Pole, Australia, and the Isua supracrustal belt, Greenland. Precambrian Research, 347, 105803. https://doi.org/10.1016/j.precamres.2020.105803.

Nakamura, K., & Kato, Y., 2004. Carbonatization of oceanic crust by the seafloor hydrothermal activity and its significance as a CO_2 sink in the Early Archean. Geochimica et Cosmochimica Acta, 68(22), 4595–4618. https://doi.org/10.1016/j.gca.2004.05.023.

Nebel, O., Scherer, E. E., & Mezger, K., 2011. Evaluation of the 87Rb decay constant by age comparison against the U–Pb system. Earth and Planetary Science Letters, 301(1), 1–8. https://doi.org/10.1016/j.epsl.2010.11.004.

Potts, P. J., Thompson, M., Kane, J. S., Webb, P. C., & Carignan, J., 2000. GEOPT6- An international proficiency test for analytical geochem- istry laboratories - report on round 6 (OU-3: Nanhoron microgranite) and 6A (Cal-s: CRPG limestone), International Association of Geoanalysts, 52.

Salters, V. J. M., & Stracke, A., 2004. Composition of the depleted mantle. Geochemistry, Geophysics, Geosystems, 5(5). https://doi.org/10.1029/2003GC000597.

Schier, K., Bau, M., Muenker, C., Beukes, N., & Viehmann, S., 2018. Trace element and Nd isotope composition of shallow seawater prior to the Great Oxidation Event: Evidence from stromatolitic bioherms in the Paleoproterozoic Rooinekke and Nelani Formations, South Africa, Precambrian Research, 315, 92–102, https://doi.org/10.1016/j.precamres.2018.07.014.

Smithies, R. H., Van Kranendonk, M. J., & Champion, D. C., 2005. It started with a plume – early Archaean basaltic proto-continental crust. Earth and Planetary Science Letters, 238(3), 284–297. https://doi.org/10.1016/j.epsl.2005.07.023.

Taylor, S. R., & McLennan, S. M., 1995. The geochemical evolution of the continental crust. Reviews of Geophysics, 33(2), 241–265. https://doi.org/10.1029/95RG00262.

Tusch, J., Münker, C., Hasenstab, E., Jansen, M., Marien, C. S., Kurzweil, F., Van Kranendonk, M. J., Smithies, H., Maier, W., & Garbe-Schönberg, D., 2021. Convective isolation of Hadean mantle reservoirs through Archean time. Proceedings of the National Academy of Sciences, 118(2), e2012626118. https://doi.org/10.1073/pnas.2012626118.

Tympel, J. F., Hergt, J. M., Maas, R., Woodhead, J. D., Greig, A., Bolhar, R., & Powell, R., 2021. Mantle-like HfNd isotope signatures in ~3.5 Ga greenstones: No evidence for Hadean crust beneath the East Pilbara Craton. Chemical Geology, 576, 120273. https://doi.org/10.1016/j.chemgeo.2021.120273.

Van Kranendonk, M. J., & Pirajno, F., 2004. Geochemistry of metabasalts and hydrothermal alteration zones associated with c. 3.45 Ga chert and barite deposits: Implications for the geological setting of the Warrawoona Group, Pilbara Craton, Australia. Geochemistry: Exploration, Environment, Analysis, 4(3), 253–278. https://doi.org/10.1144/1467-7873/04-205.

Van Kranendonk, M. J., Webb, G. E., & Kamber, B. S., 2003. Geological and trace element evidence for a marine sedimentary environment of deposition and biogenicity of 3.45 Ga stromatolitic carbonates in the Pilbara Craton, and support for a reducing Archaean ocean. Geobiology, 1(2), 91–108. https://doi.org/10.1046/j.1472-4669.2003.00014.x.

Viehmann, S., Reitner, J., Tepe, N., Hohl, S. V., Van Kranendonk, M., Hofmann, T., Koeberl, C., & Meister, P., 2020. Carbonates and cherts as archives of seawater chemistry and habitability on a carbonate platform 3.35 Ga ago: Insights from Sm/Nd dating and trace element analysis from the Strelley Pool Formation, Western Australia. Precambrian Research, 344, 105742. https://doi.org/10.1016/j.precamres.2020.105742.

White, 2005. Chapter 8: Radiogenic Isotope Geochemistry, https://www.imwa.info/geochemistry/Chapters/Chapter08.pdf

White, W. M., 2014. Isotope geochemistry[M]. John Wiley & Sons. ISBN 978-0-470-65670-9 (pbk.)

Yamamoto, K., Itoh, N., Matsumoto, T., Tanaka, T., & Adachi, M., 2004. Geochemistry of Precambrian carbonate intercalated in pillows and its host basalt: Implications for the REE composition of circa 3.4 Ga seawater. Precambrian Research, 135(4), 331–344. https://doi.org/10.1016/j.precamres.2004.09.006.

Yokoo, Y., Nakano, T., Nishikawa, M., & Quan, H., 2004. Mineralogical variation of Sr–Nd isotopic and elemental compositions in loess and desert sand from the central Loess Plateau in China as a provenance tracer of wet and dry deposition in the northwestern Pacific. Chemical Geology, 204(1), 45–62. https://doi.org/10.1016/j.chemgeo.2003.11.004.